Electromechanical resonators for thermodynamics at the nanoscale

Kushagra Aggarwal

St Anne's College
University of Oxford

A thesis submitted for the degree of Doctor of Philosophy

Michaelmas Term 2023

Abstract

Suspended carbon nanotubes provide a unique and versatile platform that combines an electronic degree of freedom with a mechanical resonator. This study delves into the dynamics of this integration, focusing on the effects of electron tunneling through a carbon nanotube on the frequency and amplitude of the mechanical resonator. We observe and analyze the resulting electromechanical coupling, demonstrating how it leads to significant alterations in the resonator's behavior. We have developed a theoretical model that characterizes the electromechanical coupling in detail. This model serves as a foundational tool for interpreting the experimental data and deriving meaningful insights into the behavior of these systems. Our findings underscore the notable back-action of this coupling, which manifests as self-sustained oscillations. These oscillations represent undriven periodic motions that emerge due to the intricate interplay between the electronic and mechanical components of the system. Furthermore, our research identifies pronounced non-linear effects, primarily originating from the Duffing non-linearities inherent in the nanotube when subjected to strong driving forces. These non-linearities add another layer of complexity to the system's dynamics, offering opportunities to study phenomena such as bistability and chaos in nanomechanical systems. The culmination of this work involves leveraging the hybrid nature of this system to investigate the thermodynamic cost of information processing under non-equilibrium conditions. Utilizing the mechanical motion as a piston and the quantum dot as a working fluid, we explore the fundamental principles governing the conversion of information into energy in quantum systems. This exploration provides valuable insights into the thermodynamics of information, particularly in the context of quantum mechanics and nanoscale devices. This thesis also opens new avenues for exploring the limits of thermodynamics in the quantum realm.

Electromechanical resonators for thermodynamics at the nanoscale



Kushagra Aggarwal

St Anne's College

University of Oxford

A thesis submitted for the degree of

Doctor of Philosophy

Michaelmas Term 2023

Acknowledgements

The work presented in this thesis is highly collaborative in nature. I am foremost grateful to Prof. Natalia Ares, my advisor, for offering me the opportunity to work in her group. My gratitude also extends to her generous assistance in various forms and for managing a well-funded laboratory. I extend thanks to Prof. Andrew Briggs, who consistently encouraged to identify what is most important and influential amidst the myriad questions one could pursue. I was fortunate to collaborate with Florian Vigneau in the initial phase of my D.Phil., and none of the experimental measurements would have been possible without his contribution.

I am grateful to the members of the FQXI consortium: Juliette Monsel, Joe Dunlop, Federico Cerisola, Federico Fedele, Lea Bresque, Jorge Tabanera, Alexia Auffeves, Juan Parrondo, and Janet Anders for their theoretical contributions to this thesis. My thanks also extend to Yikai Yang, a postdoctoral researcher who joined our group in my final year, for our enriching discussions. Similarly, I am thankful to Mark Mitchinson for engaging discussions on thermodynamics, which inspired several experimental ideas I hope will be realized soon. I had the privilege of sharing the lab and offices with several D.Phil. students at Oxford, including David Craig, Barnaby van Straaten, Jonas Schuff, Joseph Hickie, Brandon Severin, Marek Rychetsky, Sebastian Orbell, Jonathan Dexter, and Pranav Vaidynathan.

Although predating my time at Oxford and extending beyond the scope of my D.Phil., I am grateful to Georgios Katsaros. I also extend my thanks to my colleagues at IST Austria: Andrea Hofmann, Alessandro Crippa, Marco Valentini, Daniel Jirovec, Luka Drmic, Lada Vukusic.

I am also grateful to Benjamin Huard, although this work also lies outside the scope of my D.Phil., for allowing me to experiment with one of his superconducting qubit setups. This opportunity, along with our discussions about superconducting qubits, was immensely valuable. I thank Yannick Seis for guiding me in the lab in Lyon.

Finally, I owe thanks to my family- my parents and sisters- for their patience and providing the space to explore my own path.

Abstract

Suspended carbon nanotubes provide a unique and versatile platform that combines an electronic degree of freedom with a mechanical resonator. This study delves into the dynamics of this integration, focusing on the effects of electron tunneling through a carbon nanotube on the frequency and amplitude of the mechanical resonator. We observe and analyze the resulting electromechanical coupling, demonstrating how it leads to significant alterations in the resonator's behavior. We have developed a theoretical model that characterizes the electromechanical coupling in detail. This model serves as a foundational tool for interpreting the experimental data and deriving meaningful insights into the behavior of these systems. Our findings underscore the notable back-action of this coupling, which manifests as self-sustained oscillations. These oscillations represent undriven periodic motions that emerge due to the intricate interplay between the electronic and mechanical components of the system. Furthermore, our research identifies pronounced non-linear effects, primarily originating from the Duffing non-linearities inherent in the nanotube when subjected to strong driving forces. These non-linearities add another layer of complexity to the system's dynamics, offering opportunities to study phenomena such as bistability and chaos in nanomechanical systems. The culmination of this work involves leveraging the hybrid nature of this system to investigate the thermodynamic cost of information processing under non-equilibrium conditions. Utilizing the mechanical motion as a piston and the quantum dot as a working fluid, we explore the fundamental principles governing the conversion of information into energy in quantum systems. This exploration provides valuable insights into the thermodynamics of information, particularly in the context of quantum mechanics and nanoscale devices. This thesis also opens new avenues for exploring the limits of thermodynamics in the quantum realm.

List of Publications

13. Kushagra Aggarwal, Juliette Monsel, Joe Dunlop, Federico Cerisola, Florian Vigneau, Pranav Vaidynathan, Jorge Tabanera, Federico Fedele, GAD Briggs, Alexia Auffeves, Juan Parrondo, Janet Anders, Mark Mitchinson, Natalia Ares, *Measuring work and energy exchanges in a nanoscale electromechanical resonator*, in preparation.

12. Joe Dunlop, Federico Cerisola, Kushagra Aggarwal, Juliette Monsel, Natalia Ares, Janet Anders, *Cost of Erasure with Fermion Baths*, in preparation.

11. Kushagra Aggarwal, Sofia Sevitz, Federico Cerisola, Juliette Monsel, Florian Vigneau, Jorge Tabanera, Federico Fedele, GAD Briggs, Juan Parrondo, Gerard Milburn, Janet Anders, Natalia Ares, *A strongly driven nanoelectromechanical resonator coupled to single electron tunneling*, in preparation.

10. Kushagra Aggarwal, Natalia Ares, *Method of operating a parametric amplifier, method of operating a qubit, qubit system*, patent application submitted to the UK Intellectual Property Office (2024).

9. Federico Fedele, Federico Cerisola, Léa Bresque, Florian Vigneau, Juliette Monsel, Jorge Tabanera, Kushagra Aggarwal, Jonathan Dexter, Sofia Sevitz, Joe Dunlop, Alexia Auffèves, Juan Parrondo, Janet Anders, András Pályi, Natalia Ares, *Coupling a single spin to high-frequency motion*, submitted.

8. Marco Valentini, Oliver Sagi, Levon Baghumyan, Thijs de Gijsel, Jason Jung, Stefano Calcaterra, Andrea Ballabio, Juan Aguilera Servin, Kushagra Aggarwal, Marian Janik, Ruben Seoane Souto, Constantin Schrade, Marcel Verheijen, Jeroen Danon, Erik PAM Bakkers, Daniel Chrastina, Giovanni Isella, Georgios Katsaros, *Parity-conserving Cooper-pair transport and ideal superconducting diode in planar germanium*, **Nature Communications 15, 169 (2024)**.

7. Jorge Tabanera-Bravo, Florian Vigneau, Juliette Monsel, Kushagra Aggarwal, Léa Bresque, Federico Fedele, Federico Cerisola, GAD Briggs, Janet Anders, Alexia Auffeves, Juan Parrondo, Natalia Ares, *Stability of long-sustained oscillations induced by electron tunneling*, **arXiv:2211.04074 [cond-mat.mes-hall] (2022)**, Physical Review Research (in press).

6. Florian Vigneau, Juliette Monsel, Jorge Tabanera, Kushagra Aggarwal, Léa Bresque, Federico Fedele, GAD Briggs, Janet Anders, Juan Parrondo, Alexia Auffeves, Natalia Ares, *Ultrastrong coupling between electron tunneling and mechanical motion*, **Physical Review Research 4 (4) 043168 (2022)**.

5. Kushagra Aggarwal, Andrea Hofmann, Daniel Jirovec, Ivan Prieto, Amir Sammak, Marc Botifoll, Sara Marti, Menno Veldhorst, Jordi Arbiol, Giordano Scappucci, Jeroen Danon, Georgios Katsaros, *Enhancement of proximity-induced superconductivity in a planar Ge hole gas*, **Physical Review Research 3 (2) L022005 (2021)**.

4. Tushar Goyal, Kushagra Aggarwal, *Simulator for functional verification and validation of a nanosatellite*, **Proceedings of the** 40^{th} **IEEE Aerospace Conference (2019)**

3. Vatsal Badami, Kushagra Aggarwal, Shubham Sharma, Saurabh Raje, Tushar Goyal, *In-Loop simulation of attitude control of a nanosatellite*, **Proceedings of the** 40^{th} **IEEE Aerospace Conference (2019)**.

2. Rutwik Jain, Shubham Sharma, Kushagra Aggarwal, Tushar Goyal, Abhinav Sundhar, Ujjwal Anand, Nishad Sahu, Joy Parikh, *Modes of operation for a 3U CubeSat with hyperspectral imaging payload*, **Proceedings of the 2018 International Astronautical Congress (2019)**.

1. Saurabh Raje, Abhishek Goel, Shubham Sharma, Kushagra Aggarwal, Dhananjay Mantri, Tanuj Kumar, *Development of On Board Computer for a Nanosatellite*, **Proceedings of the 2017 International Astronautical Congress (2018)**.

Contents

List of Abbreviations **xiii**

1 Introduction **1**

2 Background of Thermodynamic Principles **5**
2.1 Information Thermodynamics 6
2.1.1 Maxwell's Demon 6
2.1.2 Szilard Engine and Landauer's Principle 6
2.2 Stochastic Thermodynamics 7
2.2.1 Fluctuation Theorems 7
2.2.2 Thermodynamic Uncertainty Relationships 10
2.3 Conclusion 11

3 Experimental Methods in Solid-State Devices **13**
3.1 Introduction 13
3.2 Quantum Transport 14
3.2.1 Single Quantum Dot 14
3.2.2 Double Quantum Dots 15
3.3 Fabrication of CNT Devices 16
3.4 SQUID and rf readout of Mechanical Oscillations in CNTs 18

4 Ultrastrong coupling between electron tunneling and mechanical motion **21**
4.1 Introduction 21
4.2 System and electromechanical model 24
4.3 Experimental results 28
4.4 Semiclassical electrostatic model 30
4.5 Simplified electromechanical model in the adiabatic regime 31
4.6 Characterization of the experimental device 33
4.6.1 CNT device 33
4.6.2 Determination of the lever arm and its uncertainty 34
4.6.3 Corrections to the bias voltage 35
4.6.4 Estimation of the CNT's mass 35

4.6.5 Estimation of the size of the quantum dot 38
4.7 Full set of Coulomb peaks 38
4.8 Confirmation of the small amplitude limit 39
4.9 Electric field and single-particle energy levels 41
4.10 Conclusion 42

5 Stability of self-sustained oscillations 43
5.1 Introduction 43
5.2 Experimental setup 44
5.3 Self-oscillations in single dot configuration 45
5.4 Self-oscillations in double dot configuration 51
5.5 Theoretical model 53
5.5.1 Mean-field approximation 54
5.5.2 Mechanical energy 54
5.6 Decay of self-oscillations 55
5.7 Double-dot case 56
5.8 Fitting of the Coulomb peak and tunneling rates 57
5.9 Stability diagram 59
5.10 Additional results 60
5.10.1 Self Oscillations in double quantum dots 60
5.10.2 Statistics for the duration of self-oscillations 62
5.10.3 Temperature dependence 63
5.11 Conclusion 65

6 Non-linear dynamics of an electromechanical resonator 67
6.1 Introduction 67
6.2 Device characterisation 68
6.3 Theoretical model 70
6.4 Steady state response and electronic tunnelling 71
6.5 Results 74
6.6 Conclusion 76

7 Measuring work and energy exchanges in a nanoscale electromechanical resonator 79
7.1 Introduction 80
7.2 Experiment 80
7.2.1 Transduction of displacement 83
7.2.2 Protocol 85
7.3 Electromechanical Model 86
7.3.1 Equation of motion 86

7.3.2 Effective mechanical frequency 89
7.3.3 Numerical simulations of the driven mechanical motion . . . 90
7.4 Thermodynamics of the system 91
7.4.1 Thermodynamic quantities 91
7.4.2 Landauer interpretation 92
7.5 Erasure with two fermion baths 94
7.5.1 Average cyclic work cost of bit reset 95
7.5.2 Work is related to the spread of the occupation distribution 96
7.5.3 Erasure with two Fermion baths 97
7.5.4 Bounding the work cost of erasure 99
7.5.5 Bounds on the mean absolute deviation 101
7.6 Quantifying energy dissipation 104
7.7 Conclusion & Outlook 106

8 Conclusion **109**

List of Abbreviations

CFT . . . . . Crooks Fluctuation Theorem

CNT . . . . . Carbon Nanotube

CVD . . . . . Chemical Vapour Deposition

DC . . . . . Direct Current

ebeam . . . . . Electron Beam Lithography

HEMT . . . . High Electron Mobility Transistor

MEMS . . . . Microelectromechanical System

NEMS . . . . . Nanoelectromechanical System

rf . . . . . Radio Frequency

SEM . . . . . Scanning Electron Microscope

SMA . . . . . SubMinature version A

SQUID . . . . Superconducting Quantum Interference Device

zpm . . . . . Zero Point Motion

1 Introduction

The equations of motion, whether for classical or quantum systems, exhibit time-reversal symmetry. In essence, from the standpoint of physics, transitioning from state A to state B is indistinguishable from moving from state B to state A. Yet, our daily experiences seem to contradict this. For instance, why does ice melt into water at room temperature but not vice versa? The answer lies in the second law of thermodynamics, which introduces the concept of ever-increasing entropy. This law imparts a directionality to processes; for example, the transition from state A (ice) to state B (water) is favored over the reverse because of the positive entropy change.

Historically, thermodynamics has been a remarkably successful theory. However, it traditionally addressed large, macroscopic systems with vast numbers of degrees of freedom. This approach contrasts sharply with recent advancements in various physics domains, where the focus has shifted to isolating single degrees of freedom, rendering average representations ineffective. Such shifts have spurred the evolution of stochastic and quantum thermodynamics, opening new research avenues.

In this thesis, we develop nanoelectromechanical systems (NEMS), study the phenomena arising in these devices and exploit them as a platform for exploring non-equilibrium thermodynamics. These devices are enabled by progress in materials science and fabrication techniques. The mechanical degree of freedom in NEMS have been dispersively, dissipatively and parametrically coupled to electronic degree

of freedom, such as in single electron transistors [1, 2, 3], quantum point contact [4, 5], microwave cavities [6, 7], nitrogen-vacancy centers [8, 9] to name a few. One of the major challenges in NEMS is the reduced quality factor due to increased surface-volume ratio [10]. We use carbon nanotubes as a basis for these devices, owing to its high tensile strength [11]. These nanotubes are lightest form of available nanomechanical resonators with exceptional electronic properties.

In Chapter 2, we provide a brief overview of information thermodynamics and review recent results in stochastic thermodynamics that extend the applicability of thermodynamics to nanoscale devices. Chapter 3 elucidates the experimental techniques used to define single and double quantum dots in carbon nanotubes, the nanofabrication methods for suspended carbon nanotube-based electromechanical resonators, and the operational principles of a radiofrequency amplifier based on a superconducting quantum interference device, crucial for probing the nanotube's mechanical motion.

Chapter 4 explores the interplay between electron tunneling and mechanical motion. We introduce a theoretical model to characterize this relationship, laying the groundwork for subsequent experiments. This chapter also presents experimental data that allows to extract the physical properties of the carbon nanotube.

In Chapter 5, we discover that the rate of electron tunneling through the carbon nanotube can vary based on energy of the quantum dot. Coupled with the stochastic force from electromechanical interactions, this can lead to self-sustained oscillations in the mechanical resonator. These oscillations exhibit intriguing behaviors, such as spontaneous starts, stops, and bistability, due to the underlying mechanism's complexities.

Chapter 6 highlights that carbon nanotubes can experience non-linear restoring forces from various sources, including their geometric structure and electrostatic forces. These Duffing-like forces can significantly influence both mechanical and electronic properties. Given that Duffing's equation serves as a model for investigating limit cycles and chaos, our findings pave the way for exploring these phenomena in nanomechanical systems.

Lastly, in Chapter 7, we harness the insights and control mechanisms from previous chapters to examine the thermodynamics of information under non-equilibrium conditions. This exploration is facilitated by using the mechanical motion as a piston and the quantum dot as a working fluid, especially when the quantum dot is strongly coupled to the Fermi reservoirs ensures that quantum tunneling noise dominates over thermal noise. This thesis not only advances our understanding of the dynamic interactions in nanoelectromechanical systems but also opens new avenues for exploring the limits of thermodynamics in the quantum realm.

2

Background of Thermodynamic Principles

Contents

2.1 Information Thermodynamics 6
2.1.1 Maxwell's Demon 6
2.1.2 Szilard Engine and Landauer's Principle 6
2.2 Stochastic Thermodynamics 7
2.2.1 Fluctuation Theorems 7
2.2.2 Thermodynamic Uncertainty Relationships 10
2.3 Conclusion 11

Traditional thermodynamics is a phenomenological theory, valid in the so-called thermodynamic limit where $N \to \infty$. It considers the relationship between internal energy (U) of the system under consideration, useful work (W) and dissipated heat (Q). The zeroth law introduces thermal equilibrium and notion of temperature (T), while the first law is about conservation of energy. Until now, these laws exhibit time-reversal symmetry, however, the second law of thermodynamics introduces entropy. For physical processes, the entropy is ever increasing which gives directionality to the processes, thereby introducing the arrow of time.

With the current trend in nanoscale and quantum science, where degrees of freedom are being reduced and the dynamics of single degrees become important, we move away from the thermodynamic limit. Indeed, it becomes pertinent to

understand the changes both to the formulation of thermodynamics and expected outcomes. In this chapter, we focus on the laws of thermodynamics considering microscopic degrees of freedom.

2.1 Information Thermodynamics

2.1.1 Maxwell's Demon

Attempts to break the laws of thermodynamics are not something new. One of the earliest and perhaps the most famous example is Maxwell's Demon, proposed by its namesake, James Clark Maxwell in 1867. In this thought experiment, a container with two types of gas molecules: highly energetic, fast-moving molecules and less energetic, slow-moving molecules. With a wall separating the container having a small trapdoor, a demon with information about the molecules can lead to a state where fast-moving and slow-moving molecules are separated in two sections. The demon therefore reduces entropy without performing work- in a clear violation of second law of thermodynamics.

2.1.2 Szilard Engine and Landauer's Principle

In 1929, Leo Szilard proposed a refinement to Maxwell's thought experiment. He proposed just a single molecule of gas in the chamber. Depending on the location of the molecule either in right or left half of the chamber, a weight could be connected to a wall, and the gas molecule isothermally expands such that it lifts the weight getting useful work $k_B T \ln 2$, where k_B is the Boltzmann constant and T is the temperature of the environment.

It was later proposed by Rolf Landauer in 1960 that the demon has to 'know' which part of the box was the particle in. This was the first time a link between entropy and information was introduced. These seminal thought experiments lay the foundations of the information thermodynamics.

2.2 Stochastic Thermodynamics

A central result of classical thermodynamics is that the total entropy in any process can never decrease, leading, inter alia, to fundamental limits on the efficiency of engines and refrigerators. For a long time, the results of thermodynamics were valid only for linear systems capable of reaching equilibrium. Stochastic thermodynamics extends the application of thermodynamic principles to non-equilibrium processes. These results are particularly important for small systems, where the fluctuations of the microstates become important. In this section, I review the thermodynamics of such stochastic systems and seminal results that have been obtained in the past few decades.

2.2.1 Fluctuation Theorems

Fluctuations theorems extend the second law of thermodynamics to non-equilibrium systems and express the probability distribution of heat, work or entropy change, for fluctuating trajectories.

Crooks Fluctuation Theorem

The Crooks fluctuation theorem (CFT) relates the probabilities of observing positive and negative fluctuations of the entropy production in non-equilibrium processes. Consider a system initially in thermal equilibrium and subject to an external driving force. The CFT states that the ratio of the probabilities of positive ($\Delta S > 0$) and negative ($\Delta S < 0$) entropy production values is given by:

$$\frac{P(\Delta S)}{P(-\Delta S)} = \exp\left(\frac{\Delta S_{\text{total}}}{k_{\text{B}}}\right) \tag{2.1}$$

where P(ΔS) and P($-\Delta S$) represent the probabilities of observing positive and negative entropy production, ΔS_{total} is the total change in entropy.

The CFT provides a remarkable symmetry relation between forward and reverse processes, regardless of the detailed nature of the driving protocol. It implies that even in systems driven far from equilibrium, the likelihood of observing positive and negative entropy production events is governed by a universal exponential

factor. This theorem has profound implications for understanding irreversibility in non-equilibrium systems.

Jarzynski Equality

The Jarzynski equality establishes a connection between the exponential average of the work done on a system during a non-equilibrium transformation and the free energy difference between the initial and final equilibrium states. Let W represent the work done on the system in a given trajectory. The Jarzynski equality states:

$$\langle \exp(-\beta W) \rangle = \exp(-\beta \Delta F) \tag{2.2}$$

where ΔF is the free energy difference, and $\langle\rangle$ denotes the average over different trajectories.

The significance of the Jarzynski equality lies in its ability to estimate free energy differences from non-equilibrium measurements. By performing measurements of work for multiple trajectories and taking the exponential average, one can extract valuable information about the equilibrium properties of the system. This breakthrough has enabled the study of small systems and biological processes that are inherently far from equilibrium.

To get a deeper insight, let's consider a system described by a Markovian dynamics, where the state of the system evolves stochastically according to a master equation. The transition rates between states can depend on external parameters, driving the system out of equilibrium. The key idea is to construct a trajectory space by concatenating the states visited by the system along a trajectory. For the CFT, one divides the trajectory space into two regions: the forward (F) and reverse (R) regions. The probabilities of observing a specific trajectory in the forward and reverse processes are denoted by P_{F} and P_{R}, respectively. The entropy production ΔS associated with a trajectory is given by the logarithm of the ratio of these probabilities: $\Delta S = \ln\left(\frac{P_{\mathrm{F}}}{P_{\mathrm{R}}}\right)$. By collecting statistics over a large number of trajectories, one can compute the probabilities P_{F} and P_{R}, and consequently analyze the ratio $\frac{P(\Delta S)}{P(-\Delta S)}$.

The Jarzynski equality involves the evaluation of exponential averages. Suppose we have N trajectories, each starting from an equilibrium state characterized by a probability distribution $P_{\text{eq}}(x)$ and ending in a final equilibrium state characterized by a distribution $P_{\text{eq}'}(x)$. For each trajectory, the work W is computed as the integral of the external force $F(x)$ along the trajectory: $W = \int F dx$. To establish the Jarzynski equality, one considers the exponential average:

$$\langle \exp(-\beta W) \rangle = \Sigma \exp(-\beta W_i) \mathrm{P}(W_i) \tag{2.3}$$

where W_i denotes the work in the i-th trajectory, and $\mathrm{P}(W_i)$ represents the probability of observing that particular work value. By performing work measurements for different trajectories and calculating the corresponding probabilities, one can estimate the exponential average.

The key insight is that the exponential average can be related to the free energy difference between the initial and final equilibrium states. Using statistical mechanics and ensemble averages, one can express the probability distribution ratio $\dfrac{\mathrm{P}(W_i)}{\mathrm{P}_{\text{eq}}(W_i)}$ in terms of the free energy difference ΔF. This leads to the Jarzynski equality:

$$\langle \exp(-\beta W) \rangle = \exp(-\beta \Delta F) \tag{2.4}$$

which provides a direct connection between non-equilibrium work measurements and equilibrium thermodynamics.

The aforementioned theorems have significantly advanced the field of stochastic thermodynamics, enabling researchers to study and understand the behavior of systems driven away from equilibrium. This work has paved the way for applications in various fields, including molecular motors [12], biological processes [13], and the thermodynamics of nanoscale systems [14, 15]. Fluctuation theorems continue to be an active area of research, pushing the boundaries of our knowledge in non-equilibrium statistical physics and offering new avenues for exploring the behavior of complex systems.

2.2.2 Thermodynamic Uncertainty Relationships

The principle of thermodynamics uncertainty relationships revolves around a key idea in non-equilibrium thermodynamics, namely the entropic principle. This principle asserts that all physical systems are subjected to fluctuations, including both natural and engineered systems. In the context of thermodynamics, these fluctuations can involve quantities such as energy, pressure, temperature, and volume. Fluctuations become especially crucial to consider when we look at small-scale systems or those far from equilibrium.

Thermodynamic uncertainty relationships are a class of inequalities that give a quantitative relationship between the fluctuations in a system's entropy production and the changes in other observables, such as the system's state variables. These relationships are essential as they link the microscopic realm of individual particle motion and interactions, where fluctuations play a significant role, to the macroscopic world of thermodynamic laws, which typically describe average behavior.

Historically, the idea behind these relationships was inspired by Heisenberg's Uncertainty Principle in quantum mechanics, which asserts that the more precisely the position of a particle is determined, the less precisely its momentum can be known. Likewise, in thermodynamics, the more accurately a particular thermodynamic quantity is controlled or manipulated, the more the fluctuations in other quantities increase, producing uncertainty.

A fundamental result from these uncertainty relationships is that the precision at which an average thermodynamic current can be maintained is inversely related to the entropy produced in maintaining it. This entropy production is itself linked to the dissipation of energy in the system. In simple terms, one cannot control a system's property to extreme precision without introducing fluctuations and generating some amount of entropy. This is not only a fundamental limit to the control we can exert over thermodynamic systems, but it is also a limit to the efficiency of energy conversion in these systems.

From a practical viewpoint, these thermodynamic uncertainty relationships apply broadly and can be used to understand a wide range of systems. These

include biological systems such as molecular motors and ion channels, engineered nanoscale systems like quantum dots, and even climatic systems. Thermodynamic uncertainty relationships provide a theoretical basis to understand the trade-offs inherent in these systems, such as between the precision of a biological process and the metabolic cost required to maintain it, or the efficiency and precision of an engineered nanoscale machine.

In recent years, thermodynamic uncertainty relationships have emerged as a powerful tool to probe the thermodynamics of small and out-of-equilibrium systems, offering insights into the fundamental limits of natural processes and human-made machines. Understanding these relationships not only deepens our fundamental understanding of thermodynamics but also informs better design of nanoscale machines and better understanding of biological systems.

To summarize, the thermodynamic uncertainty relationships are a fundamental concept in non-equilibrium thermodynamics that link the fluctuations of a system to the precision at which its properties can be controlled. These relationships reveal the inherent trade-offs in thermodynamic systems, which is not only a theoretical interest but also practical implications, providing insights into the limits of natural and engineered systems.

2.3 Conclusion

In this chapter, we discussed the connection between thermodynamics and information. We also reviewed recent theorems and relationships in stochastic thermodynamics, which extend the concepts of thermodynamics to systems operating away from equilibrium conditions. In the next few chapters, we introduce the experimental background of solid-state devices that will be utilised to explore thermodynamics using nanoelectromechanical resonators in Chapter 7.

3

Experimental Methods in Solid-State Devices

Contents

3.1 Introduction 13
3.2 Quantum Transport 14
3.2.1 Single Quantum Dot 14
3.2.2 Double Quantum Dots 15
3.3 Fabrication of CNT Devices 16
3.4 SQUID and rf readout of Mechanical Oscillations in CNTs 18

3.1 Introduction

In the experiments presented in this work, we study the transport through single and double quantum dots, and its coupling to the mechanical motion of CNTs. We focus on the background of semiconducting platforms and relevant experimental techniques in this chapter. We also provide details on the fabrication of CNT-based electromechanical devices. Finally, superconducting quantum interference device (SQUID)-based amplifiers which are used for probing the mechanical motion of the CNTs are presented.

3.2 Quantum Transport

Reducing a dimension of a conductor to the order of the length scale of the electron wavelength introduces quantization of energy states along the confining direction. Reducing dimensions in all three spacial directions results in fully quantized states, similar to energy levels in atoms. Quantum dots are essentially zero-dimensional structures with a discrete energy spectrum. Depending on the material if it is metallic or semiconducting and its dimensionality, such confinement can be achieved in several ways.

Semiconductors provide the ability of confinement, by a careful application of electric fields. CNTs are one-dimensional structures, therefore a confining potential to form a quantum dot is only required in one dimension. In semiconducting CNTs, using electric fields by applying voltages on gate electrodes can be used to achieve this confining potential.

3.2.1 Single Quantum Dot

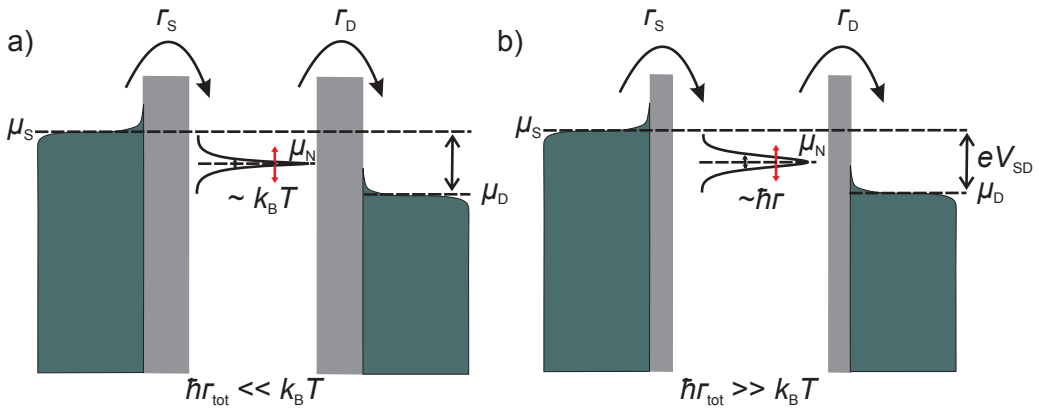


Figure 3.1: A single energy level μ_N is coupled to the source and drain electrodes with electrochemical potentials μ_S and μ_D. The tunneling rates are Γ_S and Γ_D, respectively. The single energy level can be thermally broadened (**a**) or in lifetime broadened (**b**).

A single dot is formed by confining electrons (or holes) in all spatial dimensions, yielding a discrete energy spectrum. Due to the charging effects, electrons can be filled in the single quantum dot one by one. The total energy of the quantum dot with N electrons is denoted $U(N)$. The energy required to add the N^{th}

electron is therefore $\mu_N \equiv U(N) - U(N-1)$, which is the so-called electrochemical potential for the N^{th} electron.

A single dot can be coupled to Fermi reservoirs, such as source and drain electrodes, with their chemical potentials μ_{S} and μ_{D}, respectively. These electrodes are tunnel coupled to the quantum dot with rates Γ_{S} and Γ_{D} for electron transport, with $\Gamma_{\text{tot}} = \Gamma_{\text{S}} + \Gamma_{\text{D}}$. The total energy of the single dot is

$$U(N) = \frac{1}{2}E_{\text{C}}\left(N - N_0 - \frac{C_{\text{S}}V_{\text{S}} + C_{\text{D}}V_{\text{D}} + C_{\text{G}}V_{\text{G}}}{|e|}\right)^2 + \sum_{\text{occupied}} E_n(B) \qquad (3.1)$$

with $U(N)$: Total energy of the dot with N electrons,

E_{C} : Charging energy,

N_0 : Charge in the dot compensating the positive background charge,

$C_{\text{S}}V_{\text{S}}$, $C_{\text{D}}V_{\text{D}}$: Effective induced charges due to source-drain voltages,

$C_{\text{G}}V_{\text{G}}$: Effective gate charge,

$E_n(B)$: Occupied single-particle energy levels.

In addition to the confinement and the charging energy, the coupling of the single dot to the electrodes introduces new energy scales: the thermal energy of the reservoir ($k_{\text{B}}T$), the difference between source-drain chemical potentials ($\mu_{\text{S}} - \mu_{\text{D}} = eV_{\text{SD}}$) and the tunnel couplings. If $k_{\text{B}}T >> \hbar\Gamma_{\text{tot}}$, a quantum dot energy level is said to be thermally broadened, while in case $k_{\text{B}}T << \hbar\Gamma_{\text{tot}}$, the level is said to be lifetime broadened (see Figure 3.1). For a given source-drain bias voltage V_{SD}, an electrical current flows through the dot when $\mu_{\text{D}} < \mu_{\text{N}} < \mu_{\text{S}}$. Therefore, when the energy level is not within this bias window, no current flows through and the quantum dot is in a fixed charge state, this transport regime is effectively called as 'Coulomb blockade'. Experimental measurements of single quantum dots are presented in Chapters 4,5, 6 and 7.

3.2.2 Double Quantum Dots

A double quantum dot is formed by capacitively coupling two single quantum dots either in parallel or series. A schematics of serially coupled double quantum dots in shown in Figure 3.2. In this case, each quantum dot is represented by a single

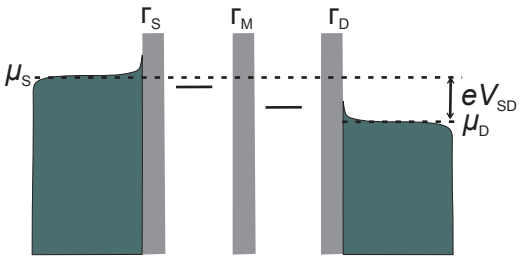


Figure 3.2: The two single electron energy levels are coupled to each other with a tunneling rate Γ_{M}. The double quantum dot can be coupled to source and drain electrodes, which have electrochemical potentials μ_{S} and μ_{D}, with coupling rates Γ_{S} and Γ_{D}.

energy level tunnel coupled to the other quantum dot's energy level. This coupling leads to an additional energy term, a mutual charging energy, which accounts for the energy change in one dot due to filling an electron in the adjacent dot.

The charge configuration of the double dots is often presented in a "honeycomb diagram". In a simplified classical model, the energy of the double quantum dot system can be expressed as:

$$U(N_1, N_2) = \frac{1}{2}N_1^2 E_{C1} + \frac{1}{2}N_2^2 E_{C2} + N_1 N_2 E_{C\mathrm{m}} + f(V_{\mathrm{G1}}, V_{\mathrm{G2}}) \tag{3.2}$$

Here, N_1 and N_2 denote the number of electrons on each dot. E_{C1} and E_{C2} are the respective charging energies, $E_{C\mathrm{m}}$ represents the mutual capacitive interaction, and $f(V_{\mathrm{G1}}, V_{\mathrm{G2}})$ encapsulates the influence of external gate voltages.

For electron transport to occur, certain resonance conditions must be satisfied. At specific points in the stability diagram, known as "triple-points", three charge states become degenerate. This degeneracy facilitates resonant tunneling through the double quantum dot. Experimental measurements of double quantum dots are presented in Chapter 5.

3.3 Fabrication of CNT Devices

The fabrication of suspended CNT devices is done on two separate chips: a silicon substrate with 150 nm SiO_2 and a quartz chip. The silicon substrate hosts the metal electrodes. In the first step, five gate electrodes with 5 nm Ti and 25 nm Au are

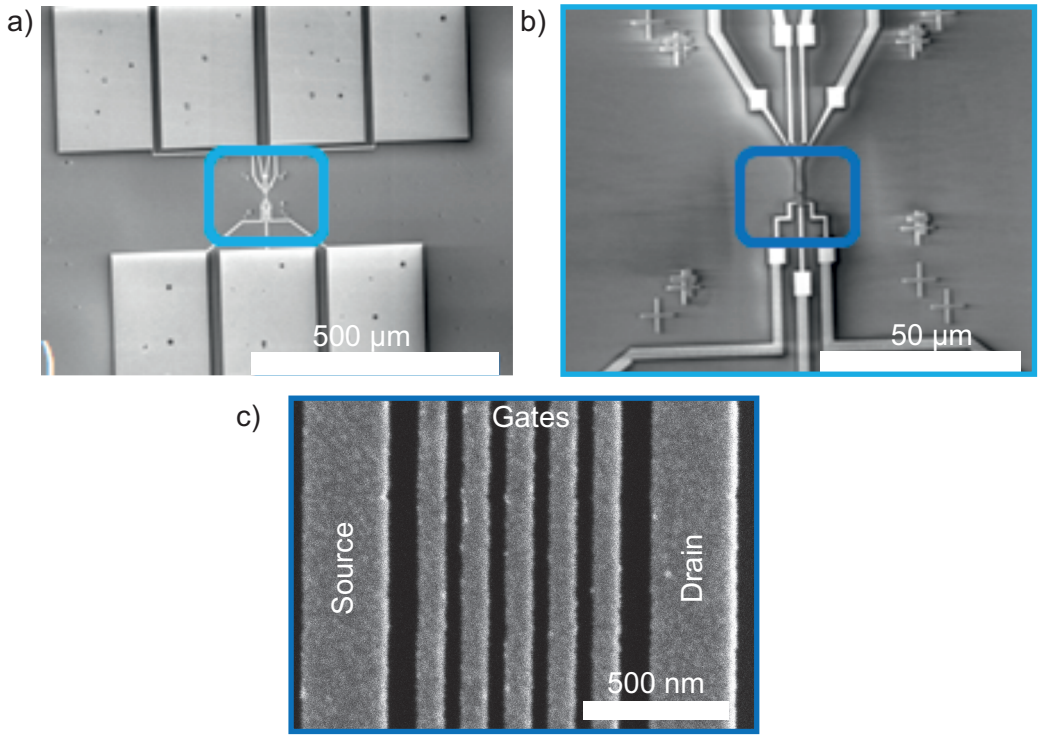


Figure 3.3: a) A scanning electron microscope (SEM) image of a CNT device showing the bonding pads. **b)** A zoomed SEM image showing the device with its connections to the bonding pads. **c)** The source and drain electrodes are at the edges as seen as the broad metal electrodes. In the middle, five electrostatic gates can be seen.

patterned via standard electron-beam (ebeam) lithography and metal deposition. Then, source-drain electrodes with 25 nm Ti and 125 nm Au are patterned using ebeam lithography and metal deposition (see Figure 3.3).

On the quartz chip, pillars of height about 10 µm are defined and a catalyst made out of Al_2O_3 nanoparticles, $Fe(NO_3)_3.9H_2O$ and $MoO_2(acac)_2$ is deposited. The quartz chip with this catalyst deposited over the pillars is transferred to a chemical vapour deposition (CVD) furnace. During the CVD growth, CNTs first grow vertically then fall down, sometimes bridging between a pair of pillars.

In the final step, the CNTs are transferred to a silicon chip with electrodes patterned using a stamping process. In this process, the silicon chip is positioned at the typical substrate location in a mask aligner, while a flipped quartz chip with CNTs is positioned where a mask would normally be placed. The two chips are then aligned using a set of markers and finally brought into close contact

to transfer the CNTs.

Subsequently, the devices are initially tested in a probe station at room temperature by measuring the resistance between the source and drain electrodes. If there is a CNT (or CNTs) between the electrodes, an electrical current can flow through the device. Empirically, in our setup, we found resistances between 100 kΩ and 1 MΩ at room temperature to be promising candidates for further testing.

We screen the devices showing conductance at room temperature through a scanning electron microscope (SEM) to ensure there is just one CNT between the electrodes. It should be noted that CNTs are extremely good at adsorbing impurities, so exposure to an SEM beam should be minimized. Finally, the devices are cooled down in a dilution refrigerator for experiments.

3.4 SQUID and rf readout of Mechanical Oscillations in CNTs

A superconducting quantum interference device (SQUID) is a highly sensitive magnetometer used to measure extremely small changes in magnetic fields. This type of device is made of two or more superconducting loops interrupted by thin layers of insulating material, known as Josephson junctions. When a magnetic field passes through the loop, it alters the phase of the electron wavefunction in a way that depends on the strength of the field. This change in phase shifts the interference pattern created when the two paths around the loop are combined. By observing this shift, it is possible to measure the strength of the magnetic field with remarkable precision. SQUIDs have been extensively used in wide-range of applications, such as magnetic resonance imaging, as well as building blocks of superconducting quantum information devices.

We use a SQUID microstrip rf amplifier (see Figure 3.4a) for probing the mechanical motion of the CNTs (discussed in Chapter 7). In a microstrip SQUID amplifier, the input voltage to be amplified is applied to a thin-film superconductor coil which is in close vicinity of the SQUID which is placed below. As illustrated in the Figure 3.4c, the coil converts the input voltage V_{in} to an electrical current

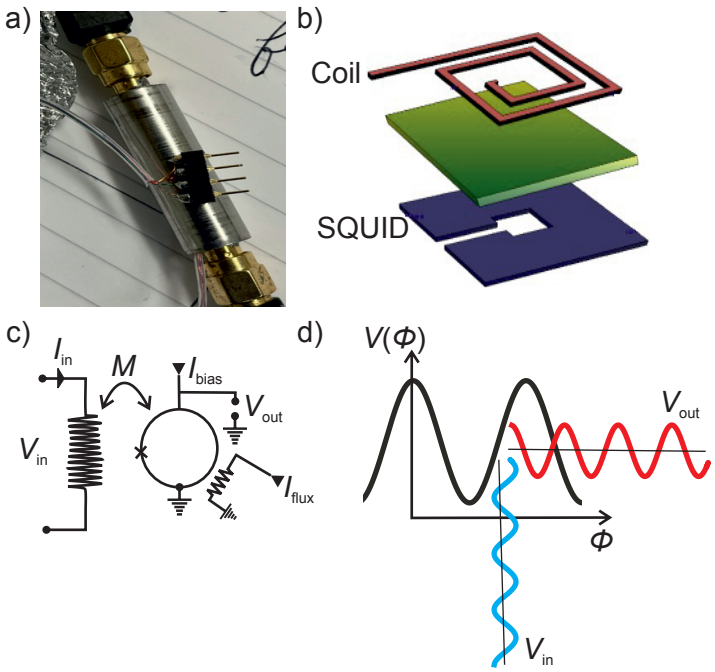


Figure 3.4: a) A SQUID amplifier encased in a magnetic shield with two subminiature version A (SMA) connectors. The four pins are used to DC bias the SQUID amplifier and tune the flux set point. **b)** A coil is inductively coupled to a radiofrequency SQUID. A insulating layer (green) prevents an electrical contact between the coil and the SQUID. **c)** An input voltage V_{in} is applied to the coil which changes the flux threading the SQUID loop. A bias current I_{bias} and flux current I_{flux} is used to set the operating point. The amplified output voltage V_{out} is obtained across the SQUID. **d)** The relationship between the voltage $V(\phi)$ and flux through the SQUID ϕ is sinusoidal. Using I_{bias} and I_{flux}, the operating point is set at the highest slope to obtain the maximum gain.

I_{in}, which induces a change in the total flux threading the SQUID. This in turn modulates the voltage drop across the SQUID, generating the output voltage V_{out}. Maximum amplification is obtained by setting the operating point at the steepest slope as in Figure 3.4d.

4

Ultrastrong coupling between electron tunneling and mechanical motion

Contents

4.1 Introduction 21
4.2 System and electromechanical model 24
4.3 Experimental results 28
4.4 Semiclassical electrostatic model 30
4.5 Simplified electromechanical model in the adiabatic regime 31
4.6 Characterization of the experimental device 33
4.6.1 CNT device 33
4.6.2 Determination of the lever arm and its uncertainty . . . 34
4.6.3 Corrections to the bias voltage 35
4.6.4 Estimation of the CNT's mass 35
4.6.5 Estimation of the size of the quantum dot 38
4.7 Full set of Coulomb peaks 38
4.8 Confirmation of the small amplitude limit 39
4.9 Electric field and single-particle energy levels 41
4.10 Conclusion 42

4.1 Introduction

In this chapter, we study the mechanical motion of the suspended CNT and its coupling to the electron tunneling through it. Ultrastrong coupling between a

quantum system and a nanomechanical resonator is reached when the ratio between the coupling strength g_{m} and the mechanical resonance frequency $\omega_{\mathrm{m}}/2\pi$ is greater than one. In the dispersive regime, such high coupling opens a wide range of possibilities for the development of promising applications in quantum information processing [16], high precision sensors [17, 18, 19], cooling [20], transfer of quantum states to mechanical motion [21, 22] and in the exploration of the foundation of quantum mechanics [23]. The main reason for these promising features lies in the strong back-action of a single photon or electron on the mechanical motion. Unprecedented control over quantum states is then available and macroscopic quantum states can be created allowing for foundational tests of quantum mechanics. Recent proposals suggest that work extraction at the nanoscale is possible in the ultrastrong coupling regime [24, 25], as well as the study of fluctuation theorems [25] and study of systems far from equilibrium [26, 27].

Among the large variety of optomechanical and electromechanical platforms developed [28, 31, 32, 33, 34, 35, 36, 37, 38, 29, 30], the ultrastrong coupling between quantum states and mechanical motion is within reach only for a few, including superconducting circuits ($g_{\mathrm{m}}/\omega_{\mathrm{m}} \simeq 0.35$)[39], NV centers embedded in semiconducting nanowires under a magnetic field gradient ($g_{\mathrm{m}}/\omega_{\mathrm{m}} \simeq 0.1$)[40], and quantum dots in semiconducting nanowires, for which strain is the coupling mechanism ($g_{\mathrm{m}}/\omega_{\mathrm{m}} \simeq 0.85$)[41, 42]. Theoretical proposals indicate that the ultrastrong coupling could be reached in SQUIDs with a mechanical compliant segment [43, 44, 45, 46], single atoms in a cavity [47, 48] or Cooper pair boxes [49, 50, 51].

Quantum dots electrostatically defined in fully-suspended CNT devices (Figure 4.1(a)) offer a high-degree of control over the confinement potential [52]. The mechanical properties of CNTs are also exceptional; comparatively large zero-point motion, quality factors as high as 5 million [53] and mechanical frequencies up to 39 GHz [54].

When the CNT is in motion, its displacement changes the distance between the CNT and the gate electrodes. The quantum dot is thus capacitively coupled to

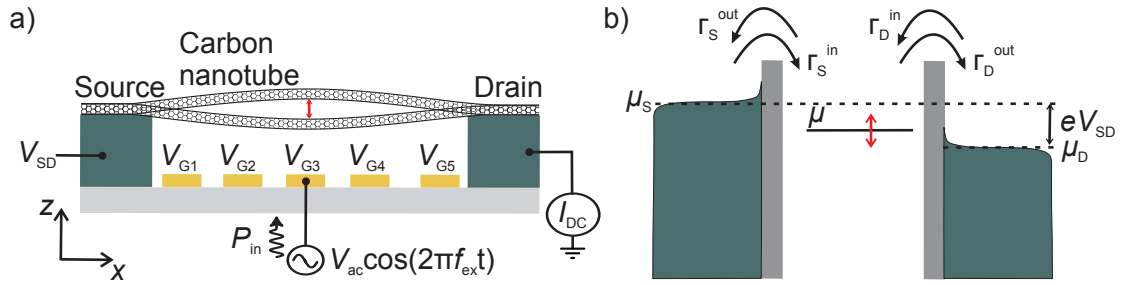


Figure 4.1: (a) Schematic of the device. A CNT is suspended between two metallic reservoirs and over an array of gate electrodes to which we apply gate voltages $V_{\mathrm{G1-G5}}$. A bias voltage V_{SD} drives a current I_{DC} through the nanotube, within which a quantum dot is electrostatically defined. The single-electron tunneling through the quantum dot couples to the nanotube's motion. The coupling strength depends on the distance d between the quantum dot and the gate electrodes. An rf source can be used to excite the mechanical motion of the CNT. (b) Schematic diagram of the electrochemical potential levels of a quantum dot. The source (S) and drain (D) tunnel rates from the reservoirs to the quantum dot are indicated $\Gamma_{\mathrm{S}}^{\mathrm{in}}$, $\Gamma_{\mathrm{S}}^{\mathrm{out}}$, $\Gamma_{\mathrm{D}}^{\mathrm{in}}$ and $\Gamma_{\mathrm{D}}^{\mathrm{out}}$. The electrochemical potentials of source and drain contacts are μ_{S} and μ_{D} respectively, and their energy difference defines a bias window. When the CNT vibrates, the electrochemical potential of the quantum dot μ shifts with respect to a reference electrochemical potential μ_0, which is controlled by the gate electrodes. The red arrow symbolizes the change in μ caused by the nanotube's motion.

the nanotube's motion. The first evidence of this effect was the observation that single-electron tunneling creates periodic modulations of the mechanical resonance frequency [55, 29, 30, 56, 57, 52]. These modulations of the mechanical resonance frequency, also called softening, are a signature of the electromechanical coupling between charge states and mechanical motion [58, 59]. This coupling allowed for the realization of coherent mechanical oscillators driven by single-electron tunneling [60], cooling of the mechanical motion [61], and probing of electronic tunnel rates [62]. Fully-suspended CNT devices in the ultrastrong coupling regime have been proposed for the realization of nanomechanical qubits [63]. A recent study has demonstrated so called deep-strong coupling [64], which is the equivalent of ultrastrong coupling between a CNT quantum dot and a THz resonator [65]. Until now, a careful experimental estimation of the electromechanical coupling strength that CNT devices can offer was still missing.

In this chapter, we show that the electromechanical coupling in fully-suspended CNT devices can reach the ultrastrong coupling regime and that it presents one of the

highest coupling ratios reported so far; $g_m/\omega_m \simeq 2.72$. We obtain this ratio using two independent approaches. We measure the periodic modulations of the mechanical resonance frequency resulting from single-electron tunneling in our experiment and model it using a rate equation model. We also simulate the quantum dot energy levels as the CNT position changes in the plane of motion. Both approaches lead to similar conclusions and converge to the same quantitative value of g_m. The observed coupling ratios can be improved further by adapting the geometry of the device.

4.2 System and electromechanical model

We focus on a CNT device with a suspended segment of approximately 800 nm (see Figure 4.1(a)). The quantum dot is defined in the nanotube through a combination of Schottky barriers at the contacts and the voltages applied to five gate electrodes (labeled V_{G1-G5}) beneath the nanotube. These gate electrodes are also used to actuate the nanotube's motion [66, 67, 60]. A current I_{DC} is driven by a bias voltage V_{SD}. All experiments in this chapter are performed at 40 mK.

To model the interplay between the single-electron transport through the quantum dot and the nanotube's mechanical motion in this device, we use rate equations. First, we describe the electron transport through the device. Applying a bias voltage V_{SD} between the source (left) and drain (right) reservoirs opens up an energy window $eV_{SD} = \mu_S - \mu_D$, where e is the charge of an electron, and μ_S and μ_D are the electrochemical potentials of the left and right reservoirs, respectively. If within this energy window, which we will refer to as bias window, there is an electrochemical potential level μ corresponding to a transition that involves the charge state of the quantum dot, electrons can tunnel from one reservoir onto the quantum dot and off to the other reservoir.

We calculate the current I_{DC} as a function of the quantum dot electrochemical potential μ. The quantum dot is coupled to left and right reservoirs (see Figure 4.1(b)), and this coupling is parameterized by four effective tunnel rates; tunneling from the source/drain reservoir to the quantum dot ($\Gamma^{in}_{S/D}(\mu)$) and tunneling from the quantum dot to the source/drain reservoir ($\Gamma^{out}_{S/D}(\mu)$) [57]. These effective tunnel

rates correspond to the product of the source/drain tunnel barrier rates ($\Gamma_{\mathrm{S/D}}$) and the overlap between the density of states of the quantum dot and source/drain reservoirs, $\rho_{\mathrm{S/D}}(\mu)$, i.e.

$$\Gamma^{\mathrm{in}}_{\mathrm{S/D}}(\mu) = \Gamma_{\mathrm{S/D}}\ \rho_{\mathrm{S/D}}(\mu), \tag{4.1a}$$

$$\Gamma^{\mathrm{out}}_{\mathrm{S/D}}(\mu) = \Gamma_{\mathrm{S/D}}\left(1 - \rho_{\mathrm{S/D}}(\mu)\right). \tag{4.1b}$$

The tunneling through the quantum dot occurs at a rate $\Gamma_{\mathrm{tot}} = \sum_{\mu=S,D}(\Gamma^{\mathrm{in}}_{\mu}+\Gamma^{\mathrm{out}}_{\mu}) = \Gamma_{\mathrm{S}} + \Gamma_{\mathrm{D}}$. As we will show later, $\Gamma_{\mathrm{tot}}/2\pi$ is of the order of 100 GHz, and thus $\hbar\Gamma_{\mathrm{tot}} \gg k_{\mathrm{B}}T$ for sub-Kelvin temperatures, with k_{B} the Boltzmann constant. In this regime, we find [57, 68]

$$\rho_{\mathrm{S/D}}(\mu) = \frac{1}{2} + \frac{1}{\pi}\arctan\left(\frac{2(\mu_{\mathrm{S/D}} - \mu)}{\hbar\Gamma_{\mathrm{tot}}}\right). \tag{4.2}$$

We can thus express the current flowing through the quantum dot as

$$I(\mu) = e\frac{\Gamma^{\mathrm{in}}_{\mathrm{S}}(\mu)\Gamma^{\mathrm{out}}_{\mathrm{D}}(\mu) - \Gamma^{\mathrm{in}}_{\mathrm{D}}(\mu)\Gamma^{\mathrm{out}}_{\mathrm{S}}(\mu)}{\Gamma_{\mathrm{tot}}}. \tag{4.3}$$

We now examine how the mechanical motion affects the electron transport. As the CNT moves, its displacement z in the vertical direction changes the capacitance between the gate electrodes and the quantum dot. This leads to a change in μ proportional to the electromechanical coupling constant g_{m} at the first order in the displacement (see Section 4.5),

$$\mu(z) \simeq \mu_0 + \hbar g_{\mathrm{m}}\frac{z}{z_{\mathrm{ZPM}}}, \tag{4.4}$$

where $z_{\mathrm{ZPM}} = \sqrt{\hbar/2m\omega_{\mathrm{m}}}$ is the zero point motion, with m the nanotube's mass (see Section 4.6.4 for details on the estimation of the CNT's mass), and μ_0 is the electrochemical potential of the quantum dot for a CNT displacement equal to 0, i.e. at $z = 0$. We can control μ_0 with the applied gate voltages.

The change in μ caused by the nanotube's motion produces a change in the average population of the quantum dot. This change can be considered adiabatic if $\Gamma_{\mathrm{tot}} \gg \omega_{\mathrm{m}}$. This means that, on the timescales corresponding to the mechanical motion, the average population instantaneously reaches a steady-state and is

purely defined by the position of the CNT. In this regime, electron-vibron coupling mechanisms such as the Franck-Condon blockade [69, 70, 71] are negligible. In this case, we find that the relative average occupation of the quantum dot with reference to a fixed charge state is

$$p(\mu(z)) = \frac{\Gamma_{\mathrm{S}}^{\mathrm{in}}(\mu(z)) + \Gamma_{\mathrm{D}}^{\mathrm{in}}(\mu(z))}{\Gamma_{\mathrm{tot}}}. \tag{4.5}$$

Note that p is a number between 0 and 1.

The mechanical motion is in turn affected by the electron transport. Variations of p cause the reduction of the mechanical resonance frequency that is considered a signature of strong electromechanical coupling in nanotube mechanical resonators [55, 29, 30, 56, 57, 52]. The effective resonance frequency $\omega_{\mathrm{m}}^{\mathrm{eff}}(\mu_0)/2\pi$, lower than $\omega_{\mathrm{m}}/2\pi$, is observed when μ varies within the bias window $[\mu_{\mathrm{D}}, \mu_{\mathrm{S}}]$. This interplay between single-electron transport and mechanical motion can be explored further by writing the equation of motion that models the CNT displacement (see Section 4.5),

$$\ddot{z} + \omega_{\mathrm{m}}^2 \left[z + 2p(\mu(z)) \frac{g_{\mathrm{m}}}{\omega_{\mathrm{m}}} z_{\mathrm{ZPM}} \right] = 0. \tag{4.6}$$

Since CNT devices exhibit high quality factors, we neglect the mechanical damping over a few mechanical periods.

The combination of Equations (4.5) and (4.6) makes explicit that p can change within a mechanical oscillation, since p depends on μ, and μ depends on z (Equation (4.4)), which is a function of time. Considering that μ has a weak dependence on z, the rest position of the resonator $z_{\mathrm{r}}(p) = -2p(\mu)(g_{\mathrm{m}}/\omega_{\mathrm{m}})z_{\mathrm{ZPM}}$, is obtained for $\ddot{z} = 0$. Figures 4.2(a-c) show the nanotube's displacement z and dot population p as a function of time, as well as the corresponding trajectories in phase space, obtained by solving Equation (4.6) numerically for different values of μ_0. When μ_0 is far above the bias window ($\mu_0 \gg \mu_{\mathrm{S}}$), $p(\mu) = 0$ and the resonator rest position is $z_{\mathrm{r}}(0) = 0$ (dash-dotted green line). Conversely, when μ_0 is far below the bias window ($\mu_0 \ll \mu_{\mathrm{D}}$), the population is $p(\mu) = 1$ and the nanotube's rest position is $z_{\mathrm{r}}(1) = -2(g_{\mathrm{m}}/\omega_{\mathrm{m}})z_{\mathrm{ZPM}}$ (dashed blue line). But when μ_0 is within the bias window, $p(\mu)$ varies between 0 and 1, i.e. $0 \leq p(\mu) \leq 1$, and the nanotube's rest

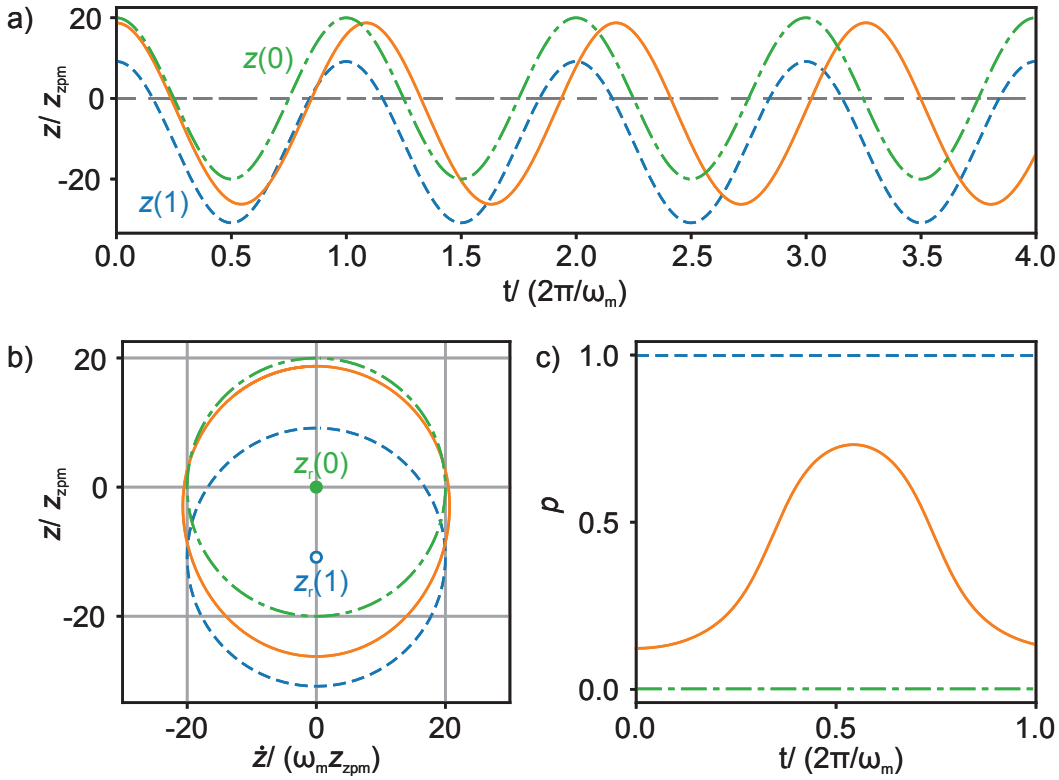


Figure 4.2: Time evolution obtained by numerically integrating the equation of motion (4.6), starting from the initial conditions $z(0) = z_0 + z_r(p(\mu(z_0)))$ and $\dot{z}(0) = 0$, with $z_0/z_{ZPM} = 20$, for three different values of μ_0: well above the bias window ($\mu_0 \gg \mu_S$, dash-dotted green lines), within the bias window ($\mu_0 = 0$, solid orange lines) and well below the bias window ($\mu_0 \ll \mu_D$, dashed blue lines). This choice of $z(0)$ results in identical amplitudes for the cases $\mu_0 \gg \mu_S$ and $\mu_0 \ll \mu_D$. (a) Nanotube's displacement z as a function of time over four mechanical periods. (b) Corresponding phase space trajectories over one mechanical period. The dots indicate the resonator's rest position for $p = 0$ and $p = 1$: $z_r(0)$ (green point) and $z_r(1)$ (blue circle). (c) Population of the quantum dot as a function of time over one mechanical period. These simulations, use the parameters extracted from the experiment; $\omega_m/2\pi = 294.5$ MHz, $\Gamma_S/2\pi = 1.0$ GHz, $\Gamma_D/2\pi = 40$ GHz, and $z_{ZPM} = 0.68$ pm [see Section 4.6]. In the plots, the value of $g_m/2\pi$ was exaggerated by a factor 2 for visual clarity; $g_m/2\pi = 1.6$ GHz while the true value is $g_m/2\pi = 0.8$ GHz.

position satisfies $0 \geq z_r(p) \geq -2(g_m/\omega_m)z_{ZPM}$ (solid orange line). The nanotube's motion follows a trajectory in phase space at constant angular velocity ω_m but the rest position $(0, z_r(p))$ shifts with $p(t)$, making the trajectory elliptical instead of circular (see Figure 4.2(b)). As a result, when p is not constant (solid orange line), the period can exceed $2\pi/\omega_m$, leading to a reduction of the effective mechanical resonance frequency $\omega_m^{eff}(\mu_0)/2\pi$, evident in Figure 4.2(a).

Under the approximation of small displacements, the effective resonance fre-

quency can be estimated from Equation (4.6). Linearizing $p(\mu)$, we obtain

$$p(\mu) = p(\mu_0) + (\mu - \mu_0) \left.\frac{\partial p}{\partial \mu}\right|_{\mu_0}. \tag{4.7}$$

We introduce this expression in Equation (4.6) and use Equation (4.4) to rewrite the equation of motion as follows

$$\ddot{z} + \left[\omega_{\mathrm{m}}^2 + 2g_{\mathrm{m}}^2\hbar\omega_{\mathrm{m}}\left(\frac{\partial p}{\partial \mu}\right)|_{\mu_0}\right] z = -2p(\mu_0)g_{\mathrm{m}}\omega_{\mathrm{m}}z_{\mathrm{ZPM}}. \tag{4.8}$$

Thus the effective resonance frequency is

$$\omega_{\mathrm{m}}^{\mathrm{eff}}(\mu_0) = \sqrt{\omega_{\mathrm{m}}^2 + 2g_{\mathrm{m}}^2\hbar\omega_{\mathrm{m}}\left(\frac{\partial p}{\partial \mu}\right)|_{\mu_0}}. \tag{4.9}$$

Note that $\partial p/\partial \mu$ is negative.

4.3 Experimental results

To verify the validity of this model in our device and estimate the coupling strength g_{m}, we use gate voltages to define a single quantum dot, observed as the Coulomb diamonds in Figure 4.3(a). From this measurement, we estimate the lever arm $\alpha = 0.054^{+0.007}_{-0.005}$ eV/V and its uncertainty (see Section 4.6.2), which relates the variation of μ_0 with the applied gate voltages $\Delta\mu_0 = -\alpha\Delta V_{\mathrm{G1}}$. Measurements in Figure 4.3(a,b) were performed with the CNT at rest (no driven motion), and thus μ is equal to μ_0. From a fit of a Coulomb peak using Equation (4.3) (Figure 4.3(b)), we obtain $\Gamma_{\mathrm{S}}/2\pi = 1.0 \pm 0.1$ GHz and $\Gamma_{\mathrm{D}}/2\pi = 40 \pm 5$ GHz. The uncertainty interval in these tunneling rates is determined by fitting the Coulomb peak with two extreme α values given by the uncertainty in α. We then use Equation (4.5) to estimate p for any value of μ. The resulting $p(\mu)$ is shown in Figure 4.3(c).

We drive the nanotube's motion by a microwave tone at frequency f_{ex} and drive power $P_{\mathrm{in}} = -79$ dBm applied to gate G3 (see Figure 4.1). The mechanical resonance causes sharp steps in $I(f_{\mathrm{ex}})$. Numerically differentiating $I(f_{\mathrm{ex}})$, the resonance is evident as peaks/dips in $\mathrm{d}I/\mathrm{d}f_{\mathrm{ex}}$ (Figure 4.3(d)). The mechanical resonance frequency drops below $\omega_{\mathrm{m}}/2\pi = 294.5$ MHz at values of V_{G1} for which we observed a Coulomb peak (Figure 4.3(b)). We fit this effective resonance frequency,

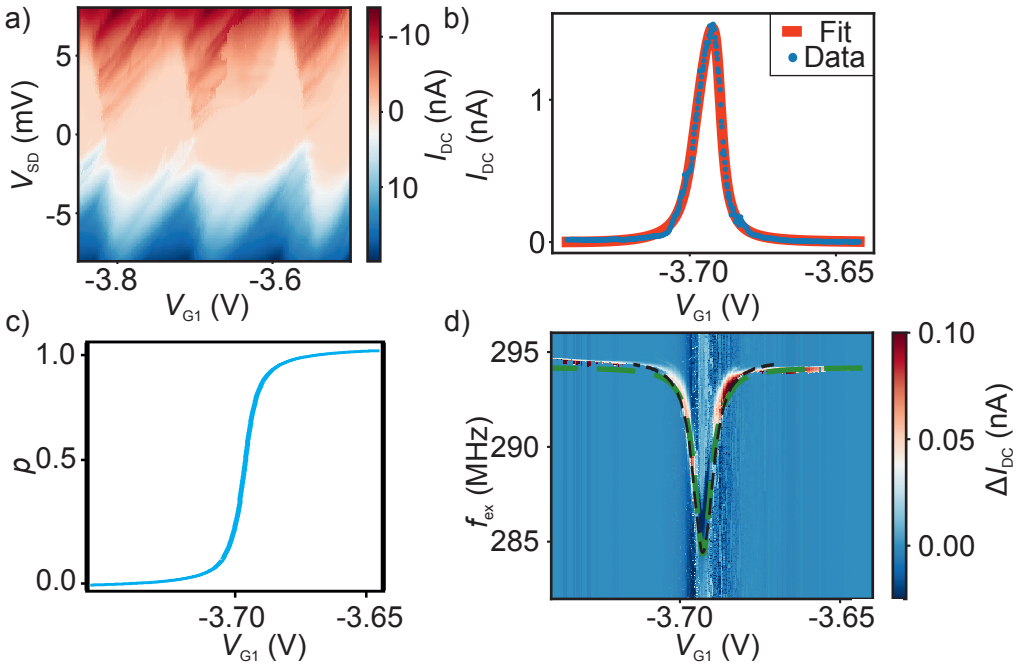


Figure 4.3: (a) I_{DC} as a function of V_{SD} and V_{G1} with $V_{\mathrm{G2}} = 0$ V, $V_{\mathrm{G3}} = -4$ V, $V_{\mathrm{G4}} = 0$ V, $V_{\mathrm{G5}} = -3.95$ V and $R_{\mathrm{s}} = 100$ kΩ. We observe Coulomb diamonds, evidencing single-electron tunneling. (b) I_{DC} as a function of V_{G1} for $V_{\mathrm{SD}} = 0.2$ mV at the Coulomb peak indicated by the blue dotted line in (a). The red line is a fit to Equation (4.3) with $\Gamma_{\mathrm{S}}/2\pi = 1.0$ GHz and $\Gamma_{\mathrm{D}}/2\pi = 40$ GHz. (c) Population p as a function of V_{G1} computed using Equation (4.5) for $z = 0$. (d) Current variation ΔI_{DC} as function of the drive power frequency f_{ex} and V_{G1} at $V_{\mathrm{SD}} = 0.2$ mV. In each column, the average value of the current was subtracted to highlight the mechanical resonance. Near the Coulomb peak, the nanotube's resonance frequency shows a dip. A small shift in V_{G1} explains the gate voltage difference between the center of the Coulomb peak in panels (b) and (d). The green line is a fit with Equation (4.9) and the black line is the effective resonance frequency reproduced by numerical integration of the equation of motion Equation (4.6) with $g_{\mathrm{m}}/2\pi = 0.80$ GHz.

$\omega_{\mathrm{m}}^{\mathrm{eff}}$, using Equation (4.9). Because $p(\mu)$ is estimated from the tunnel rates and μ_0 is calculated from the lever arm α (Figure 4.3(a,b)), the coupling strength g_{m} is the only fitting parameter. The resistance of the measurement circuit was taken into account by correcting the bias voltage accordingly (see Section 4.6.3). We find $g_{\mathrm{m}}/2\pi = 0.80 \pm 0.04$ GHz given the uncertainty over Γ_{S} and Γ_{D}. This result leads to a coupling ratio $g_{\mathrm{m}}/\omega_{\mathrm{m}} \simeq 2.72 \pm 0.14$. This ratio, is, to the best of our knowledge, the highest value reported among all other electromechanical platforms. We have estimated $g_{\mathrm{m}}/2\pi$ for other Coulomb peaks in Section 4.7.

We have further corroborated $\omega_{\mathrm{m}}^{\mathrm{eff}}(\mu_0)$ by numerically integrating Equation (4.6).

This approach does not require $p(\mu)$ to be linearized. We estimate $z_{\mathrm{ZPM}} = 0.68$ pm (see Section 4.6.4), and considering the values of ω_{m}, Γ_{S} and Γ_{D} extracted from the experiment, we compute $z(t)$ for various sets of values of μ_0, g_{m} and $z(0)$, choosing $\dot{z}(0) = 0$. We then derive $\omega_{\mathrm{m}}^{\mathrm{eff}}$ (see Section 4.8) and find that $g_{\mathrm{m}}/2\pi \simeq 0.80$ GHz accurately reproduces the dependence of $\omega_{\mathrm{m}}^{\mathrm{eff}}$ with V_{G1} observed in the experiment (dashed blue line in Figure 4.3(d)). This result is in good agreement with the value of g_{m} obtained from the fit to Equation (4.9). The amplitude of motion, $z(0) \simeq 20 z_{\mathrm{ZPM}} \sim 15$ pm, is consistent with the values estimated in previous experiments [67, 60]. The value of $z(0)$ only significantly affects the width of the dip in the resonance frequency when $z(0)/z_{\mathrm{ZPM}}$ is larger than $\Gamma_{\mathrm{tot}}/g_{\mathrm{m}}$, i.e $z(0)/z_{\mathrm{ZPM}} \gtrsim 50$ (see Section 4.6.4). We thus confirm that the small displacement limit (Equation (4.7)) applies to our experiments.

4.4 Semiclassical electrostatic model

We now compare these results with a semiclassical numerical approximation. We calculate the single-particle energy levels of the dot, $\varepsilon_n(z)$, $n = 0, 1, ...$ In this case, $\varepsilon_n(z)$ is the contribution to the charging energy, μ, which depends on position z for the gate voltage configuration of the experiment. The occupied energy levels will only impose a constant force on the oscillator. In this case, the value of g_{m} can be estimated from Equation (4.4) as

$$g_{\mathrm{m}} = \frac{z_{\mathrm{ZPM}}}{\hbar} \frac{d\varepsilon_n}{dz}. \tag{4.10}$$

We compute the levels $\varepsilon_n(z)$ solving explicitly the electric potential field in the plane of motion, $V(z, x)$, using a finite difference method (see Section 4.9). Then, the dot energy levels can be obtained from $V(z, x)$ using the Bohr-Sommerfeld equation [72],

$$\oint \sqrt{2m_e \left(\varepsilon_n(d) - eV(d, x)\right)} dx = 2\pi\hbar \left(n + \frac{1}{2}\right). \tag{4.11}$$

The integral is calculated along an horizontal line at height d from the gates representing the classical path of the electrons. m_e is the electron mass. Figure 4.4 shows ε for different values of n as a function of the distance d. The values of g_{m}

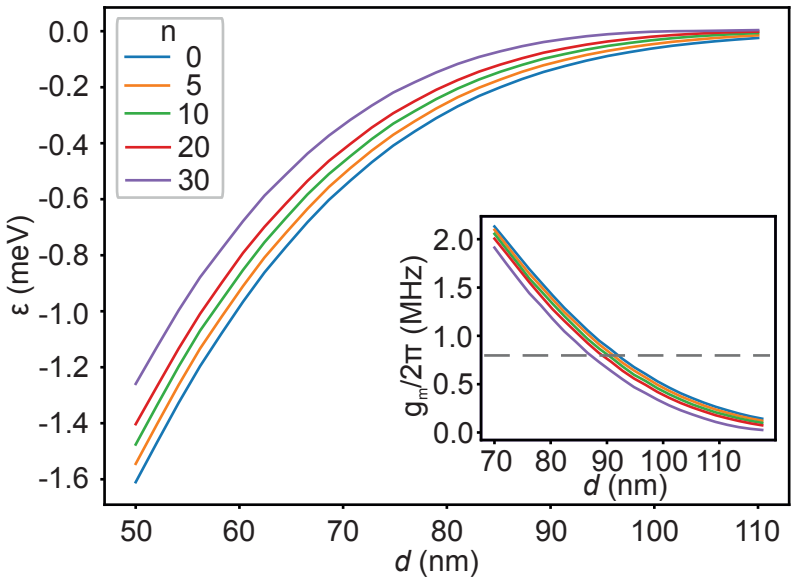


Figure 4.4: Energy levels of the quantum dot with $n = 0, 5, 10, 20, 30$ as a function of d obtained from Equation (4.11). (Inset) Values of g_m obtained from the dependence of the energy levels with d. The dash line represent the value $g_\mathrm{m}/2\pi = 0.80$ GHz obtained from the experiment.

extracted for different values of d are displayed in Figure 4.4(inset). We find a value $g_\mathrm{m}/2\pi \approx 0.80$ GHz for $d = 90$ nm, a distance which is consistent with the geometry of our device (see Section 4.9) considering the deformation of the nanotube. The value of g_m decreases slightly with the quantum level index n and as a function of d, setting the range of possibilities for our platform.

4.5 Simplified electromechanical model in the adiabatic regime

In this section, we give more details about the electromechanical model presented in Section 4.2.

We focus here on a single level of the quantum dot, the one inside or closest to the bias window, assuming that there is at most one level inside it (as represented in Figure 4.1(b)). The quantum dot is capacitively coupled to the gates and the effective capacitance depends on the distance between the quantum dot and the gates. Therefore, the vertical motion of the CNT (CNT) changes the electrochemical

potential μ of the quantum dot level. At the first order in z, we have

$$\mu(z) \simeq \mu_0 + \left.\frac{\partial \mu}{\partial z}\right|_{z=0} z, \tag{4.12}$$

where $z = 0$ corresponds to the rest position of the CNT when the quantum dot level is empty. Like for optomechanical systems [23], we define from the above expression the electromechanical coupling strength

$$g_\mathrm{m} = \frac{1}{\hbar} \left.\frac{\partial \mu}{\partial z}\right|_{z=0} z_\mathrm{ZPM}, \tag{4.13}$$

and obtain the expression of $\mu(z)$ given by Equation (4.4).

So the Hamiltonian describing this simplified model of the electromechanical system is

$$H = \left(\mu_0 + \hbar g_\mathrm{m} \frac{\hat{z}}{z_\mathrm{ZPM}}\right) \hat{n} + \hbar \omega_\mathrm{m} \hat{b}^\dagger \hat{b}, \tag{4.14}$$

where $\hat{b}$ is the annihilation operator of the considered mechanical mode and $\hat{n}$ the occupation of the quantum dot level. The interaction part of the Hamiltonian therefore writes

$$H_\mathrm{int} = \hbar g_\mathrm{m} \frac{\hat{z}}{z_\mathrm{ZPM}} \hat{n}, \tag{4.15}$$

which corresponds to an electromechanical force

$$\hat{F} = -\frac{\partial H_\mathrm{int}}{\partial \hat{z}} = -\frac{\hbar g_\mathrm{m} \hat{n}}{z_\mathrm{ZPM}} \tag{4.16}$$

applied on the resonator.

In addition, electrons tunnel in and out the quantum dot with rates $\Gamma^\mathrm{in}_\mathrm{S/D}(\mu)$ and $\Gamma^\mathrm{out}_\mathrm{S/D}(\mu)$ (see Equations (4.1)) and the mechanical resonators undergoes damping at rate Γ_m. Our device operates in the semi-classical regime (large phonon number in the resonator) where there is no entanglement between the quantum dot and resonator and no coherences inside the quantum dot. Furthermore, the relevant time scales for the tunneling events $1/\Gamma_\mathrm{S/D}$ are orders of magnitude shorter than

the mechanical dynamics (see Table 4.1). Therefore, we make the adiabatic approximation, namely we consider that the population $p = \langle \hat{n} \rangle$ of the quantum dot is always the equilibrium one (Equation (4.5)), and instantaneously follows the variations of $z = \langle \hat{z} \rangle$. The time evolution of the position of the resonator is described by the classical equation of motion

$$\ddot{z} + g_{\mathrm{m}} \dot{z} + \omega_{\mathrm{m}}^2 z = \frac{\langle \hat{F} \rangle}{m}, \tag{4.17}$$

where m is the mass of the resonator. This equation is consistent with the results from Ref. [58]. In the following, we will consider only a few mechanical periods and thus neglect the mechanical damping due to the high quality factor $Q_{\mathrm{m}} = \omega_{\mathrm{m}}/\Gamma_{\mathrm{m}}$ (see Table 4.1). Using Equation (4.16) and the expression of the zero-point motion fluctuation $z_{\mathrm{ZPM}} = \sqrt{\hbar/2m\omega_{\mathrm{m}}}$, we obtain the equation of motion (4.6).

4.6 Characterization of the experimental device

In this section, we describe the suspended CNT device we used in the experiment and explain how we determined its characteristics.

4.6.1 CNT device

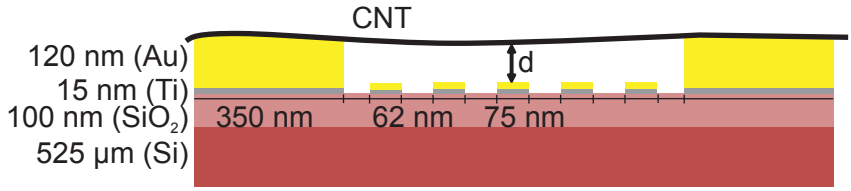


Figure 4.5: Schematic of the device.

The suspended CNT device is similar to the one presented in [66, 67, 60]. We fabricated chips from high resistance Si/SiO_2 substrate by patterning Au/Cr electrodes with electron beam lithography. The CNTs are grown by CVD on a separate quartz substrate using nanoparticles of Al_2O_3, $Fe(NO_3)$ and $MoO_2(acac)2$ as catalyst and mechanically transferred to the chip. Figure 4.5 display a schematic of the device respecting geometric the proportions.

Parameter	Name	Value
Bias voltage	V_{SD}	0.2 mV
Left tunneling rate	$\Gamma_{\mathrm{S}}/2\pi$	1.0 ± 0.1 GHz
Right tunneling rate	$\Gamma_{\mathrm{D}}/2\pi$	40 ± 5 GHz
Lifetime broadening	$\Gamma_{\mathrm{tot}}/2\pi$	41 ± 5 GHz
Bare mechanical frequency	$\omega_{\mathrm{m}}/2\pi$	294.5 MHz
Zero point motion fluctuation	z_{ZPM}	0.68 ± 0.04 pm
Mechanical quality factor	Q_{m}	≤ 2000
Coupling strength	$g_{\mathrm{m}}/2\pi$	0.80 ± 0.04 GHz

Table 4.1: Parameters of the case considered in this chapter.

4.6.2 Determination of the lever arm and its uncertainty

The lever arm $\alpha = \frac{|e|C_{\mathrm{G}}^{l\,\mathrm{dot}}}{C}$ (where $C_{\mathrm{G}}^{l\,\mathrm{dot}}$ is the capacitance between the gate voltage V_{G1} and the dot, and C the sum of the gate, source C_{S} and drain C_{D} capacitances) is critical to in the estimation of the coupling strength. The lever arm can be extracted from the two slopes Slope1 and Slope2 of the Coulomb diamond (Figure 4.6(a)) [73]

$$\mathrm{Slope1} = -\frac{|e|C_{\mathrm{G}}^{l\,\mathrm{dot}}}{C - C_{\mathrm{S}}}, \quad \mathrm{Slope2} = \frac{|e|C_{\mathrm{G}}^{l\,\mathrm{dot}}}{C_{\mathrm{S}}}. \tag{4.18}$$

Combining the two expressions of Equation (4.18), we obtain

$$\alpha = \frac{\mathrm{Slope1} \times \mathrm{Slope2}}{\mathrm{Slope1} - \mathrm{Slope2}} \tag{4.19}$$

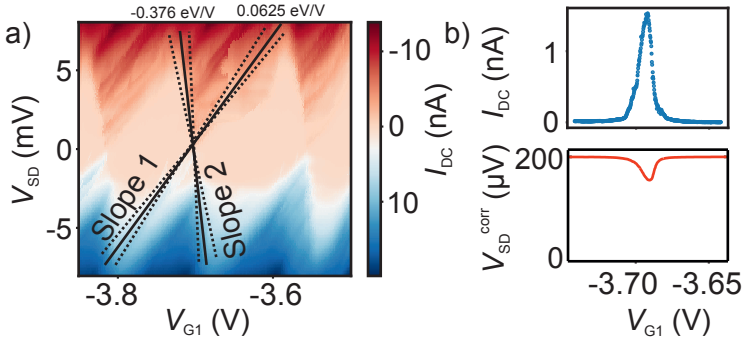


Figure 4.6: (a) Coulomb diamond from Figure 4.3. The two black lines follow the edge of the diamond and correspond to Slope1 $= -0.376^{+0.064}_{-0.174}$ eV/V and Slope2 $= 0.0625^{+0.0065}_{-0.0045}$ eV/V. The dashed lines indicates the error in the determination of the slope. (b) Coulomb peak in Figure 4.3(b) with the measured current I_{DC} (upper plot) and corrected voltage between source and drain contacts (lower plot).

From Figure 4.6(a), we deduce the two slopes Slope1 $= -0.376^{+0.064}_{-0.174}$ eV/V and Slope2 $= 0.0625^{+0.0065}_{-0.0045}$ eV/V, resulting in a lever arm:

$$\alpha = 0.054^{+0.007}_{-0.005}\ \text{eV/V}. \tag{4.20}$$

4.6.3 Corrections to the bias voltage

The internal resistance $R_\text{s} = 100\ \text{k}\Omega$ of the IV converter become a significant fraction of the total resistance of the circuit when the device is tuned in a Coulomb peak. It is therefore necessary to introduce a corrected bias voltage,

$$V_\text{SD}^\text{Corr}(V_\text{G1}) = V_\text{SD} - I(V_\text{G1})R_\text{s}. \tag{4.21}$$

The resulted $V_\text{SD}^\text{Corr}(V_\text{G1})$ is plotted in Figure 4.6(b). The corrected bias voltage was used to fit the Coulomb peak in Figure 4.3(b) and the mechanical resonance frequency in Figure 4.3(d), which impact the estimation of g_m.

4.6.4 Estimation of the CNT's mass

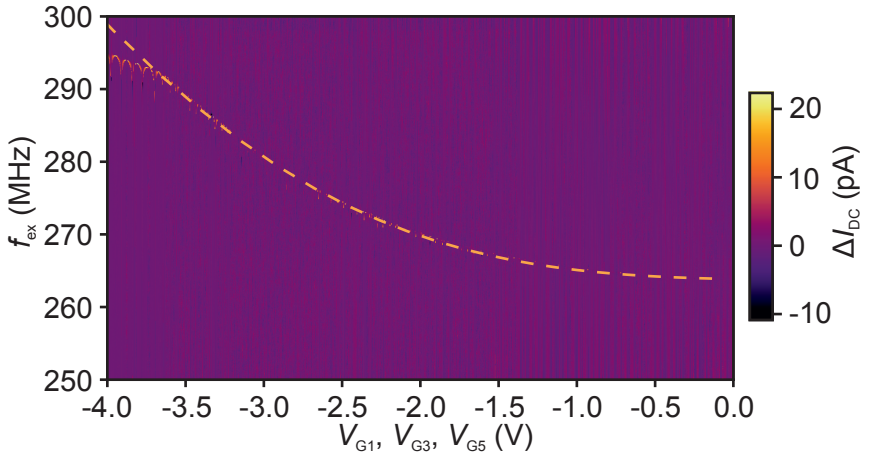


Figure 4.7: Mechanical resonance frequency observed for a large sweep of gate voltages $V_\text{G} = \{V_\text{G1}, V_\text{G3}, V_\text{G5}\}$ while driving the CNT with a microwave tone at frequency $f_\text{e}/2\pi$ in a similar manner as Figure 4.3(d). The mechanical resonance frequency $\omega_\text{m}/2\pi$ is fitted (yellow dashed line) by self-consistently solving for the eigenmodes of Equation (4.22) together with Equation (4.23) and Equation (4.25). The obtained fitting parameters are $L = 936 \pm 10\,\text{pm}$, $r = 3.9 \pm 0.2\,\text{pm}$, $V_0 = 0.82 \pm 0.07\,\text{V}$, $T_r = 0.7 \pm 0.2\,\text{nN}$.

In the following we estimate the mass m of the CNT and its zero point motion z_ZPM from the dependence of the mechanical resonance frequency $\omega_\text{m}/2\pi$ with gate

voltage [74, 75, 76]. We measure the change in current ΔI_{DC} as a function of f_{ex} (Figure 4.7) while sweeping three gate voltages $V_{\mathrm{G}} = \{V_{\mathrm{G1}}, V_{\mathrm{G3}}, V_{\mathrm{G5}}\}$ (V_{G2} and V_{G4} showed leakage currents during the experiment). We observe the increase of ω_{m} when V_{G} become more negative until -3.6 V, where the CNT enters the strong bending regime [77, 75].

Parameter	Estimated value
d	100 nm
L	936 ± 10 nm
r	3.9 ± 0.2 nm
ρ	$1350\,\mathrm{kg/m^3}$
E	1.25 TPa
T_r	0.7 ± 0.2 nN
V_0	0.82 ± 0.07 V
C_{G}	12.9 ± 0.2 aF
$\partial C_{\mathrm{G}}/\partial z$	29.0 ± 0.8 pF/m
m	61 ± 6 ag
z_{ZPM}	0.68 ± 0.04 pm

Table 4.2: Parameters of the estimation of the CNT's mass and zero point motion z_{ZPM}.

To fit the mechanical frequency, we make use of the continuum model developed in [75] and [78] to describe the bending modes of a CNT. The displacement z as a function of time and the position x along the tube axis is modeled by the equation

$$\rho A \frac{\partial^2 z}{\partial t^2} + EI \frac{\partial^4 z}{\partial x^4} - T \frac{\partial^2 z}{\partial x^2} = F(x,t), \tag{4.22}$$

where the first term accounts for the inertia of the CNT, with ρ the mass density of the CNT and A the cross-section area. The second term accounts for the restoring force due to the bending rigidity EI, with E the Young modulus and I the second moment of inertia, while the third term is the restoring force due to the tension T. Finally, the CNT is driven and tuned by the electrostatic force per unit length $F(x,t)$, which is given by [78]

$$F(x,t) = \frac{1}{2} \frac{\partial c_{\mathrm{G}}^l}{\partial z} (V_G(t) - V_0)^2, \tag{4.23}$$

where V_0 is an offset on the dc gate voltage $V_G(t)$ and $c_{\mathrm{G}}^l = C_{\mathrm{G}}/L$, with C_{G} the total capacitance between the CNT and the gates, is the gate capacitance per

unit length. If we approximate the geometry of the problem as that of a cylinder above an infinite plane, then [78]

$$c_{\mathrm{G}}^{l}(x) = \frac{2\pi\epsilon_0}{\operatorname{arccosh}[(d - z(x))/r]} \approx \frac{2\pi\epsilon_0}{\ln(2d/r)} + \frac{2\pi\epsilon_0}{\sqrt{d^2 - r^2}\operatorname{arccosh}^2(d/r)} z(x), \tag{4.24}$$

where d is height of the CNT from the gates (at zero gate voltage), r is the radius of the CNT, and the last approximation is valid for $d \gg r, z$. Finally, the tension T on the CNT has two contributions: one due to the pull of CNT towards the gates which elongates it, and another due to clamping which can introduce a residual tension T_r and bending (so that the length of the clamped CNT is not the same as the length when unclamped) even when the gate voltage is zero. In conclusion, the tension is given by [78]

$$T = T_r + \frac{EA}{2L}\int_0^L \left(\frac{\partial z}{\partial x}\right)^2 \mathrm{d}x. \tag{4.25}$$

One can then get frequency of the eigenmodes of Equation (4.22) by solving Equation (4.22) self-consistently together with Equation (4.23) and Equation (4.25) (see [78] for details on these calculations). We use the obtained fundamental frequency to fit the gate voltage dependence measured in Figure 4.7. To do the fit, we take $\rho = 1350\,\mathrm{kg/m^3}$ and $E = 1.25\,\mathrm{TPa}$, which are standard values for a CNT as it has been widely reported in the literature [78, 79, 80]. We further know from the device fabrication that $d \approx 100\,\mathrm{nm}$. The parameters left to fit are then L, r, T_r, and V_0. The obtained values are shown in Table 4.2 and the resulting fit in Figure 4.7 (dashed yellow line). From L and r we further estimate the mass $m = 61 \pm 6\,\mathrm{ag}$. This gives a zero point motion $z_{\mathrm{ZPM}} = 0.68 \pm 0.04\,\mathrm{pm}$. It is worth pointing out that the uncertainty on z_{ZPM} does not affect the value of coupling coefficient g_{m}, since the expression of the effective mechanical frequency (Equation (4.9)) does not depend on z_{ZPM}. Furthermore, we have found that, in the numerical simulations, small changes in z_{ZPM} only affect the value found for $z(0)$ which is such that $z(0)/z_{\mathrm{ZPM}} \simeq 20$.

4.6.5 Estimation of the size of the quantum dot

Here we estimate the length L_{dot} of the quantum dot confinement in the CNT from the formula of the capacitance between a cylinder and an infinite plane, which for $d \gg z, r$ takes the form

$$C_{\mathrm{G}}^{\mathrm{dot}} \approx \frac{2\pi\varepsilon_0 L_{\mathrm{dot}}}{\ln(2d/r)} \tag{4.26}$$

where ε_0 is the vacuum permittivity. We get the same value of the quantum dot capacitance with respect with V_{G1}, $C_{\mathrm{G}}^{\mathrm{dot}} = 1.46$ aF, estimated from the Coulomb diamond in Figure 4.3(a), for $L_{\mathrm{dot}} = 103$ nm and using the parameters of Table 4.2.

4.7 Full set of Coulomb peaks

We show in Figure 4.8 other Coulomb peaks in the same device. For each Coulomb peak, there is a dip in the mechanical resonance frequency. We applied the method described above to estimate the coupling strength g_{m}. The results of each fit are summarized in Table 4.3. Our data shows no evidence of a dependence of g_{m} with gate voltage. However, the range of gate voltage might be too small to reveal a trend.

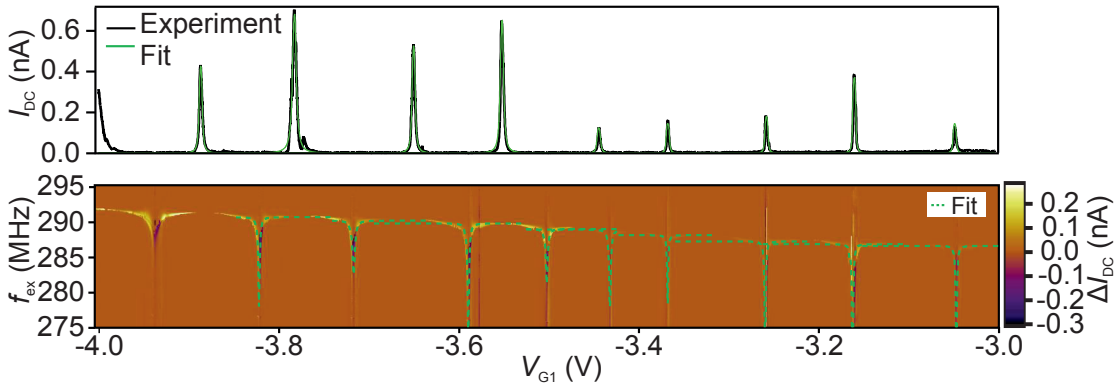


Figure 4.8: Top: Fit (green line) of the Coulomb peaks measured under the same condition as in Figure 4.3(b) for the extended range of V_{G1} (black line). The center of the Coulomb peaks in gate voltage are shifted from the centers of the frequency dips due to gate voltage drifts. Bottom: Corresponding mechanical resonance frequency obtained by measuring the current variation ΔI. The plot was leveled by column for clarity. The mechanical resonance frequency variation are fitted using the linearization presented in Section 4.2, using g_{m} as fitting parameter. The fitting parameters are displayed in Table 4.3.

Param.	$\Gamma_L/2\pi$	$\Gamma_R/2\pi$	V_{G1}^f	V_{G1}^{pk}	$\omega_m/2\pi$	$g_m/2\pi$
Unit	GHz	GHz	V	V	MHz	GHz
Peak 1	0.7	25	-3.821	-3.886	294.6	0.8
Peak 2	1.7	40	-3.716	-3.7815	294.0	0.8
Peak 3	0.9	25	-3.589	-3.6485	293.5	0.9
Peak 4	1.3	30	-3.502	-3.55	292.5	0.7
Peak 5	0.2	30	-3.432	-3.442	292.4	0.8
Peak 6	0.2	20	-3.368	-3.365	291.4	0.8
Peak 7	0.25	20	-3.260	-3.255	290.3	0.8
Peak 8	0.5	15	-3.163	-3.157	289.8	0.8
Peak 9	0.2	20	-3.055	-3.045	289.5	1.0

Table 4.3: Parameters of the fit of the measurements shown in Figure 4.8 from Peak 1 (on the left) to Peak 9 (on the right). The centers of the Coulomb peaks V_{G1}^{pk} are different in gate voltage from the centers of the frequency dips V_{G1}^f due to gate voltage drifts.

4.8 Confirmation of the small amplitude limit

In Section 4.2, we did a first order expansion to obtain the effective mechanical frequency (Equation (4.9)) and used this expression to fit the experimental data (Figure 4.3(d)) and extract the value of g_m. Here, we go one step further and numerically integrate the equation of motion Equation (4.6) to confirm the value found for the coupling strength. This numerical integration requires to choose values for μ_0, g_m and a set of initial conditions ($\dot{z}(0)$, $z(0)$). We choose $\dot{z}(0) = 0$ and therefore $z(0)$ is closely related to the amplitude of the mechanical motion. The other parameters were determined from the experimental data and are given in Table 4.1.

For each set of values $(\mu_0, g_m, z(0))$, we get $\omega_m^{eff}(\mu_0)$ as the slope of the argument of $z(t) + i\dot{z}(t)/\omega_m$. Figure 4.9(a) represents $\omega_m^{eff}(\mu_0)$ as a function of the gate voltage for $g_m/2\pi = 0.80$ GHz and different values of $z(0)$. The quantum dot level μ_0 is related to the gate voltage by the relation $\mu_0 = \alpha\Delta V_{G1})$, k and $\alpha = 0.054$ eV/V. This figure shows that the frequency dip can be characterized by its depth, $\Delta\omega_{max} = \omega_m - \min_{\mu_0}(\omega_m^{eff}(\mu_0))$, and full width at half-minimum, $\Delta\mu_{1/2}$. We extract these two parameters from the experimental data: $\Delta\omega_{max}^{exp}/2\pi = 9.1$ MHz and$\Delta\mu_{1/2}^{exp} = 0.21$ meV. We then plot maps of $\Delta\omega_{max}$ and $\Delta\mu_{1/2}$ (Figure 4.9 (b) and

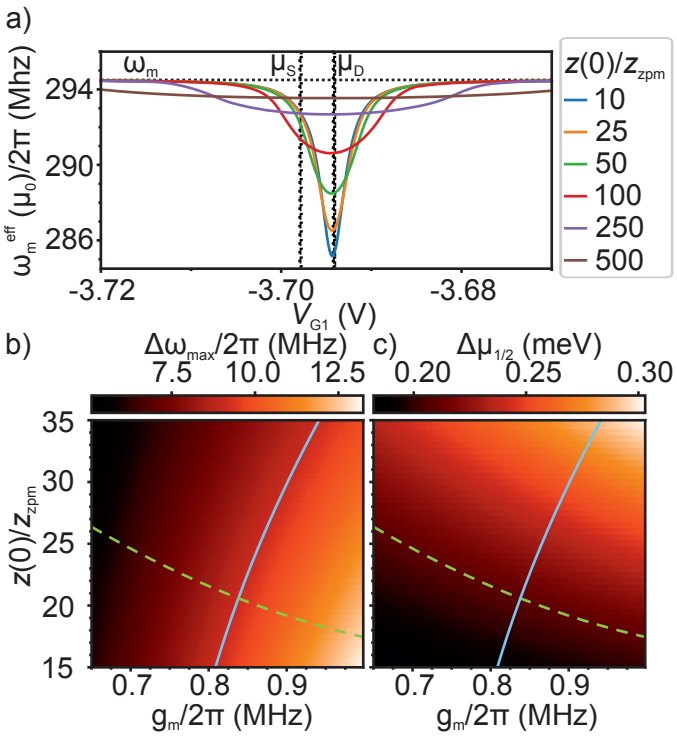


Figure 4.9: Characterization of the frequency dip: (a) mechanical resonance frequency as a function of the gate voltage $V_{G5} = V_0 - \mu_0/\alpha$ for $g_\mathrm{m}/2\pi = 0.80$ GHz and different values of $z(0)$, (b) depth of the dip $\Delta\omega_\mathrm{max} = \omega_\mathrm{m} - \min_{\mu_0}(\omega_\mathrm{m}^\mathrm{eff}(\mu_0))$ and (c) full width at half-minimum $\Delta\mu_{1/2}$ as a function of the initial position $z(0)$ and the coupling strength g_m. The light blue solid line corresponds to $\Delta\omega_\mathrm{max}/2\pi = 9.1$ MHz and the dashed green line to $\Delta\mu = 0.21$ meV, which are the characteristics of the experimental plot in Figure 4.2(c). The other parameters are given in Table 4.1.

(c) respectively) as functions of g_m and $z(0)$. The solid light-blue line corresponds to the experimental depth and the dashed yellow line to the width at half-minimum. The intersection of the two curves gives us the coupling strength: $g_\mathrm{m}/2\pi = 0.84$ GHz for $z(0) = 21 z_\mathrm{ZPM}$. With this method, we obtain a coupling strength in good agreement with the analytical fit ($g_\mathrm{m} = 0.80 \pm 0.04$ GHz), thus validating the first order expansion and, in addition we get an estimate of the amplitude of the mechanical oscillations, ~ 15 pm.

In Figure 4.9(a), we note that the dips are centered on the chemical potential of the right reservoir, μ_D. This is because the two barriers have very different tunnel rates: $\Gamma_L \ll \Gamma_R$. In addition, for small amplitudes of the mechanical oscillations, the widths of the dips are very similar, with $\Delta\mu_{1/2} \simeq \hbar\Gamma_\mathrm{tot}$. In this limit, the

effective frequency is well estimated by Equation (4.9). Conversely, the frequency dip becomes larger when the amplitude of the mechanical oscillations makes $\mu(z)$ vary more than $\hbar\Gamma_{\mathrm{tot}}$, that is for $z(0)/z_{\mathrm{ZPM}} > \Gamma_{\mathrm{tot}}/g_{\mathrm{m}}$. In this case, $\mu(z)$ can enter the bias window even for a μ_0 relatively far outside. Note that $\hbar\Gamma_{\mathrm{tot}}$ is the length of the interval centered in μ_{D} over which $p(\mu)$ varies significantly, see Equations (4.2) and (4.5). For the experimental device, we have $\Gamma_{\mathrm{tot}}/g_{\mathrm{m}} = 50$ so we can reasonably use the small amplitude limit.

4.9 Electric field and single-particle energy levels

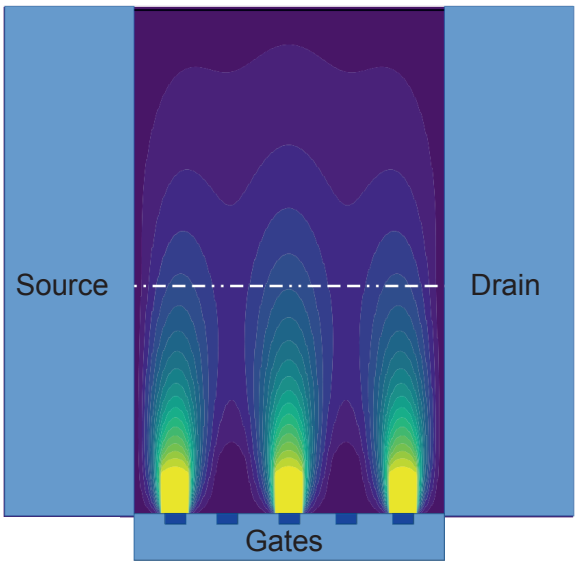


Figure 4.10: Electrical voltage in the vertical plane of the device in an arbitrary gates configuration. The nanotube is represented with an horizontal white line between the source and drain electrodes, at a certain distance from the gates. This line represents the integration path of Equation(11).

We used a finite-differences method in order to calculate the electric potential field in a vertical plane on the device. In this calculation we considered a 1200×1200 grid in order to obtain enough resolution, and imposed the five gates in the bottom on the figure and the two lateral electrodes. The top boundary of the device is considered at sufficient height from the device and kept at constant zero voltage, obtaining a negligible impact on the system [81, 82].

Equation (4.11) requires a path integral along the classical electrons trajectory. In Figure 4.10, we sketch this situation. The electrons path representing the nanotube is considered as a straight horizontal line at a certain distance from the gates, moving from left lead to right.

4.10 Conclusion

To conclude, we have found that fully-suspended CNT devices can reach ultrastrong coupling $g_{\mathrm{m}}/2\pi \approx 0.80 \pm 0.04$ GHz between single-electron transport and mechanical motion, leading to a coupling ratio of $g_{\mathrm{m}}/\omega_{\mathrm{m}} \simeq 2.72 \pm 0.14$, a value that exceeds that obtained with any other electromechanical platform. We have quantified the coupling strength by using rate equations to model the reduction of mechanical resonance frequency observed in our experiments. We separately confirmed the resulting coupling strength with electrostatic simulations based on Bohr-Sommerfeld equations. From these simulations, we extrapolate that this coupling could be enhanced by reducing the distance between the CNTs and the gates and/or the number of charges in the quantum dot. It allows for an ambitious suite of experiments, ranging from nanomechanical qubits to information to work conversion at the nanoscale.

5

Stability of self-sustained oscillations

Contents

5.1 Introduction 43
5.2 Experimental setup 44
5.3 Self-oscillations in single dot configuration 45
5.4 Self-oscillations in double dot configuration 51
5.5 Theoretical model 53
5.5.1 Mean-field approximation 54
5.5.2 Mechanical energy 54
5.6 Decay of self-oscillations 55
5.7 Double-dot case 56
5.8 Fitting of the Coulomb peak and tunneling rates . . . 57
5.9 Stability diagram 59
5.10 Additional results 60
5.10.1 Self Oscillations in double quantum dots 60
5.10.2 Statistics for the duration of self-oscillations 62
5.10.3 Temperature dependence 63
5.11 Conclusion 65

5.1 Introduction

Coupling of quantum devices to mechanical degrees of freedom can be exploited for high-precision measurements [83, 84, 85, 17, 19, 86] and may serve as a platform for quantum and classical information processing [87, 88]. At low temperatures,

CNT devices can be operated as extremely sensitive mechanical oscillators which are strongly coupled to single electron tunneling [89, 91, 30, 79, 92, 93, 94, 95, 17, 90, 28]. The interplay between single electron tunneling and mechanical motion, in the absence of a mechanical drive, can give rise to self-sustained oscillations. Such self-oscillations were observed to be either present or absent depending on the electron transport regime, both in theory [96, 97, 98] and experiments [29, 99, 100, 101, 60, 63, 102].

In this chapter, we explore self-oscillations that can appear or vanish spontaneously. These bistable states of motion of an undriven oscillator, until now unexplored, are of particular interest for applications of these devices in quantum and stochastic thermodynamics [103, 27, 104, 105], in collective dynamics and synchronization [106], and in emulating neural behavior [107, 108, 109]. We measure bistable self-oscillations both for single and double quantum dot configurations and present a theoretical analysis that provides a complete characterization of the stability of self-oscillations at different bias voltages. Once started, undriven oscillations can be self-sustained and may decay over time scales of the order of 10^8 mechanical periods. In this way, our system explores timescales of electronic and mechanical origin that are separated by several orders of magnitude.

5.2 Experimental setup

The same device from Chapter 4 is used for this experiment (see Figure 5.1(a)). Applying a bias voltage V_{SD} between the source and drain electrodes, we measure a current I_{DC} through the CNT. The gate electrodes, to which we apply voltages $V_{\mathrm{G1\text{-}5}}$, are located beneath the CNT. These gate voltages define an electrostatic potential for the confined charges, and depending on the combination of gate voltage values, we can define single or double quantum dots within the CNT (Figs. 5.1(a,b)) [110, 73].

The mechanical motion of the CNT can be excited by applying an rf signal to one of the gate electrodes. Sharp changes in the current through the CNT indicate its mechanical motion [89, 111, 54], and we identify the natural mechanical resonance frequency $\omega_{\mathrm{m}}/2\pi = 270$ MHz with an approximate quality factor Q of 2000.

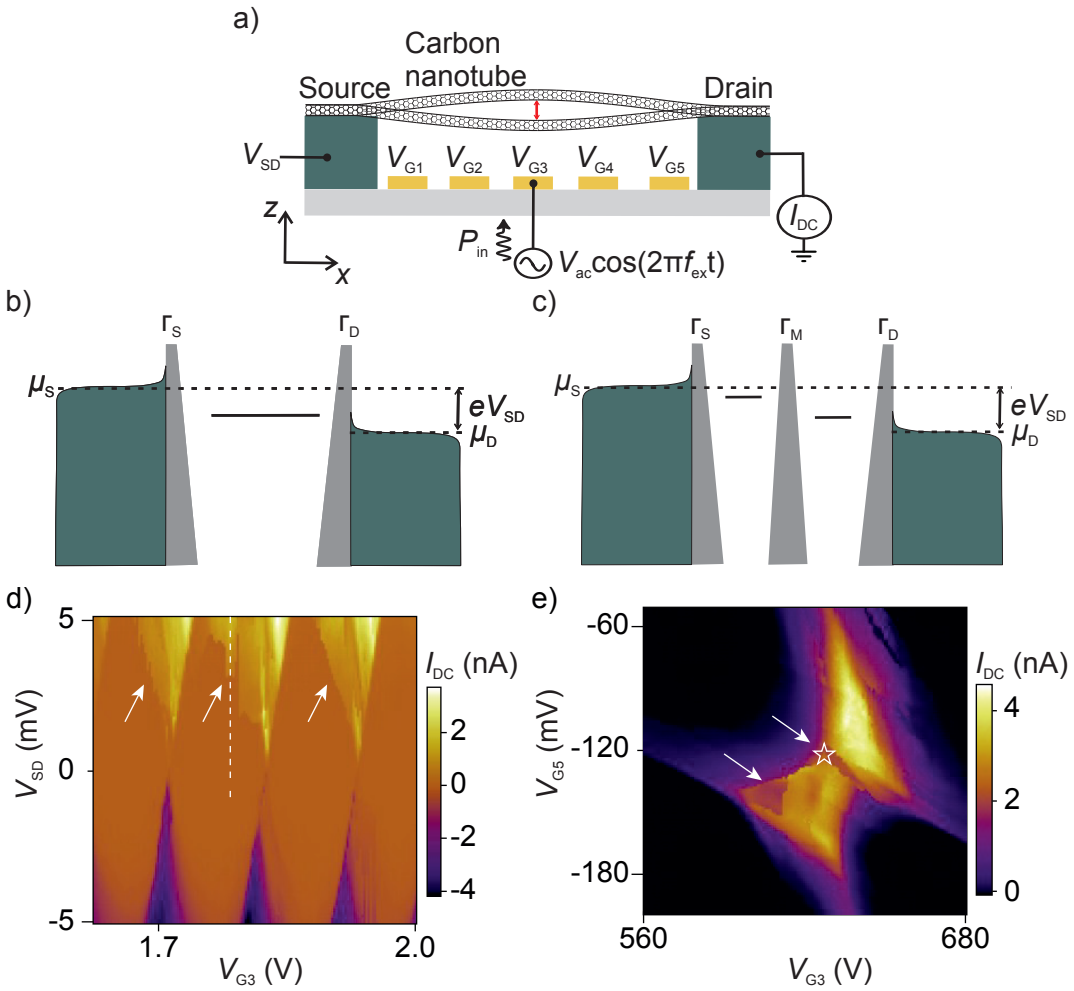


Figure 5.1: a) A CNT suspended over two metal electrodes. Five gate voltages, $V_{\mathrm{G1\text{-}G5}}$, are used to create either a single dot or a double dot. **b,c)** Energy diagrams for single dot and double dot configuration. The source, drain and interdot tunnel rates are indicated and the associated tunnel rates are labeled Γ_{S}, Γ_{D} and Γ_{M}. **d)** Current measured in single-dot configuration as a function of the gate voltage V_{G3} and bias voltage V_{SD}. White arrows point at features which indicate the presence of self-oscillations. The current traces in Figure 5.2(a) were taken along the dashed vertical line. **e)** Current measured in the double-dot configuration by sweeping V_{G5} and stepping V_{G3} with $V_{\mathrm{SD}} = 1.8$ mV. White arrows point at current features which indicate the presence of self-oscillations. The white star indicates a triple point, where we observe the switch in current as a function of V_{SD} plotted in Figure 5.4(a).

5.3 Self-oscillations in single dot configuration

Self-oscillations are identified as sharp switches in current appearing in the absence of an rf excitation [29, 99, 100, 101, 60, 102]. We observe such switches both for single and double dot configurations (Figure 5.1(c,d)). In the single dot configuration, we

observe the bistability through the hysteretic behavior of the current when sweeping V_{SD} in and out of the self-oscillation area, following the vertical white dashed line in Figure 5.1(c), which corresponds to a constant gate voltage $V_{\mathrm{G3}} = 1.8$ V. As V_{SD} is swept upward, a sharp increase of current around $V_{\mathrm{SD}} = 2.3$ mV indicates the onset of self-oscillations (red curve in Figure 5.2(a)). When V_{SD} is swept in the opposite direction (blue curve), the sharp decrease of current is found at a significantly lower voltage $V_{\mathrm{SD}} \simeq 1.3$ mV. The sharp changes in current are reproducible over several sweeps of V_{SD}, with a small variation in threshold voltages due to the stochastic nature of this process. This hysteresis cycle shows that there is a range of bias voltages, $V_{\mathrm{SD}} \simeq 1.3 - 2.3$ mV, labeled as (II) in Figure 5.2, for which the system exhibits bistability.

We can explain the bistability regime observed using a model describing the motion of the CNT as a single vibrational mode of displacement $z(t)$, frequency ω_{m}, and effective mass m, whose evolution equation reads [27, 96, 97]

$$m\ddot{z}(t) = -m\omega_{\mathrm{m}}^2 z(t) - \gamma\dot{z}(t) - g_{\mathrm{m}}n(t) + \xi(t) \tag{5.1}$$

Here $\gamma = m\omega_{\mathrm{m}}/Q$ is the friction coefficient affecting the CNT motion and $n(t) = 0, 1$ is the occupation number of the dot, which is a stochastic variable, and $\xi(t)$ is thermal Gaussian white noise with zero average and $\langle \xi(t)\xi(t') \rangle = 2\gamma k_{\mathrm{B}} T \delta(t - t')$, T being temperature and k_{B} the Boltzmann constant. Gate voltages exert a force on the CNT when the dot is occupied, i.e. $n(t) = 1$. This force depends on several parameters such as the distance between the dot and the gate electrodes. For small oscillations, this force can be considered constant. The constant g_{m} determines the strength of the coupling between the dot charge and the mechanics.

The stochastic occupation number $n(t)$ undergoes Poissonian jumps whenever electron tunneling occurs [97, 27]. The rates of jumps from the left and right electrodes to the dot are given by $\Gamma_{\mathrm{S/D}}(z) f_{\mathrm{S/D}}(\mu(z))$ and from the dot to the electrodes by $\Gamma_{\mathrm{S/D}}(z)[1 - f_{\mathrm{S/D}}(\mu(z))]$, where $\Gamma_{\mathrm{S/D}}(z)$ are the tunneling rates, and $f_{\mathrm{S/D}}(\mu(z))$ are the Fermi functions of each lead. The electrochemical potential of the dot, $\mu(z) = \mu_0 + g_{\mathrm{m}} z$, depends on the CNT displacement z. The constant μ_0

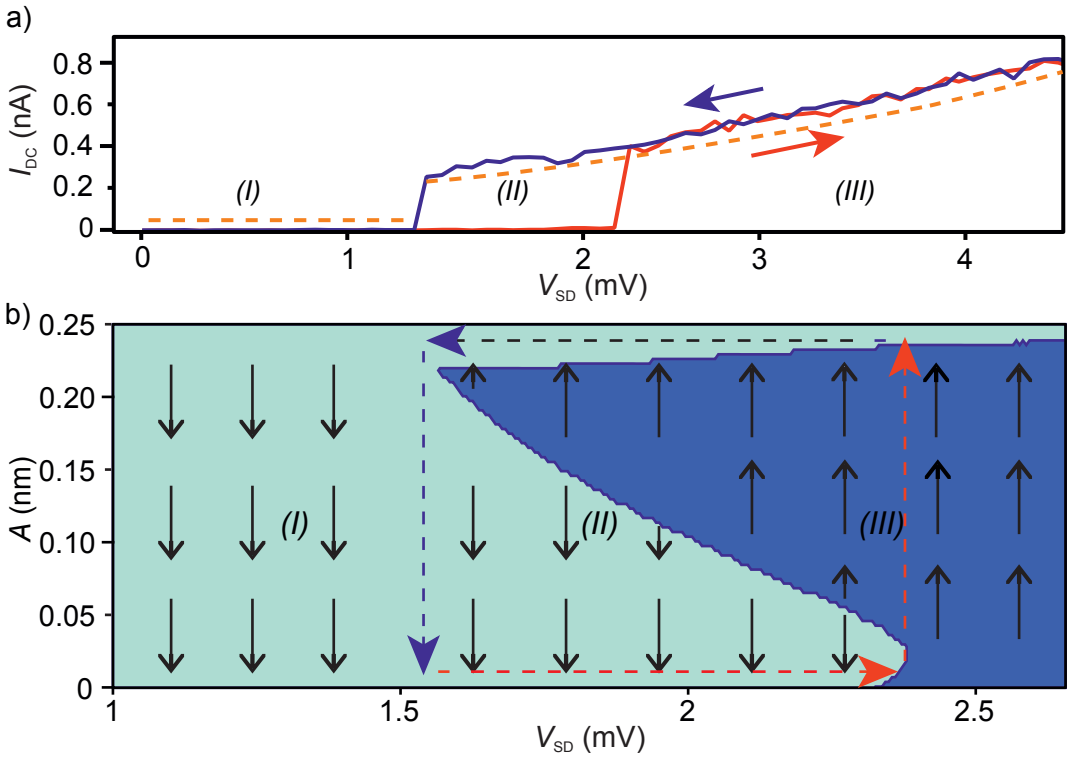


Figure 5.2: a) Hysteresis in I_{DC} as a function of V_{SD} measured in the single dot regime following the dashed line ($V_{G3} = 1.8$ V) in Figure 5.1(c). The red and blue arrows indicate the direction of each sweep. The orange dashed line is the current calculated from Equation (5.5). The numerals (I, II, III) indicate regions of no oscillations, bistability and self-oscillations, respectively. b) Stability diagram: the dark (light) blue areas indicate $\Delta E > 0$ ($\Delta E < 0$) for different values of A and V_{SD}. Small arrows indicate the direction in which A would change in each area given the sign of ΔE. Blue and red arrows delimit regions (I), (II) and (III) and indicate a similar hysteresis cycle as that shown in panel a). We use $\omega_m/2\pi = 270$ MHz, $g_m = 0.01$ eV/nm, $m = 2 \times 10^{-22}$ kg, and $Q = 1000$, $\Gamma_S = 400$ GHz, $\Gamma_D = 18$ GHz, $\alpha_S = 4$ nm^{-1}, and $\alpha_D = 0$.

is the electrochemical potential of the dot in the absence of mechanical motion. Assuming that the energy of the dot reaches the chemical potential μ_S at the onset of self-oscillations and transport, $\mu_0 = eV_S^*$, where V_S^* is the value of V_{SD} at the border between regions (II) and (III) in Figure 5.2(a), i.e., $\mu_0 = 2.25$ meV. The value of g_m can be estimated as in Chapter 4. Notice that the tunneling rates $\Gamma_{S/D}(z)$ depend on the energy of the dot and, consequently, on the displacement z of the oscillations. This inhomogeneity of the tunnel barriers has been found to be a necessary condition for the occurrence of self-oscillations [60, 97, 27, 98].

In the experimental results presented in this chapter, the tunneling rates are

much larger than the mechanical frequency of the CNT, $\Gamma_{\mathrm{S/D}}(z) \gg \omega_{\mathrm{m}}$. Hence, the dynamics of the random variable $n(t)$ are much faster than the CNT's motion. This enables us to approximate the behavior of the system through deterministic dynamics that are influenced by minor fluctuations arising from thermal noise and the random nature of the occupation number $n(t)$. The deterministic dynamics determine the self-oscillations' stability, as demonstrated below, whereas fluctuations are responsible for their generation and decay [63]. Neglecting the thermal noise in Equation (5.1) and replacing the random occupation number $n(t)$ by its average $\bar{n}(t)$, we obtain:

$$\ddot{z}(t) = -\omega_{\mathrm{m}}^2 z(t) - \frac{\omega_{\mathrm{m}}}{Q}\dot{z}(t) - \frac{g_{\mathrm{m}}}{m}\bar{n}(t) \tag{5.2}$$

$$\dot{\bar{n}}(t) = \Gamma_{\mathrm{in}}(z(t))[1-\bar{n}(t)] - \Gamma_{\mathrm{out}}(z(t))\bar{n}(t). \tag{5.3}$$

Equation (5.3) is the master equation for the average occupation number with transition rates $\Gamma_{\mathrm{in}} = \Gamma_{\mathrm{S}} f_{\mathrm{S}}(\mu) + \Gamma_{\mathrm{D}} f_{\mathrm{D}}(\mu)$, and $\Gamma_{\mathrm{out}} = \Gamma_{\mathrm{S}}[1 - f_{\mathrm{S}}(\mu)] + \Gamma_{\mathrm{D}}[1 - f_{\mathrm{D}}(\mu)]$. Eqs. (5.2) and (5.3) are deterministic and predict the appearance of self-oscillations [60]. Here we analyze the stability of these self-oscillations by calculating the exchange of energy between the dot and the CNT's motion. To simplify the analysis, we assume that the leads are at zero temperature, yielding sharp Fermi functions $f_{\mathrm{S,D}}(\mu)$ and that the tunneling rates are given by $\Gamma_{\mathrm{S/D}}(z) = \Gamma_{\mathrm{S/D}} e^{\alpha_{\mathrm{S/D}} z}$ [79], $\alpha_{\mathrm{S/D}}$ being parameters that quantify the inhomogeneity of the barriers.

Self-oscillations were so far explained by proving that the last term in Equation (5.2) acts as negative damping that can counterbalance the energy dissipation term [60]. Another approach to understand the stability of self-oscillations is to consider the energy ΔE that the CNT gains in an oscillation of a given amplitude A. The mechanical energy, $E(t) = m\dot{z}(t)^2/2 + m\omega_{\mathrm{m}}^2 z(t)^2/2$, changes in a single oscillation of period $\tau \equiv 2\pi/\omega_{\mathrm{m}}$ by

$$\Delta E = -m \int_0^\tau \left[\frac{\omega_{\mathrm{m}}}{Q}\dot{z}(t)^2 + \frac{g_{\mathrm{m}}}{m}\dot{z}(t)\bar{n}(t) \right] dt. \tag{5.4}$$

The device thus functions as an engine: the second term in Equation(5.4) is the energy that the electrical current transfers to the mechanical motion, whereas the

first term is the energy dissipated as heat through friction. To calculate ΔE, it is enough to consider harmonic oscillations, $z(t) = A\cos(\omega_{\mathrm{m}}t)$. We solve Equation (5.2) for the average occupation number $\bar{n}(t)$ using this harmonic approximation and then insert the solution into Equation (5.4) to calculate ΔE as a function of A and the other relevant parameters. This approximation is accurate for high Q and relatively small g_{m}.

The stability of an oscillation of amplitude A is given by the sign of ΔE. If the oscillation gains energy, that is, if $\Delta E > 0$, then the amplitude increases. On the other hand, if $\Delta E < 0$, the amplitude decreases. The magnitude of ΔE does not affect the stability of the oscillations, but it is relevant for the spontaneous generation and decay of the self-oscillations. In Figure 5.2(b) we show the areas where ΔE is positive (dark blue) or negative (light blue), depending on the value of the bias voltage V_{SD} and the amplitude A of the oscillation. For the rest of the parameters, we use realistic values based on a fitting of the Coulomb peaks. If the system is oscillating with an amplitude A located in the dark blue region, then the oscillator gains energy in each oscillation and the amplitude increases, as indicated by the vertical arrows, until it reaches the light blue region. On the other hand, the amplitude of the oscillation decreases in the light blue region. We can also distinguish three different regions depending on V_{SD}. In region (I), ΔE is negative for any value of A; therefore, oscillations lose energy and fade out. In region (II), there are both positive and negative values of ΔE, in correspondence with the bistability observed in Figure 5.2(a). In region (III), ΔE is mostly positive, and A reaches a saturation value $A \approx 0.25$ nm. At the boundary between regions (II) and (III), for small values of A, the model also predicts unstable amplitudes. The shape of the dark blue region is given by dissipation.

Our model also provides an estimate of I_{DC},

$$I_{\mathrm{DC}} = \frac{q}{\tau}\int_0^{\tau} \Gamma_{\mathrm{S}}(z(t))\Big[f_{\mathrm{S}}(\mu(z(t))) - \bar{n}(t)\Big]dt. \tag{5.5}$$

We estimate I_{DC} for the $z(t)$ resulting from the saturation value of A. The result, plotted in Figure 5.2(a) (orange dashed curve), shows good agreement with the data (blue and red curves).

We also explore the occurrence and duration of self-oscillations in region (II). The sample is subjected to a protocol where V_{SD} is modified in sequence as shown in Figure 5.3(a). We start the protocol with a low voltage, $V_{KILL} = 0$ mV, for which self-oscillations are absent, and perform a rapid quench to the value $V_{SD} = V_{PROBE}$ that we want to probe. This voltage is kept constant for about 10 seconds to observe the spontaneous onset of self-oscillations revealed by a sudden increase in I_{DC}. V_{SD} is then changed for about a second to a high pump bias voltage $V_{PUMP} = 3$ mV, where self-oscillations are induced. We then move back V_{SD} to V_{PROBE} for the rest of the sequence (about 20 s) to measure the persistence of the self-oscillations. Figure 5.3(a) shows I_{DC} during the protocol for three representative regions. Sudden changes in the current indicate the presence of self-oscillations.

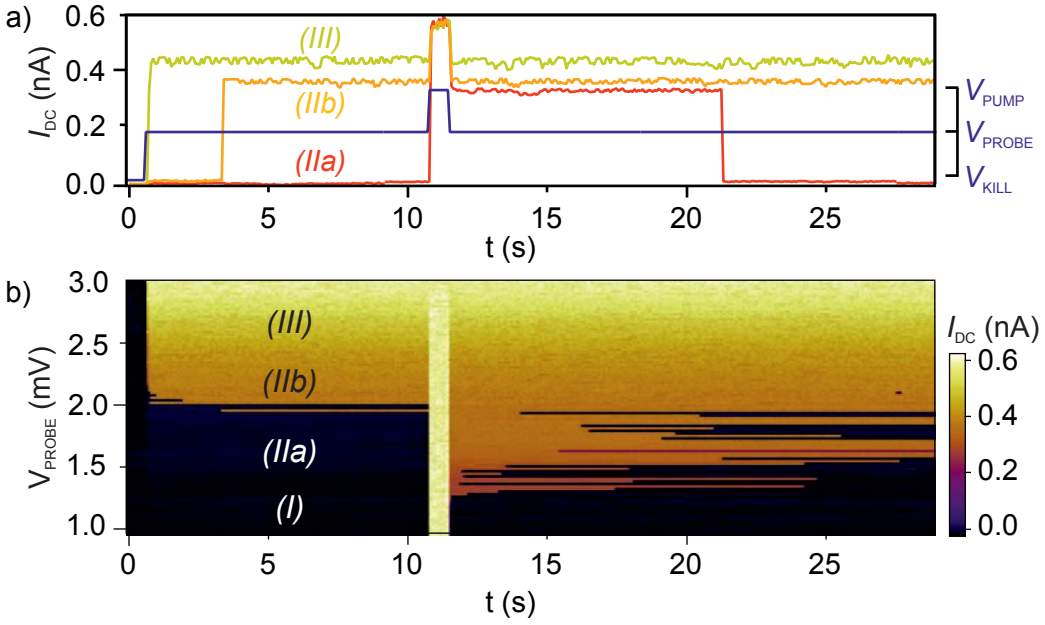


Figure 5.3: a) Sequence of bias voltages V_{SD} applied (blue) and observed current during the protocol for $V_{PROBE} = 1.6$ mV (IIa), 1.98 mV (IIb), and 2.5 mV (III), selected from panel b). The device is in the single-dot configuration (see Figure 5.1(a)). V_{SD} is initially set to $V_{KILL} = 0$ mV to start the protocol with the CNT at rest. Then V_{SD} is increased up to V_{PROBE} for a given time. Self-oscillations are pumped by setting V_{SD} to $V_{PUMP} = 3$ mV. Finally, the persistence of the self-oscillations is measured by setting V_{SD} back to V_{PROBE}. b) Observed current during the protocol for different values of V_{PROBE}. We identify four regions: (I) absence of self-oscillations; (IIa) self-oscillations observed after the pumping step and spontaneously decaying after a random time; (IIb) self-oscillations spontaneously appearing at a bias potential $V_{SD} = V_{PROBE}$; and (III) stable self-oscillations.

Figure 5.3(b) summarizes experimental results for a wide range of V_{PROBE}. We

identify four different regimes associated with the three regions in Figure 5.2. For $0 < V_{\mathrm{PROBE}} < 1.3$ mV, region (I), the absence of current indicates that self-oscillations are not stable. They do not appear spontaneously at $V_{\mathrm{SD}} = V_{\mathrm{PROBE}}$ and vanish immediately after the pumping step. In region (IIa), $1.3 \text{ mV} < V_{\mathrm{PROBE}} < 2.0$ mV, self-oscillations do not start spontaneously but endure during a random time after being triggered by the pumping step. In a small bias voltage range around $V_{\mathrm{PROBE}} \approx 2.0$ mV, region labelled as (IIb), self-oscillations can start spontaneously after some time at V_{PROBE}. Finally, for $V_{\mathrm{PROBE}} > 2$ mV, region (III), self-oscillations are always stable: they start spontaneously at V_{PROBE} and are maintained during the whole protocol.

In the bistable regions, (IIa) and (IIb), self-oscillations appear and vanish due to fluctuations that allow the system to access areas in the stability diagram of Figure 5.2(b) that have the opposite sign of ΔE than that dictated by our deterministic model. The probability of these excursions is very small but can occur after a large number of oscillations. For instance, a self-oscillation of frequency $\omega_{\mathrm{m}}/2\pi \sim 270$ MHz can last for 20 seconds or 5.4×10^9 oscillations. One can identify two main sources of fluctuations: the thermal noise affecting the motion of the nanotube and quantum noise due to tunneling. The latter is much larger than the former, but is present only when a current flows through the CNT.

5.4 Self-oscillations in double dot configuration

We perform a similar study when the device is in the double-dot configuration by measuring the hysteresis as a function of V_{SD} (Figure 5.4(a)) at the point designated by the white star in Figure 5.1(d). The sharp changes in current are reproducible over several sweeps of V_{SD} for a different thermal cycle of the device, with a small variation in threshold voltages due to the stochastic nature of this process. In the double dot configuration, the hysteretic switches define regions (i) to (iv). In region (iii) we observe current values showing self-oscillations, while in regions (i) and (v) these self-oscillations seem not to be present.

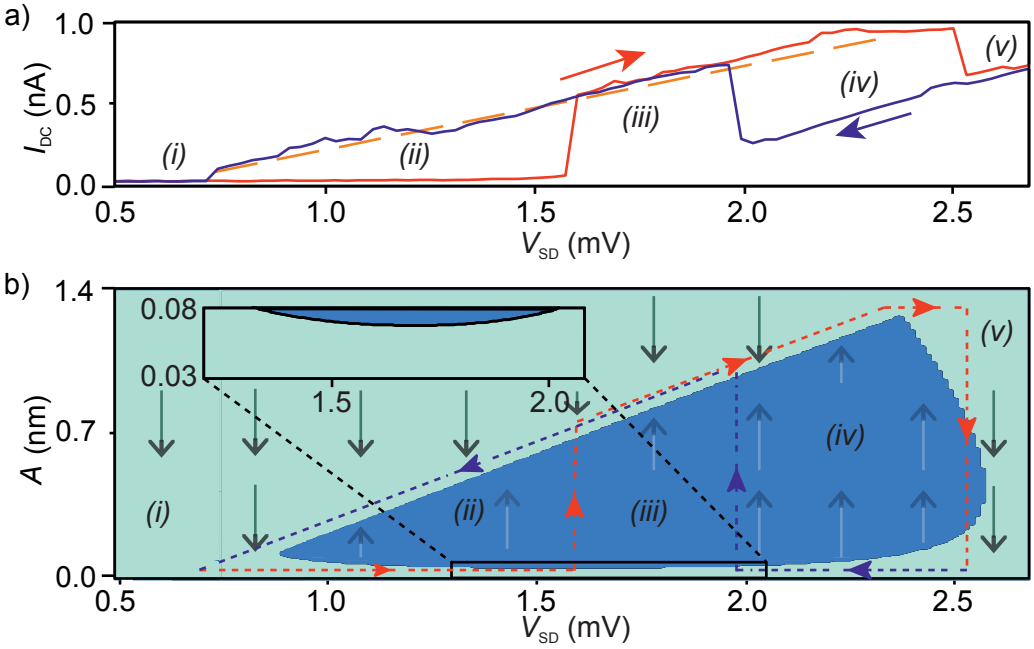


Figure 5.4: a) Current switch hysteresis as function of V_{SD} in the double-dot configuration, measured at the location of the white star in Figure 5.1(e) ($V_{\mathrm{G3}} = 620$ mV, $V_{\mathrm{G5}} = -120$ mV). Red and blue arrows indicate the direction of each current sweep. The dashed orange line shows the current calculated from Equation (5.5) with $\Gamma_{\mathrm{M}} = \omega$, $\sigma = 0.1$ nm and amplitude 1 nm. The numerals (i, ii, iii, iv, v) indicate different regions in the stability diagram. b) Stability diagram: the dark (light) blue areas indicate $\Delta E > 0$ ($\Delta E < 0$) for different values of A and V_{SD}. Small arrows indicate the direction in which A would change in each area given the sign of ΔE. Blue and red dashed lines delimit regions (ii), (iii) and (iv). Blue and red arrows indicate a similar hysteresis cycle as that shown in panel a). Inset: zoom in on areas approaching zero amplitude. We use $\omega_{\mathrm{m}}/2\pi = 270$ MHz, $g_{\mathrm{m}} = 0.01$ eV/nm, $m = 2 \times 10^{-22}$ kg, and $Q = 1000$.

These current switches can be explained by our model under the assumption that the motion of the CNT mostly affects the electrochemical potential of one of the dots. This assumption is justified by the estimation of capacitive coupling of the dots to the gate electrodes which indicates that one of the dots is primarily controlled by V_{G3}, whilst the other is mainly controlled by V_{G5}. The electrochemical potential of the second dot can thus be considered aligned with $\mu_{\mathrm{D}} = 0$. In this case, the system is similar to the one-dot case but replacing the transport between the dot and the rightmost electrode by tunneling between the two dots occurring when their electrochemical potentials are aligned, i.e., when $z(t)$ is close to zero; in the model, this interdot exchange is represented by the rate Γ_{M} and a width σ, $\Gamma_{\mathrm{out}}(z) \sim \Gamma_{\mathrm{M}} \exp -z^2/\sigma^2$. Notice that, contrary to the case of a single dot,

self-oscillations disappear for high bias voltages V_{SD} (region (v)). This phenomenon is difficult to explain with the model outlined above, since V_{SD} simply determines the location of the leftmost Fermi level μ_{S} and should not affect the stability of self-oscillations. However, according to Equation (5.4), self-oscillations are maintained by a correlation between the charge of the dot $n(t)$ and the instant velocity of the CNT, $\dot{z}(t)$. This correlation could be lost due, for instance, to inelastic co-tunneling, which is present for high values of V_{SD} .

For the double-dot case, which now considers interdot tunneling and an inelastic contribution to the current proportional to V_{SD}, we obtain the current shown in Figure 5.4(a) (orange line) and the stability diagram depicted in Figure 5.4(b). The stability diagram shows good agreement with the measured current switches as a function of V_{SD} in upwards (red) and downwards (blue) sweeps, although the boundaries of region (iii) are not precisely located due to its stochastic nature. We can also observe that the area with $\Delta E < 0$ (light blue) appears close to zero A in region (iii) (inset). This would indicate that the rest position of the CNT is unstable and self-oscillations can be easily induced by fluctuations, a picture which is supported by the measurements of the onset of self-oscillations in region (iii) .

5.5 Theoretical model

In this section, we describe the theoretical model for the coupling between the quantum dot and the mechanical oscillator. Similar models have been used in theoretical and experimental works [27, 97, 60]. Since the quantum dot is strongly coupled to the right and left electrodes, the system behaves classically [112]. The evolution of the vertical position z of the CNT is described by an underdamped Langevin equation

$$\ddot{z} = -\omega_{\mathrm{m}}^2 z - \frac{\omega_{\mathrm{m}}}{Q}\dot{z} - \frac{g_{\mathrm{m}}}{m}n + \xi. \tag{5.6}$$

Here, ω_{m} is the resonance frequency of the oscillator, Q the quality factor, m the oscillator mass, g_{m} the coupling constant between the oscillator and n the electron occupation. The term $-\frac{g_{\mathrm{m}}}{m}n$ represents, precisely, the electrostatic force acting on

the CNT due to the electron occupation. ξ represents the environmental thermal noise, following $\langle \xi(0)\xi(t)\rangle = 2\gamma k_{\mathrm{B}} T\delta(t)$, with T the environment temperature, k_{B} the Boltzmann constant and $\gamma = m\omega_{\mathrm{m}}/Q$ the damping constant.

The occupation $n = 0, 1$ evolves following a dichotomic stochastic process. During each time interval dt, the transition $n = 0 \to 1$ takes place with probability $\Gamma_{\mathrm{in}}dt$, and $n = 1 \to 0$ with probability $\Gamma_{\mathrm{out}}dt$. $\Gamma_{\mathrm{in/out}}$ are the energy-dependent tunnel rates. The average occupation $\bar{n}$ evolves then following the master equation

$$\dot{\bar{n}} = \Gamma_{\mathrm{in}}[1 - \bar{n}] - \Gamma_{\mathrm{out}}\bar{n}. \tag{5.7}$$

5.5.1 Mean-field approximation

For a large quality factor Q and tunnel rates $\Gamma_{\mathrm{in/out}}$, the time required for the mechanics to thermalize becomes longer than the time required by n to equilibrate. In this case, both fluctuations in occupation and position are negligible, and we consider just the deterministic system of equations

$$\dot{\bar{n}} = \Gamma_{\mathrm{in}}[1 - \bar{n}] - \Gamma_{\mathrm{out}}\bar{n}, \tag{5.8}$$

$$\ddot{z} = -\omega_{\mathrm{m}}^2 z - \frac{\omega_{\mathrm{m}}}{Q}\dot{z} - \frac{g_{\mathrm{m}}}{m}\bar{n}, \tag{5.9}$$

which corresponds to a *mean-field approximation.*

5.5.2 Mechanical energy

The CNT mechanical energy under the mean-field approximation is

$$E = \frac{1}{2}m\dot{z}^2 + \frac{1}{2}m\omega_{\mathrm{m}}^2 z^2. \tag{5.10}$$

Taking the time derivative and using equations (5.8) we obtain

$$\frac{dE}{dt} = -m\frac{\omega_{\mathrm{m}}}{Q}\dot{z}^2 - g_{\mathrm{m}}\dot{z}\bar{n}. \tag{5.11}$$

If $z(t), \bar{n}(t)$ is a given trajectory of Eqs.(5.8), the change in mechanical energy in a certain time τ is

$$\Delta E = -\int_0^\tau \left[m\frac{\omega_{\mathrm{m}}}{Q}\dot{z}^2(t) + g_{\mathrm{m}}\dot{z}(t)\bar{n}(t)\right] dt. \tag{5.12}$$

5.6 Decay of self-oscillations

The switching between states in the bistability region finds its origin in the thermal and electric noise (see Equation (5.6)). In order to clarify this, we identify the bistability in terms of the double-well problem [113, 114, 96] in the single-dot configuration. We now consider a long timescale $T_A \gg 1/\omega_{\rm m}$ where the amplitude of oscillation will vary with time. In this timescale, we consider an effective Langevin equation for mechanical energy,

$$\frac{dE}{dt} = f(E) + \xi_E, \tag{5.13}$$

where $f(E) = \Delta E/\tau$ is the average increment of energy per unit of time, and ΔE is given by Equation (5.4). Note that the value of ΔE depends on the amplitude of the oscillations, and therefore on the mechanical energy, $E = m\omega_{\rm m}^2 A^2/2$. $\tau = 2\pi/\omega_{\rm m}$ is the period of the oscillation. ξ_E is a noise containing both electrical and thermal fluctuations and will depend on the actual value of the energy. Equation (5.13) can be written considering an effective "potential" given by

$$U(E) = -\frac{1}{\tau}\int_0^E \Delta E(E')dE', \tag{5.14}$$

then,

$$\frac{dE}{dt} = -\frac{dU}{dE} + \xi_E. \tag{5.15}$$

In Figure 5.5, we represent the effective potential $U(E)$ (red line), evaluated using harmonic trajectories $z(t) = A\cos\omega_{\rm m}t$. Here, the problem is explicitly analogous to the typical double-well potential in energy space. In that figure, self-oscillations correspond to the right well, A, with a certain energy associated. The other well, C, corresponds with the motionless state. Switching between both states will happen when a fluctuation puts the system over the barrier B.

We use equation (5.6) to simulate one trajectory in the self-oscillation state for 10^4 oscillation periods. The histogram of this trajectory is included in Figure 5.5 (blue). This histogram is sharply peaked in the point A, and therefore a very large number of mechanical periods are required for the self-oscillations to vanish.

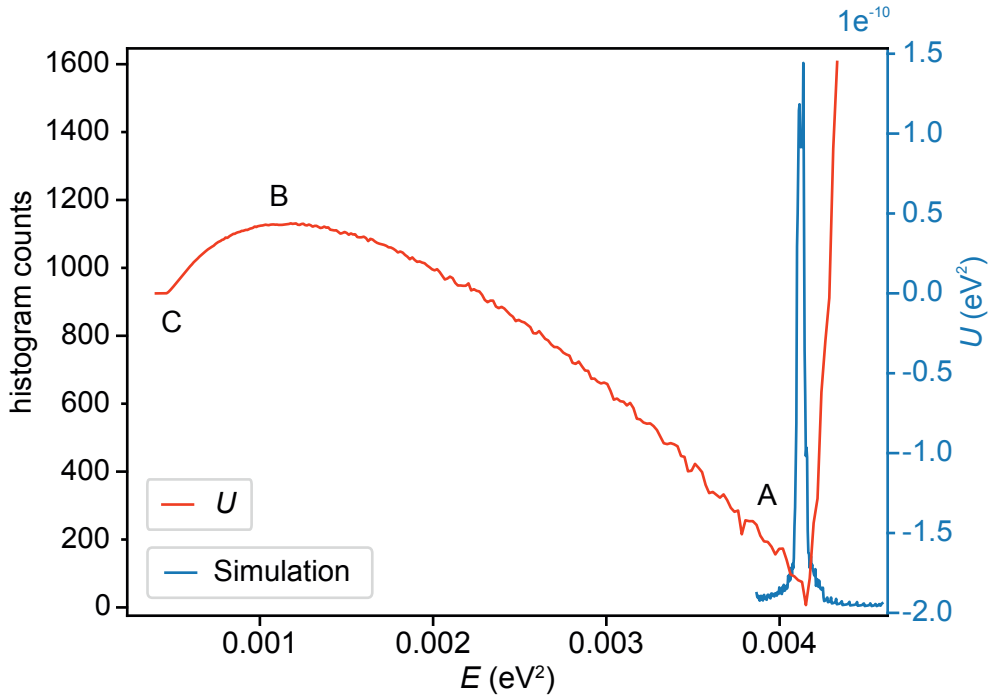


Figure 5.5: Numerical computation of the effective potential $U(E)$ (red) and stochastic simulation of a single trajectory (blue) as a function of the mechanical energy for the one dot-configuration. The sharp peak in U at the point A is due to the end of the borders of the conduction region of the device. The letters A, B, C indicate the stable oscillation points (A, C) and the tipping point between both regimes (B). The parameters are $\omega/2\pi = 270$ MHz, $g_{\rm m} = 0.01$ eV/nm, $m = 2 \times 10^{-22}$ kg, $Q = 1000$, $\Gamma_{\rm S} = 400$ GHz, $\Gamma_{\rm D} = 18$ GHz, $\alpha_{\rm S} = 4$ nm^{-1}, and $\alpha_{\rm D} = 0$.

According to this, the self-oscillation duration is given by the shape of the barrier. In the region (II) of Figure 5.2, the size of the barrier increases with the bias voltage $V_{\rm SD}$, generating longer and longer self-oscillations in that region. This increase in duration is observed in Figure 5.2 along region (IIa).

5.7 Double-dot case

As in the earlier section, the gate voltages inducing the configurations are $V_{\rm G3}$ and $V_{\rm G5}$. One of the dots is located close to the center of the CNT and can move as in the single-dot configuration, while the second one is positioned near the rightmost end of the CNT and remains static. This system is similar to the one-dot case but replacing the transport between the moving dot and the right lead by an effective tunneling rate with the form $\Gamma_{\rm dot-dot}(z) = \Gamma_{\rm M} \exp -z^2/\sigma^2$. The width σ represents

the effects of the thermal noise on the moving dot.

However, contrary to the case of a single dot, self-oscillations disappear for high bias voltages V_{SD}. This happens as a result of the inelastic current, promoting transport even between misaligned dots [73, 115]. In (iii, iv, v) we will calculate inelastic transport in a completely effective way, including homogeneous transport rates $\Gamma^{\mathrm{ie}}(V_{\mathrm{SD}})$ in the master equation,

$$\Gamma_{\mathrm{in}}(z) = \Gamma_{\mathrm{S}}(z) f_{\mathrm{S}}(\mu(z)) + \Gamma^{\mathrm{ie}}(V_{\mathrm{SD}}) \tag{5.16}$$

$$\Gamma_{\mathrm{out}}(z) = \Gamma_{\mathrm{S}}(z)[1 - f_{\mathrm{S}}(\mu(z))] + \Gamma_{\mathrm{dot-dot}}(z) + \Gamma^{\mathrm{ie}}(V_{\mathrm{SD}}), \tag{5.17}$$

and obtaining their value from the motionless state. In regions (i, ii) we state $\Gamma^{\mathrm{ie}}(V_{\mathrm{SD}}) = 0$ for every V_{SD}.

For the double-dot configuration, we have implemented a similar protocol as for the single-dot configuration in Figure 3 (Figure 5.6(a)). The measurement is performed at the coordinates of the white star in Figure 1e, in the same configuration as in Figure 4. The pump voltage $V_{\mathrm{PUMP}} = 1.8$ mV is chosen in the area where the self-oscillations are always on (Figure 5.6(b)).

From the current measurement, depicted in Figure 5.6(b), we identify different behaviors depending on V_{SD}. In (i) and (ii), self-oscillations never start spontaneously, whereas in (iii) they start spontaneously just after the kill step. After the pump step, in regions (i) and (v) self-oscillations stop immediately. In regions (ii) and (iv) the triggered self-oscillations are sustained for a duration too long to be observed in the time frame of this experiment. In the border between regions (iv) and (v) the self-oscillation time decays in a similar way as observed in the single-dot configuration.

5.8 Fitting of the Coulomb peak and tunneling rates

We fit the Coulomb diamond in the single dot configuration to estimate the tunneling rates parameters $\Gamma_{\mathrm{S/D}}$ and $\alpha_{\mathrm{S/D}}$. The fitting procedure is similar to Chapter 4 with the addition of energy-dependent tunneling rates, represented by the parameter

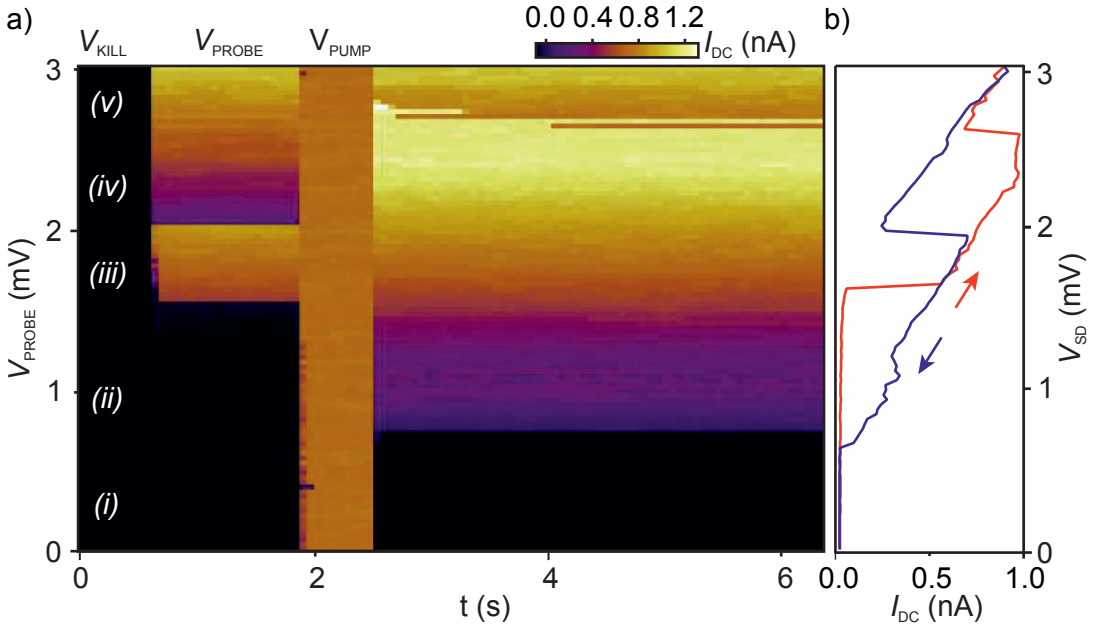


Figure 5.6: a) Voltage bias sequence applied to measure panel b). First, any self-oscillations are killed setting V_{SD} to $V_{\mathrm{KILL}} = 0$ mV, then V_{SD} is set to the target voltage V_{PROBE}. About 1.5 s later, V_{SD} is set to $V_{\mathrm{PUMP}} = 1.8$ mV to start self-oscillations for about 0.5 s. Finally, the voltage is set back to the target V_{SD}. b) Current measured by repeating the sequence shown in panel a) for different V_{PROBE}. The different behaviors are classified in five areas: (i) absence of self-oscillations, (ii) self-oscillations observed after the pumping step, (iii) self-oscillations spontaneously appearing, (iv) self-oscillations observed after the pumping step and spontaneously decaying after a random time, (v) absence of self-oscillations. c) IV measurement with the two sweep direction in the configuration of panel b) showing the current switch hysteresis; same as Figure 5.4(a).

$\alpha_{\mathrm{S/D}}$, following Ref. [79]. The rates of charges tunneling in and out between the source or drain and the quantum dot are given by the expression:

$$\Gamma^{\mathrm{in}}_{\mathrm{S/D}}(\mu) = \Gamma_{\mathrm{S/D}} \exp(\alpha_{\mathrm{S/D}}\mu/g_{\mathrm{m}})\ \rho_{\mathrm{S/D}}(\mu), \tag{5.18a}$$

$$\Gamma^{\mathrm{out}}_{\mathrm{S/D}}(\mu) = \Gamma_{\mathrm{S/D}} \exp(\alpha_{\mathrm{S/D}}\mu/g_{\mathrm{m}}) \left(1 - \rho_{\mathrm{S/D}}(\mu)\right), \tag{5.18b}$$

where μ is the energy of the dot and $f_{\mathrm{S/D}}$ are the Fermi distribution. The overlap between the density of states of the quantum dot and left/right reservoirs is given by:

$$\rho_{\mathrm{S/D}}(\mu) = \frac{1}{2} + \frac{1}{\pi} \arctan\left(\frac{2(\mu_{\mathrm{S/D}} - \mu)}{\hbar\Gamma_{\mathrm{tot}}}\right). \tag{5.19}$$

Finally, the current across the quantum dot is:

$$I(\mu) = e\frac{\Gamma^{\mathrm{in}}_{\mathrm{S}}(\mu)\Gamma^{\mathrm{out}}_{\mathrm{D}}(\mu) - \Gamma^{\mathrm{in}}_{\mathrm{D}}(\mu)\Gamma^{\mathrm{out}}_{\mathrm{S}}(\mu)}{\Gamma_{\mathrm{tot}}}. \tag{5.20}$$

We fit the experimental the Coulomb diamonds in Figure 5.7(a) by cutting it into multiple Coulomb peak with bias ranging from $V_{SD} = 0$ mV to $V_{SD} = 0.9$ mV (Figure 5.7(b)). We fit these Coulomb peaks with a unique set of parameters to obtain $\Gamma_S = 400$ GHz, $\Gamma_D = 15$ GHz, $\alpha_D/g_m = 0$ eV^{-1} and $\alpha_S/g_m = 400$ eV^{-1}.

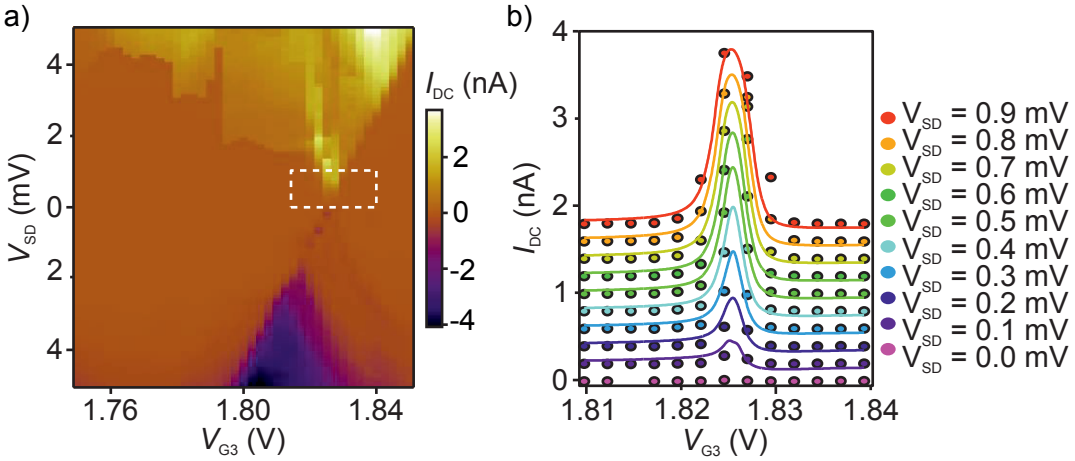


Figure 5.7: Coulomb diamond and fit. a) Zoom on the Coulomb diamond from Figure 1d. The white dashed rectangle represent the area from which are obtained the cut of panel b). b) Set of cuts of panel a) at different bias (circles) and fitting curves (lines). For each bias, the cuts and fit are vertically offset by 0.2 nA from the previous bias. The fitting parameters of the all set are: $\Gamma_S = 400$ GHz, $\Gamma_D = 15$ GHz, $\alpha_S/g = 0$ eV^{-1}, $\alpha_D/g = 400$ eV^{-1} and $V_0 = 1.826$ V. The lever arm 0.18 eV/V is obtained from panel a).

To take into consideration the voltage drop at the IV converter internal resistance (100 kΩ), we reduce the bias of the fit by $V_{SD}^{Corr}(V_{G1}) = V_{SD} - I(V_{G3})R_s$. Because the density of the point of the measurement is not sufficient, we calculate V_{SD}^{Corr} from a first fit of the Coulomb peaks. We then fit again the peaks considering the corrected bias voltage. The contribution of this correction on the final result is small.

5.9 Stability diagram

Here we show a large measurement of the stability diagram of the CNT going from the single dot to the double dot configurations during the cool down run of the main paper results.

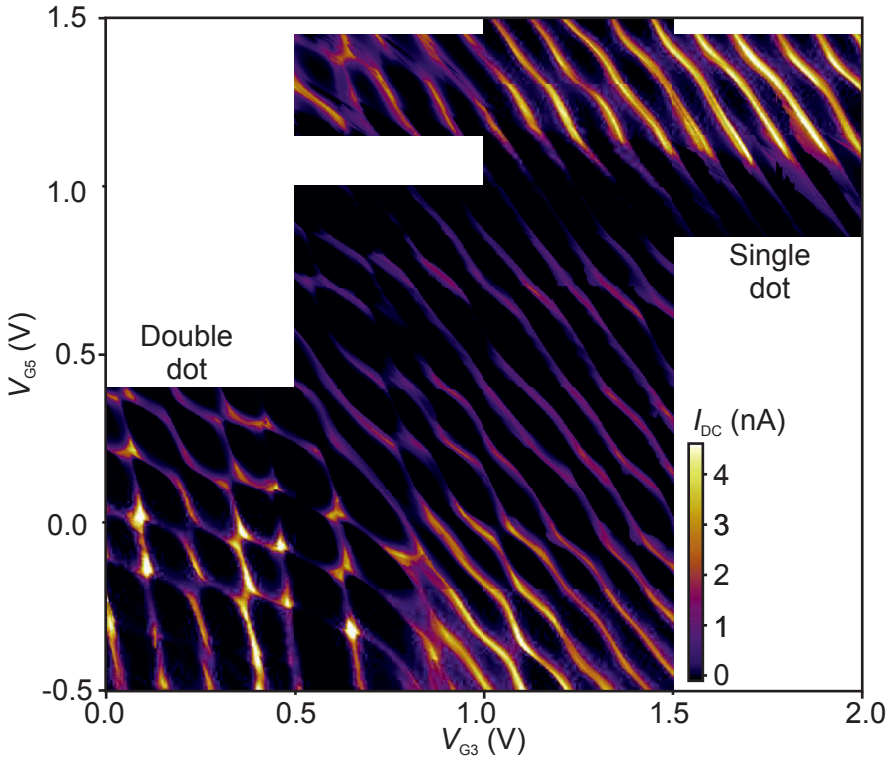


Figure 5.8: Stability diagram containing the single quantum dot and double quantum dot regime measured at $V_{SD} = 3$ mV.

5.10 Additional results

Here we present additional results obtained with the same device but during a different cool down. The device was thermocycled to 300 K between the measurements shown earlier and the ones presented in the following sections.

5.10.1 Self Oscillations in double quantum dots

In Figure 5.9(a) and Figure 5.9(b) we show the measurement of a bias triangle with positive and negative bias voltages ($V_{SD} = \pm 4$ mV) showing that the device is in the double quantum dot configuration. We measure the hysteresis of the self-oscillations (Figure 5.9(e)) at the coordinates of the white star in Figure 5.9(b), located in the edge of the self-oscillation area. The hysteresis is measured multiple time in a row and show a bistability region from $V_{SD} = -4$ mV to $V_{SD} = -2$ mV. Following the homogeneous area from the white star, evidence of self-oscillations are visible one particular edge of one of the triangle in both bias polarity. This edge correspond

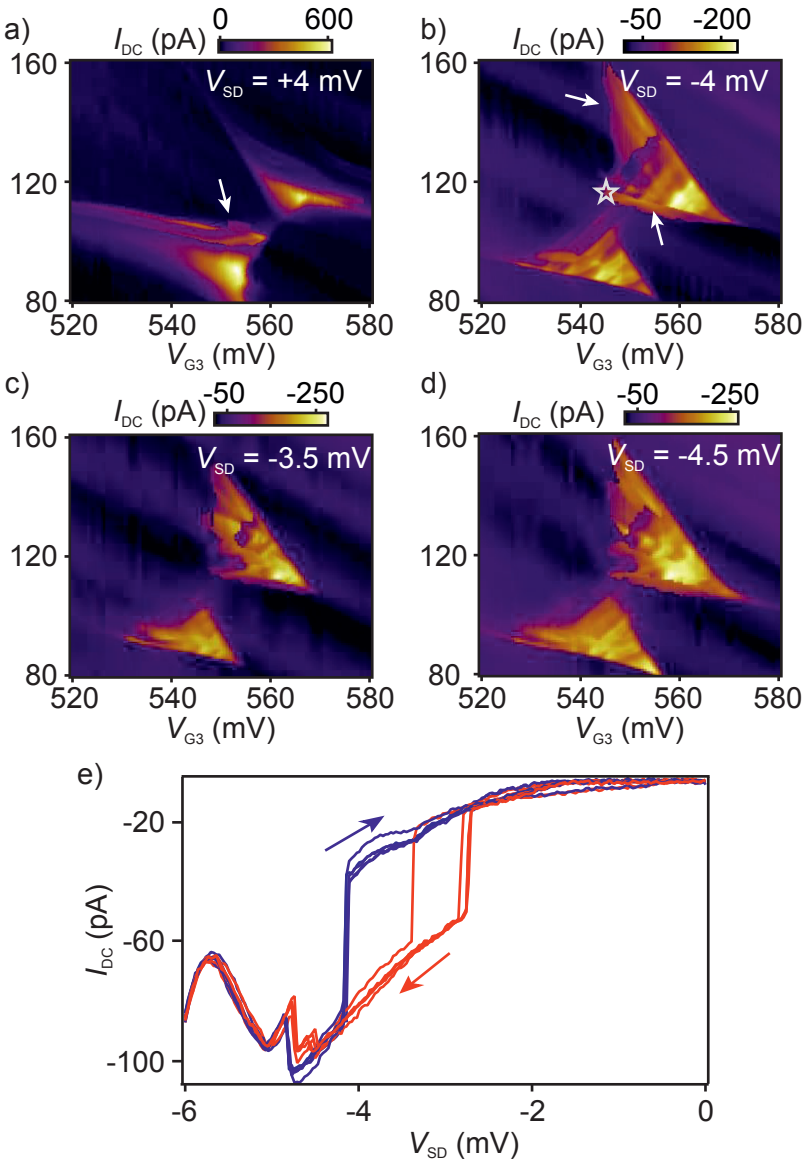


Figure 5.9: Results obtained for the same device but during a different cool down than the results presented in earlier sections. a,b) Bias triangles measured on the double quantum dot regime for $V_{SD} = +4$ mV (a) and $V_{SD} = -4$ mV. Self-oscillations are visible on the edge of one of the triangles highlighted by the arrow. c,d) Measurements of self-oscillations in the same conditions as panel (b)but with $V_{SD} = -3.5$ mV and $V_{SD} = -4.5$ mV for panel (c) and (d) respectively. e) Self-oscillation hysteresis measured at the position of the white star in panel (b). We report five sweeps forward sweep (blue), and five backward sweep (red). The sweep direction is indicated by arrows.

to the chemical potential of one of the two dots (the same in both polarity) align with the chemical potential of the contact lead of its side [73]. Self-oscillations are also observed on the same side of the bias triangles for bias voltages ranging from -3.5 mV to -4.5 mV, see Figure 5.9(b,c,d).

We show the mechanical nature of the current switch that we associate with self-oscillations, we use a rf excitation, applied to one of the gate electrodes, to drive the CNT and excite self-oscillations. This is shown in Figure 5.10. First, we reveal the mechanical resonance frequency $\omega = 262$ MHz in Figure 5.10(a) by measuring the current as a function of the rf drive frequency f_{ex} and power P_{in}. The mechanical quality factor, $Q \approx 2000$, is estimated from the width at a half minimum of the peak in current displayed in Figure 5.10(b)

We then apply the rf excitation while the device is in a bistability region (white arrow in Figure 5.9(b), $V_{\text{SD}} = -3$ mV). For each pixel in Figure 5.10(c), the bias voltage V_{SD} is initially set to $V_{\text{SD}} = 0$ mV for 0.1 s to kill any self-oscillations and then set back to $V_{\text{SD}} = -3$ mV for an other 0.1 s, when the current is measured. Most of the times, the self-oscillations consistently restart when the drive frequency is near ω. This result evidences a mechanical pumping of the self-oscillation at much reduced power P_{in} when the frequency of the excitation f_{ex} is close to natural resonance frequency.

5.10.2 Statistics for the duration of self-oscillations

In Figure 5.11, we show a statistical measurement of the self-oscillation time in the same experimental run as Figure 5.9 and 5.10. First, we prepare the device in the bistability region at the gate voltage coordinates corresponding to the white star in Figure 5.9(b). Then, we excite self-oscillations for about 5 s by setting the bias voltage to $V_{\text{SD}} = -4$ mV, setting for which self-oscillations are always ON (see Figure 5.9(c)). We then change the bias voltage to probe the bistability region ($V_{\text{SD}} = -3$ mV for Figure 5.11(a) and -3.2 mV for Figure 5.11(c)) and measure the current with a rate of approximately 1 point per second. When the current falls below a certain threshold, the measurement stops and the sequence restarts to the next column (saving significant measurement time). We ran 200 sequences for each figure (5.11(a) and 5.11(c)), displaying a series of vertical lines from which we can extract the duration of the self-oscillations.

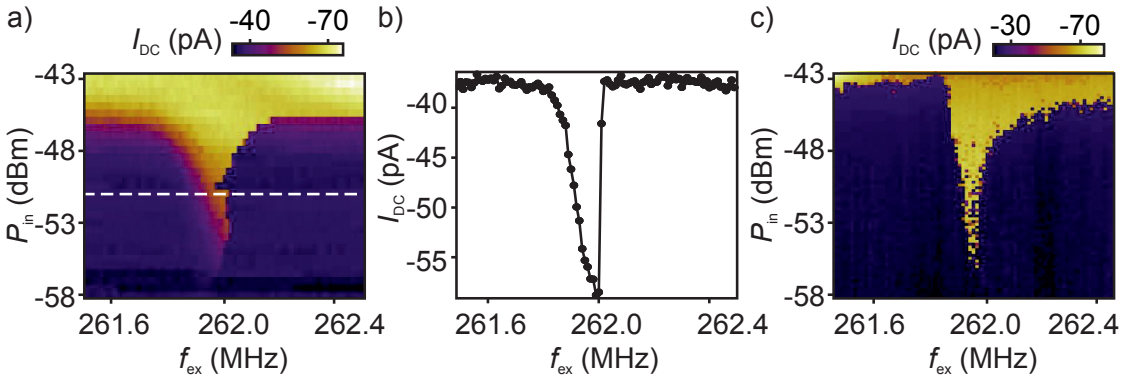


Figure 5.10: Mechanical quality factor and mechanical assisted self-oscillations: a) Current measured as a function of the rf excitation at frequency $\omega_e/2\pi$ and power P_{in}. The source-drain bias is set to $V_{SD} = -4$ mV in a region without self-oscillations, (see Figure 5.9(e)). The white dashed lines indicate the position of the line cut in panel (b). b) Line-cut of panel (a) at $P_{drive} = -51$ dBm (white dashed line). From the width of the dip at half minimum, we estimate a mechanical quality factor of $Q \approx 2000$. c) Current measured as a function of the rf excitation at frequency $\omega_e/2\pi$ and power P_{in}. Here $V_{SD} = -3$ mV is set in the middle of the bi-stable region (see Figure 5.9(e)) marking the presence of self-oscillations. Mechanically assisted self-oscillations are induced by applying a continuous rf-excitation $\omega_e/2\pi$ near the mechanical resonance frequency. The measurement is performed at a location marked by the star marker in Figure 5.9(b). For each pixel self-oscillations are initially suppressed by setting $V_{SD} = 0$ mV for 0.1 s, and then set to -3 mV while measuring the current for 0.1 s. The bright pixels indicate high negative current and mark the points where self-oscillations are present.

We plot a histogram of the duration of the self-oscillations in Figure 5.11(b) and 5.11(d). We note a pattern, particularly visible in Figure 5.11(c), where long lived self-oscillations are followed by a rather repetitive number of short lived self-oscillations. In time domain, this correspond to an approximate 8 min period, in which the first 3 min shows a few long lived self-oscillations and the next 5 min a series of short lived self-oscillations. This regular variability of self-oscillations suggests an influence of external sources which could not be identified.

5.10.3 Temperature dependence

In yet another cool down run, we measure self-oscillations in the Coulomb blockade regime under various temperature conditions. In Figure 5.12, we show the positive side of a Coulomb diamond, showing a region where self-oscillations are evident. The self-oscillations are first measured at 60 mK (base temperature of the cryostat) under both bias sweep directions (two leftmost panels in Fig 5.12) in order to

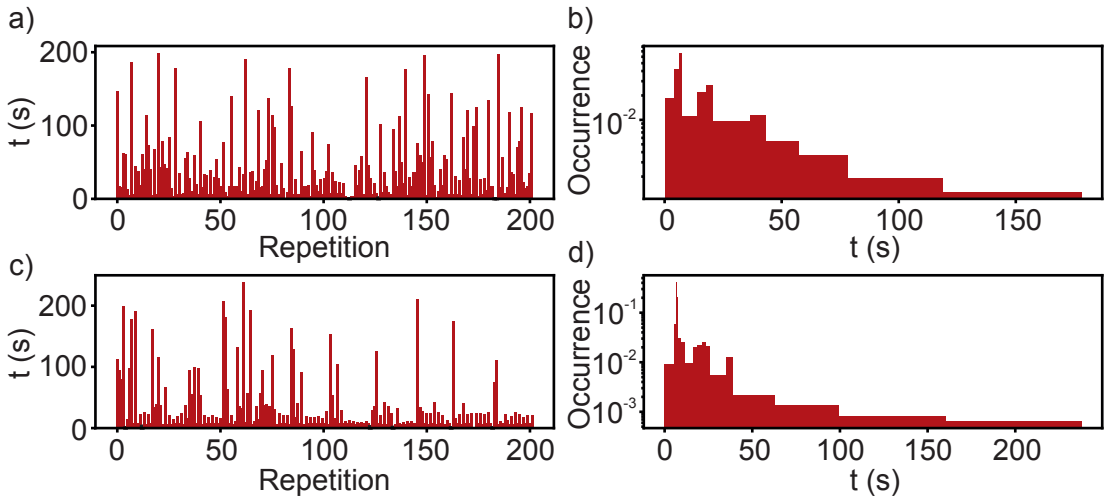


Figure 5.11: a,b) 200 measurements in a row of the duration of self-oscillations for two different values of V_{SD}. For each vertical line, the self-oscillations are first excited by setting the bias voltage to $V_{\mathrm{SD}} = -4$ mV for about 5 s then the bias is set to the target voltage $V_{\mathrm{SD}} = -3$ mV (a) or $V_{\mathrm{SD}} = -3.2$ mV (c). Then we measure the current at a rate of about one point per second. We detect the stop of the self-oscillation when the current falls below a pre-determined threshold. The top of each row indicates the duration of the self-oscillations. b,d) Histograms of the duration of self-oscillation for (a) and (c), respectively.

highlight a bistability region. Then the same Coulomb diamond was measured at increasing cryostat temperatures up to a maximum of 820 mK (other panels in Figure 5.12). Note that a 20 mK uncertainty in the device temperature should be considered to take into account the thermalization of the chip. We saw that the self-oscillation area decreases progressively, starting from the regions further away from the Coulomb diamond, as the temperature rises.

The damping of self-oscillations at high temperatures can be explained by the dispersion of the dynamics due to fluctuations. This magnitude can be estimated as $\sigma_z^{\mathrm{therm}} \sim \sqrt{k_{\mathrm{B}}T/m\omega_{\mathrm{m}}^2}$, where k_{B} is the Boltzmann constant and T is the cryostat temperature. For $T = 60$ mK, it takes the value $\sigma_z^{\mathrm{therm}} \simeq 3.7 \times 10^{-2}$ nm; since this value is orders of magnitude smaller than the amplitude of the self-oscillations, its effect on the oscillations is negligible. However, for $T = 1$ K the dispersion is $\sigma_z^{\mathrm{therm}} \simeq 0.14$ nm. In this regime, the dispersion in the dynamics due to temperature is of the size of the self-oscillations, preventing their appearance.

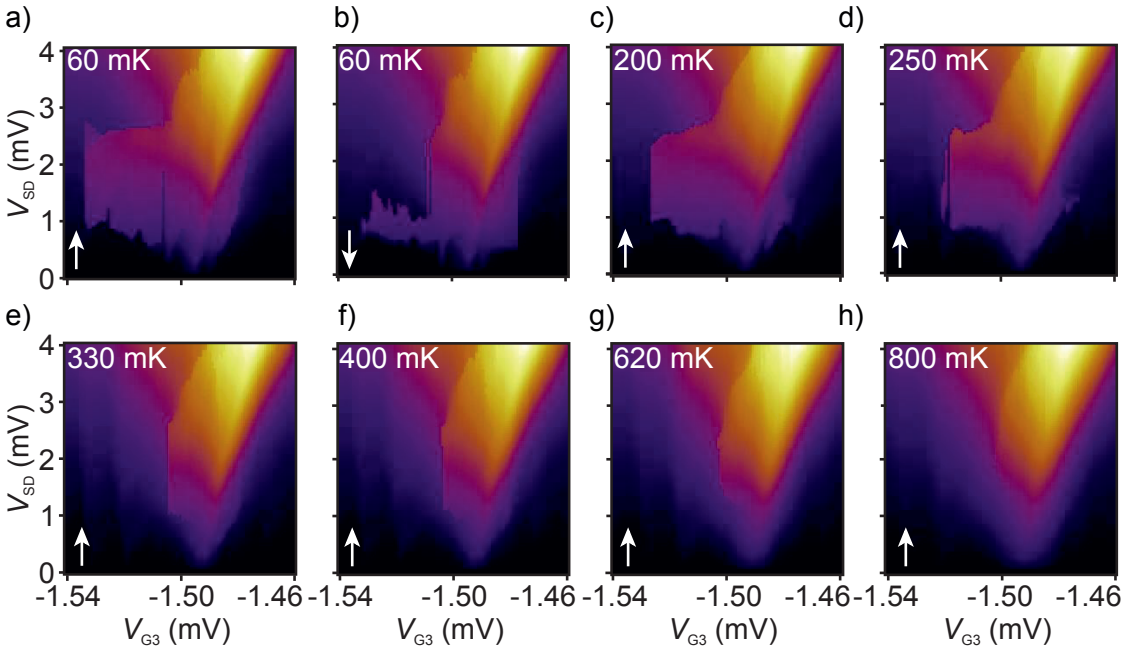


Figure 5.12: Measurements of self-oscillations in a Coulomb diamond for different temperatures. The leftmost panel was measured at base temperature, 60 mK, with two different voltage bias sweep directions indicated by white arrows. They reveal an area of self-oscillations and another of bistability showing self-oscillations in one of the sweep directions. In the other panels, the Coulomb diamond is always measured with the same bias sweep direction but with increasing temperatures, up to 820 mK. The self-oscillation area progressively vanishes as the temperature increases.

5.11 Conclusion

In conclusion, we were able to construct stability diagrams that fully characterize the oscillations induced by electron tunneling in single and double quantum dot configurations. We achieve this by observing hysteresis cycles in the current flowing through the device, by using a novel protocol to probe, pump and kill these self-oscillations, and by developing a dynamical model. Our results show the subtleties in the coupling between mechanical motion and single electron transport, and open new venues to design autonomous motors and other types of energy transducers at the microscale.

6

Non-linear dynamics of an electromechanical resonator

Contents

6.1 Introduction 67
6.2 Device characterisation 68
6.3 Theoretical model 70
6.4 Steady state response and electronic tunnelling 71
6.5 Results 74
6.6 Conclusion 76

6.1 Introduction

In previous chapters, we focused on the coupling of the mechanical motion of CNTs with single electron tunneling. We noted that this coupling is in the ultrastrong regime, enabling spontaneous self-oscillations to emerge even in the absence of an external driving force. In these CNTs, various factors such as electrostatic forces, geometric properties, and contact forces can induce non-linear effects [116]. These effects are typically modeled as a Duffing non-linearity in the equation of motion for the mechanical resonator. However, the operating regime of the device, as discussed in earlier chapters, was limited to small amplitudes and driving forces, ensuring

that non-linearities did not play a significant role.

In this chapter, we present electron transport measurements of a CNT under strong driving. We also introduce a theoretical model shedding light on the roles of Duffing non-linearities and electromechanical coupling extending beyond the linear limit.

Duffing's equation has been widely explored to understand limit cycles and chaotic motion [117]. Our findings provide a foundation for exploring such mechanisms in nanomechanical resonators, where quantum effects might significantly influence the system's dynamics. Furthermore, our results could pave the way for studying thermodynamic models based on limit cycles, similar to those observed in neurons and clocks [118, 119].

6.2 Device characterisation

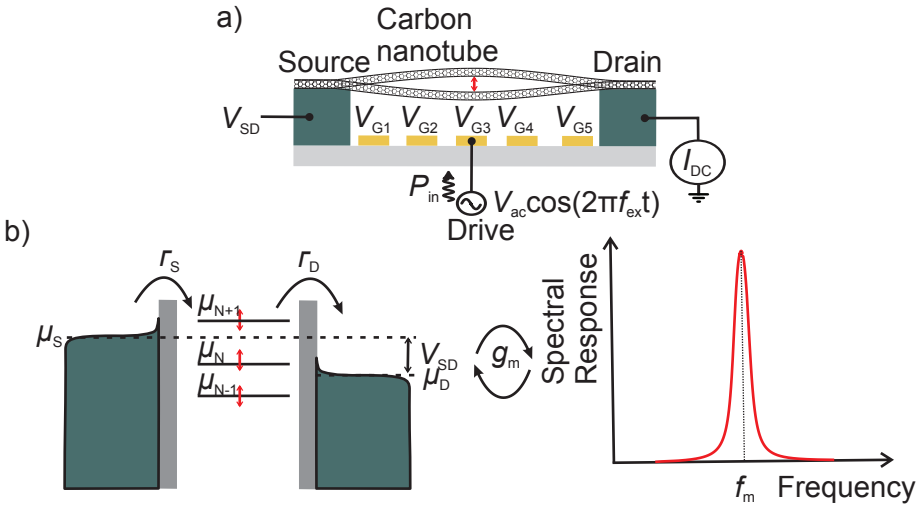


Figure 6.1: **a)** A CNT nanoelectromechanical resonator suspended over two metal electrodes. Five finger gates are used to control the electrostatic potential. An rf drive $V_{\mathrm{ac}}\cos(2\pi f_{\mathrm{ex}}t)$ is used to excite the mechanical motion. **(b)** The energy space representation of the hybrid system. The quantum dot can host several charge states with corresponding chemical potentials $\mu_{\mathrm{N\text{-}1}}$, μ_{N}, and $\mu_{\mathrm{N+1}}$ that are coupled to the mechanical motion of the CNT with a strength g_{m}.

We use an electromechanical resonator formed by suspending a CNT over source-drain metal electrodes (see Figure 6.1a), as used in the preceding chapters. A bias voltage V_{SD} is applied, and a current I_{DC} through the CNT is measured. Five gate

electrodes with voltages V_{G1} to V_{G5} are used to control the electrostatic potential and form a quantum dot. An rf drive is connected to one of the gates, which can be used to excite the mechanical motion of the CNT, detected by monitoring I_{DC}. In contrast to previous chapters, where just one energy level of the quantum dot played a role, multiple energy levels of the quantum dot play a role here due to the large displacement of the mechanical oscillator under strong driving and ultrastrong coupling. We consider different levels $\mu_{N\text{-}1}, \mu_N, \mu_{N+1}$ in the quantum dot, coupled to source and drain, represented by chemical potentials μ_S and μ_D, with tunneling rates Γ_S and Γ_D respectively (see Figure 6.1b). The energy levels in the dot are also coupled to the mechanical motion of the CNT, having a natural resonance frequency f_m, with a coupling strength g_m. The back action due to this coupling strongly influences the state of both mechanical motion and quantum dot state, as described in previous chapters.

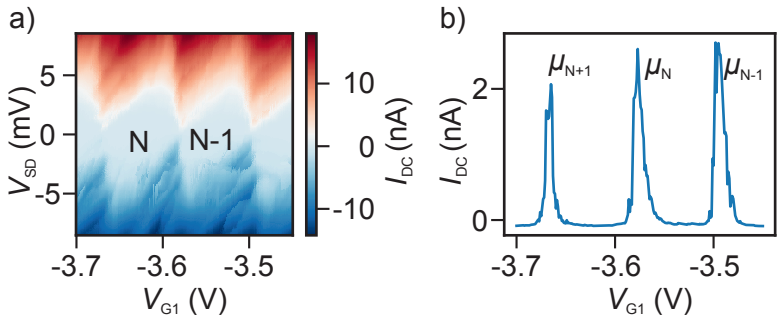


Figure 6.2: **(a)** A colormap of I_{DC} as a function of V_{SD} and V_{G1}. Characteristic Coulomb diamonds are observed, showing different charge states. **b)** I_{DC} as a function of V_{G1} for a constant $V_{SD} = 0.25\,\text{mV}$ showing Coulomb peaks. Each Coulomb peak corresponds to a specific chemical potential entering the bias window.

We first start by characterising the electronic degree of freedom, i.e., the quantum dot in the CNT. The gate voltages are configured such that a single quantum dot is defined in the CNT. In Figure 6.2a, the chemical potential ladder is varied using V_{G1} while changing V_{SD}. Coulomb diamonds are observed, which evidence single electron transport through the CNT. Each Coulomb diamond corresponds to a fixed number of charges on the quantum dot. At a fixed $V_{SD} = 0.25\,\text{mV}$ in Figure 6.2b, Coulomb peaks are observed, corresponding to a chemical potential entering the bias window.

Before introducing the main experimental results of this chapter, we will introduce the theoretical model and the non-linear terms that play a role in the dynamics of the mechanical oscillator. These non-linear effects are particularly important as we go beyond the limit of small oscillations.

6.3 Theoretical model

The system consists of a single quantum dot coupled to the mechanical oscillator. The total Hamiltonian of the system can be written as

$$H = H_{\text{mech}} + H_{\text{QD}} + V_{\text{int}}. \tag{6.1}$$

The first term describes the mechanical oscillator with a Duffing non-linearity. This term also contains the external force applied to the mechanical oscillator, such that

$$H_{\text{CNT}} = \hbar\omega_0 \hat{b}^\dagger \hat{b} + \frac{\beta}{4}\hat{z}^4 + F\cos(2\pi f_m t)\hat{z}. \tag{6.2}$$

The operators $\hat{b}$ ($\hat{b}^\dagger$) are the annihilation (creation) operators of the mechanics related to the displacement operator $\hat{z}$, ω_0 is the natural frequency of the CNT, β is the Duffing parameter, and F is the external force (per unit mass) applied to the CNT.

The second term in Equation (6.1) describes the single energy level of a quantum dot,

$$H_{\text{QD}} = \mu\hat{n}. \tag{6.3}$$

The energy required to add an electron from the source/drain to the dot is given by the chemical potential μ. The occupation of the dot is described by the number operator $\hat{n}$ which can take the value of either 0 or 1 depending if the dot is empty or occupied. The electrons can tunnel to/from the quantum dot with source (drain) tunneling rates $\gamma^{\text{in}}_{\text{S/D}}(\mu)$ which are defined as

$$\gamma^{\text{in}}_{\text{S/D}}(\mu) = \Gamma_{\text{S/D}}\rho_{\text{S/D}}(\mu), \tag{6.4}$$

$$\gamma^{\text{out}}_{\text{S/D}}(\mu) = \Gamma_{\text{S/D}}\left(1 - \rho_{\text{S/D}}(\mu)\right), \tag{6.5}$$

where $\Gamma_{S/D}$ are the source/drain tunnel barriers. The fermionic population of each reservoir is given by the density of states ρ that depends on their respective chemical potentials μ_k, $k = \mathrm{S, D}$. The device used in this study is in the lifetime broadening regime, i.e. $\hbar\Gamma_{\mathrm{tot}} >> k_B T$. We therefore suppose the source and drain contacts to be at zero temperature.

The interaction between the mechanics and the electronic degree of freedom in Equation (6.1), following Ref. [120], is given by

$$V_{\mathrm{int}} = \hbar g_{\mathrm{m}} \frac{\hat{z}}{z_{\mathrm{ZPM}}} \hat{n}, \tag{6.6}$$

where g_{m} is the electromechanical coupling constant, $z_{\mathrm{ZPM}} = \sqrt{\hbar/2m\omega_{\mathrm{m}}}$ is the zero-point motion and m is the mass of the CNT.

Note that the force arising due to the electromechanical coupling $F_{\mathrm{CNT}} = -\partial V_{\mathrm{int}}/\partial z$ is always negative. Therefore, when the dot is occupied ($\hat{n} = 1$), the CNT experiences a restoring force proportional to the coupling strength.

We start by simulating the response of the mechanical oscillator for different driving powers. Figure 6.3a shows the Duffing response and the bistability for different sweep directions. Figure 6.3b shows the steady-state displacement for different driving force amplitudes as a function of driving frequency $\omega_{\mathrm{ex}} = 2\pi f_{\mathrm{ex}}/\omega_{\mathrm{m}}$. In the case of low driving force, the amplitude response of the mechanical oscillator is that of a harmonic driven oscillator. As the driving force is increased, a change in the response is observed due to the Duffing non-linearity resulting in the hardening of the mechanical oscillator, i.e., higher amplitudes with increasing frequency.

6.4 Steady state response and electronic tunnelling

We study the steady-state response of the CNT displacement with the electronic back action in the weak and strong driving regimes. Since the electron transport is much faster than the mechanical motion, we use the adiabatic approximation: the moments are instantaneous, and the dot's population instantaneously reaches the steady state, i.e., $\langle\hat{z}\rangle = z$ and $\langle\hat{n}\rangle = p(\mu)$, where $p(\mu)$ is the population of the dot given by

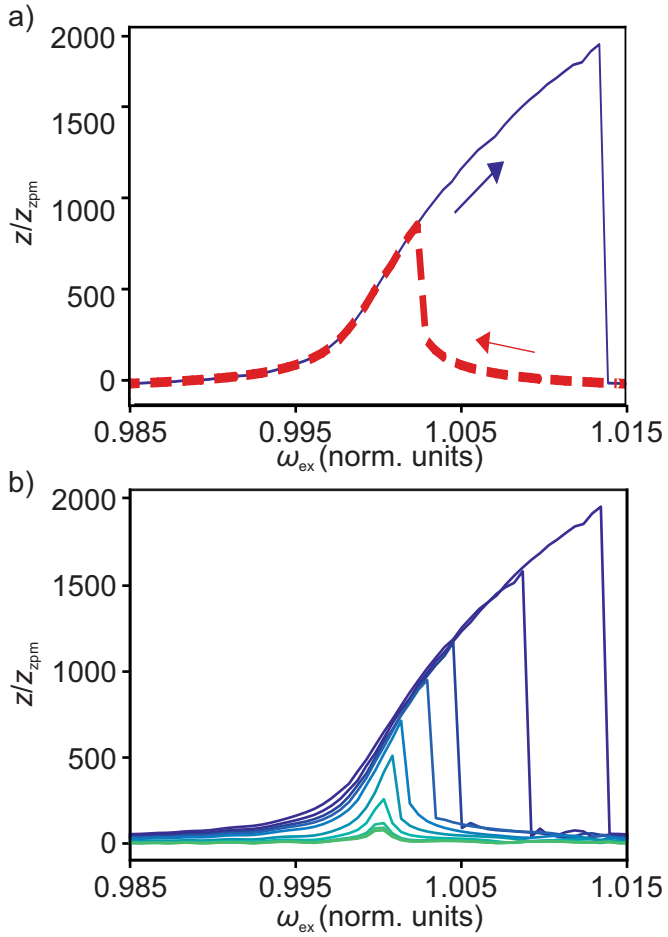


Figure 6.3: a) The characteristic response of a Duffing oscillator exhibits bistability in its motion, which depends on the sweep direction.**(b)** The simulated steady-state response of the CNT z relative to its zero-point motion z_{zpm} is shown as a function of the renormalized driving frequency $\omega_{\mathrm{ex}} = 2\pi f_{\mathrm{ex}}/\omega_m$. This frequency varies from low to high values for different driving forces. The transition from darker to lighter colors represents the force values F being: $F_0/2.5$, $F_0/3$, $F_0/3.5$, $F_0/4$, $F_0/5$, $F_0/10$, $F_0/20$, $F_0/40$, $F_0/50$, and $F_0/60$, with $F_0 = 4$. The back action of the electronic transport is not considered here.

$$p(\mu) = \frac{\Gamma_{\mathrm{S}}^{\mathrm{in}}(\mu) + \Gamma_{\mathrm{D}}^{\mathrm{in}}(\mu)}{\Gamma_{\mathrm{tot}}}. \tag{6.7}$$

Since p is a function of the electrochemical potential, which in turn is a function of the displacement of the CNT, it is time dependent and can take values between 0 and 1. When the electrochemical potential is within the bias window, i.e., $\mu_{\mathrm{D}} < \mu_N < \mu_{\mathrm{S}}$, single-electron transport occurs and is measured as a current I_{DC} given by

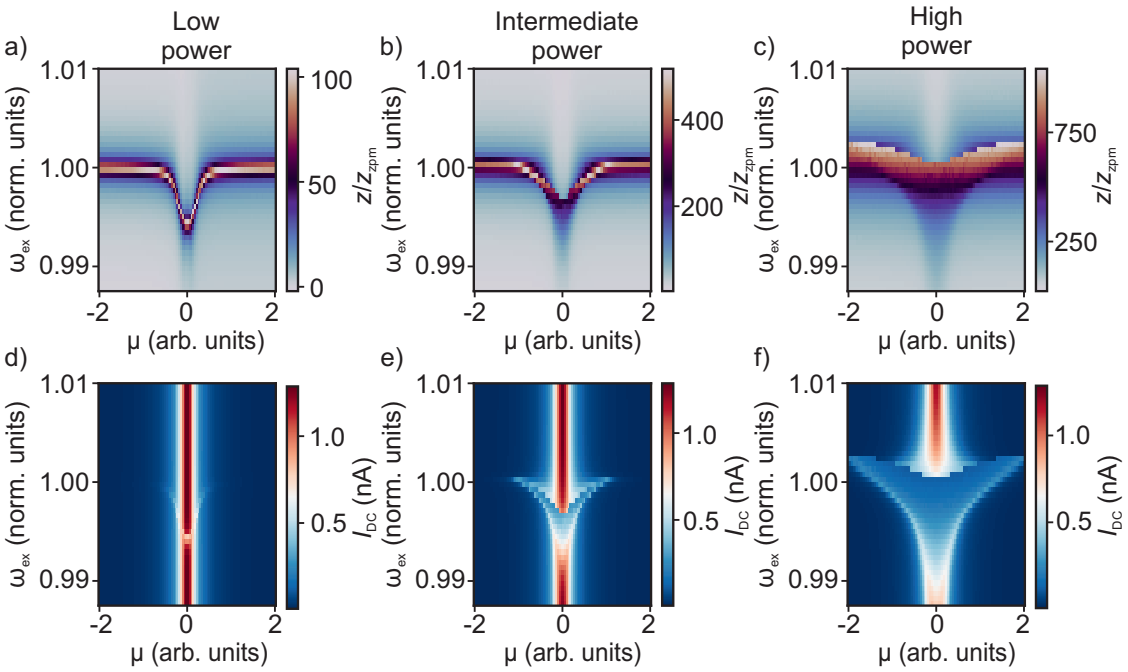


Figure 6.4: The top row **(a-c)** corresponds to the simulated steady-state displacement of the CNT z with respect to its zero-point-motion z_{zpm}, as a function of normalized frequency ω_{ex} and quantum dot's energy level μ, for different driving powers. The bottom row **(d-f)** corresponds to the simulated current through the device I_{DC}, as a function of normalized frequency ω_{ex} and quantum dot's energy level μ, for respective driving powers. Parameters, based on experimental data, are $\mu_{\mathrm{R}} = -0.1$ eV, $\mu_{\mathrm{L}} = 0.1$ eV, $\Gamma_{\mathrm{L}}/2\pi = \Gamma_{\mathrm{R}}/2\pi = 30$ GHz, $g_m/2\pi = 0.5$ GHz, $\beta = 9.375 \times 10^{-9}$, and damping $\nu = 1.15 \times 10^{-3}$.

$$I_{\mathrm{DC}} = e\frac{\Gamma_{\mathrm{S}}^{\mathrm{in}}(\mu)\Gamma_{\mathrm{D}}^{\mathrm{out}}(\mu) - \Gamma_{\mathrm{D}}^{\mathrm{in}}(\mu)\Gamma_{\mathrm{S}}^{\mathrm{out}}(\mu)}{\Gamma_{\mathrm{tot}}}. \tag{6.8}$$

We use Equation (6.1) to simulate the displacement of the CNT as a function of driving frequency, see Figure 6.4 (top row) for three different force amplitudes corresponding to the weak, intermediate, and strong driving regimes. In Figure 6.4 (bottom row), the corresponding I_{DC} through the CNT is shown. In the weak driving regime (see Figure 6.4(a,d)), the CNT behaves as a driven harmonic oscillator. It should be noted that electron transport μ occurs whenever the energy level is in the bias window. The mechanical motion can cause the energy level μ to move within this bias window for a certain period in every cycle, causing a net change in I_{DC}. Consequently, it can be observed that close to the Coulomb peak, the frequency of the mechanical oscillator changes (softening of the mechanical frequency) due

to the electromechanical coupling, as discussed in Chapter 4.

Increasing the strength of the driving force in Figure 6.4(b,e), the softening of the mechanical frequency close to the Coulomb peak can still be observed. However, it should be noted that the lineshape of the mechanical resonance shows a Duffing response. This arises due to the non-linearity given by the interaction between the electron and mechanical coupling [57]. It should be noted that the resonance peak obtained by measuring I_{DC} is broadened due to the large displacement of the mechanical oscillator.

Finally, in Figure 6.4(c,f), we focus on the response of the hybrid electromechanical system when it is strongly driven. In this case, the Duffing nature of the mechanical oscillator dominates. It can be seen that the lineshape of the mechanical resonance broadens and higher amplitudes are observed at increasing frequencies, due to the hardening nature of the Duffing non-linearity.

6.5 Results

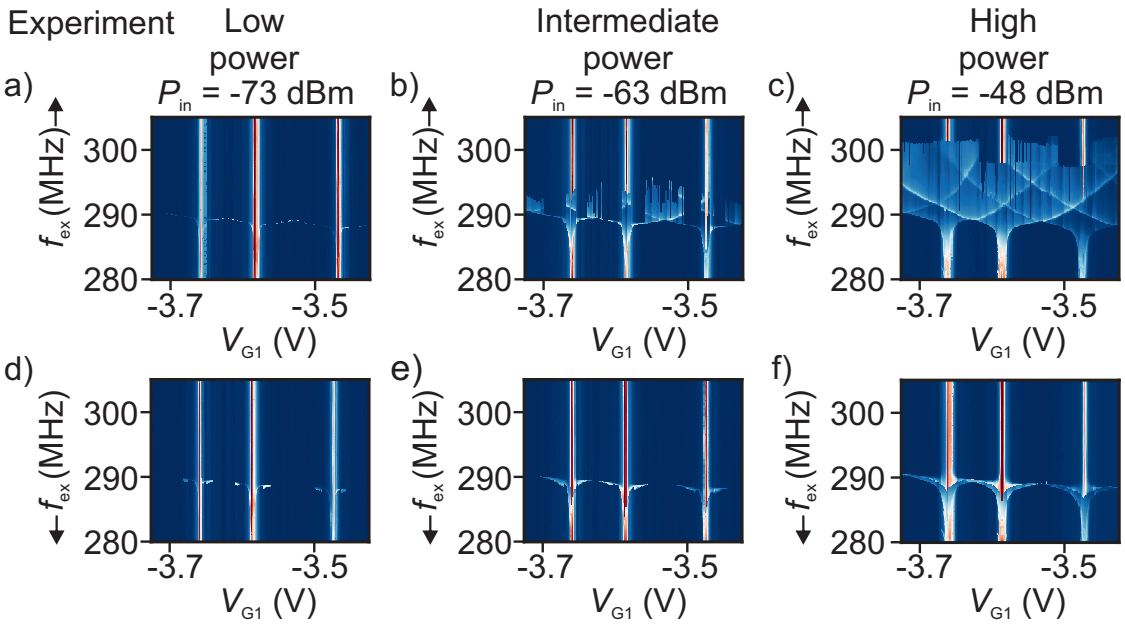


Figure 6.5: The measured I_{DC} response as a function of f_{ex} and V_{G1} across various driving powers is depicted. The top row **(a-c)** illustrates the sweep direction of f_{ex} from low to high, while the bottom row **(d-f)** illustrates the sweep direction of f_{ex} from high to low.

We now turn our attention to the experimental results in this section. Figure 6.5 shows the response of I_{DC} as a function of gate voltage V_{G1} and driving frequency f_{ex}, for different sweep directions (low to high frequency or vice versa) and driving power P_{in}. The top row corresponds to a sweep direction from low frequency (280 MHz) to high frequency (305 MHz), while the bottom row corresponds to a sweep direction from high frequency (305 MHz) to low frequency (280 MHz).

In the low driving force regime with $P_{\mathrm{in}} = -73$ dBm at the device (Figure 6.5(a,d))), there is no major difference when comparing to results of Chapter 4, i.e., the mechanical resonance softens at each of the Coulomb peaks corresponding to a different energy level μ_{N-1}, μ_N, and μ_{N+1} entering the bias window. It can also be seen that the mechanical frequency increases slightly with increasing gate voltage due to the electrostatic tensioning of the CNT.

As we increase the driving power to $P_{\mathrm{in}} = -63$ dBm corresponding to the intermediate driving force in Figure 6.5(b,e), several features develop. A bistability between the two sweep directions can be seen when comparing the response for the up sweep (Figure 6.5(b)) and for the down sweep (Figure 6.5(e)).

At the highest driving powers $P_{\mathrm{in}} = -48$ dBm in Figure 6.5(c,f), the response evolves into an arch-like structure. This is due to an intricate process, where the mechanical response arises due to the Duffing and electromechanical non-linearities. This in turn alters the I_{DC} which is a function of the displacement of the mechanical oscillator. Under strong driving, the displacement can be large, leading to various energy levels of the quantum dot participating in the electron transport.

We can explain the observed response of I_{DC} using the model presented in Section 6.3. As the driving power, and consequently the driving force, increases, the Duffing term in Equation (6.2) begins to dominate. This dominance results in the broadening of the mechanical resonance. Due to its hardening nature, higher amplitudes are achieved at higher frequencies. This effect brings multiple energy levels μ_{N-1}, μ_N, and μ_{N+1} within the bias window in a single period of oscillation. At different amplitudes, various levels enter the bias window, creating an arch-like structure that can be traced back to each Coulomb peak. We also note that the

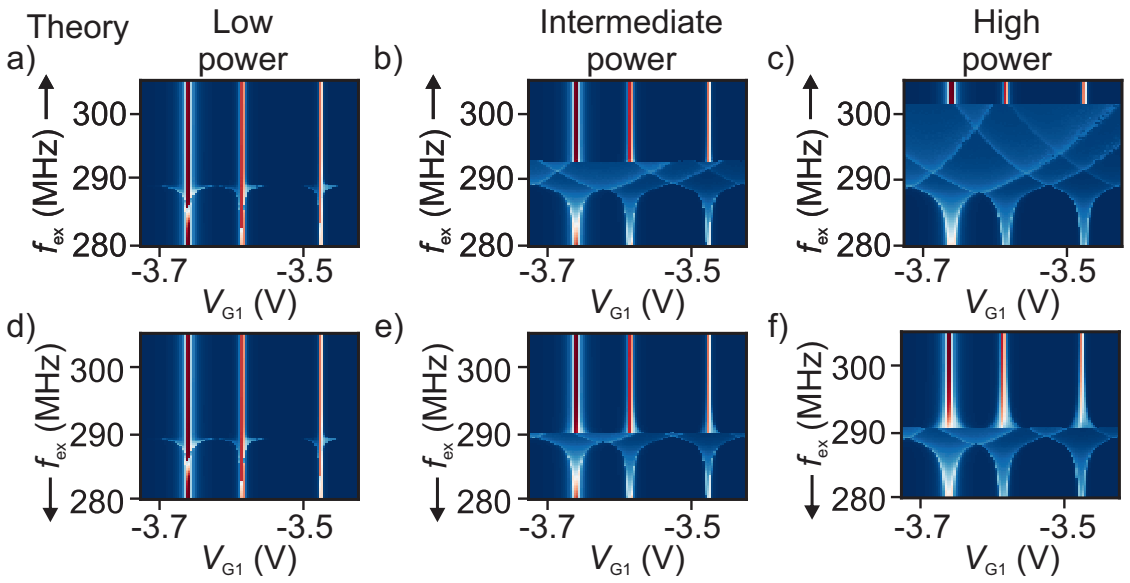


Figure 6.6: The calculated I_{DC} response as a function of f_{ex} and V_{G1} for various driving powers is presented. The top row **(a-c)** corresponds to the sweep direction of f_{ex} from low to high, while the bottom row **(d-f)** corresponds to the sweep direction of f_{ex} from high to low.

model can calculate the I_{DC} response, as shown in Figure 6.6. This calculation is achieved by extending the model to include multiple μ, leading to the equation

$$p_{\text{eff}}(x) = \sum_i \frac{g_{\text{m}}^i}{\omega_{\text{m}}} p(\mu_i), \tag{6.9}$$

where p_{eff} represents the population of the dot in the adiabatic regime, as given by Equation (6.7). The electromechanical coupling strength for each level is denoted by g_{m}^i. Similarly to Figure 6.5, the top row corresponds to the low-to-high sweep of f_{ex}, while the bottom row corresponds to the high-to-low sweep of f_{ex}. The curvature of the arches is due to a combination of Duffing non-linearity and electromechanical coupling. The calculated response matches well with the experimental data, although it is notable that the theoretical data lacks experimental noise.

6.6 Conclusion

In this chapter, we have highlighted the effect of non-linearities on the electrical response of the CNT. We found that in the weak driving regime, the mechanical oscillator experiences back-action due to single-electron tunneling (Chapter 4) while experiencing electrostatic tensioning due to the gate voltage.

In the strong driving force regime, it was found that non-linearities play a significant role and produce arch-like structures owing to the transduction of the mechanical motion to the electrical current. This system highlights a novel opportunity, with the non-linearities associated with the single-electron tunneling merging with the intrinsic Duffing non-linearities of the CNT. The model developed in this chapter is fully able to capture these interactions with simulations matching the experimental results.

Hybrid nanoelectromechanical systems in this regime provide an opportunity to explore limit cycles and chaotic motion with quantum tunneling noise [117]. Furthermore, such systems can provide a pathway to study quantum to classical transitions [121].

7

Measuring work and energy exchanges in a nanoscale electromechanical resonator

Contents

7.1 Introduction 80
7.2 Experiment 80
7.2.1 Transduction of displacement 83
7.2.2 Protocol 85
7.3 Electromechanical Model 86
7.3.1 Equation of motion 86
7.3.2 Effective mechanical frequency 89
7.3.3 Numerical simulations of the driven mechanical motion 90
7.4 Thermodynamics of the system 91
7.4.1 Thermodynamic quantities 91
7.4.2 Landauer interpretation 92
7.5 Erasure with two fermion baths 94
7.5.1 Average cyclic work cost of bit reset 95
7.5.2 Work is related to the spread of the occupation distribution 96
7.5.3 Erasure with two Fermion baths 97
7.5.4 Bounding the work cost of erasure 99
7.5.5 Bounds on the mean absolute deviation 101
7.6 Quantifying energy dissipation 104
7.7 Conclusion & Outlook 106

7.1 Introduction

In the past chapters, we have established the experimental setup and theoretical models to understand the coupling between the electrical and mechanical degrees of freedom in CNTs. A quantum dot coupled to a mechanical oscillator can be seen as analogous to a working fluid coupled to a piston, a quintessential example for understanding the laws of thermodynamics.

Several experiments using single-electron transistors have been carried out, demonstrating Szilard's engine and fluctuation-dissipation relationships [122, 123]. The mechanical oscillator in the present device presents an exciting control mechanism; it can be used to change the population of the quantum dot. Therefore, as bound by thermodynamics, it is required to dissipate heat.

In this chapter, we present how this nanoelectromechanical resonator can be used to demonstrate information erasure. This is a significant endeavor, as it involves converting electrical signals from a solid-state device at cryogenic temperatures into relevant thermodynamic quantities and analyzing them within the framework of thermodynamics. As will be discussed later, several challenges are faced from a theoretical standpoint, such as the presence of non-equilibrium conditions. This chapter is divided into three main parts: (I) the experimental techniques, (II) the conversion of experimentally measured quantities to thermodynamic quantities, and (III) the theory of Landauer's principle for fermionic baths.

7.2 Experiment

A nanoelectromechanical resonator is formed by suspending a CNT over source and drain metal electrodes, as used in previous chapters. The electrostatic potential of the CNT is controlled using five gate electrodes with voltages: V_{G1} to V_{G5}. The current through the CNT, I_{DC}, is measured while applying a source-drain bias voltage V_{SD}. An rf drive is connected to the middle gate to excite the mechanical motion of the CNT, and the motion can be monitored using an rf tank circuit. The full experimental setup is shown in Figure 7.1. In contrast to earlier chapters, where

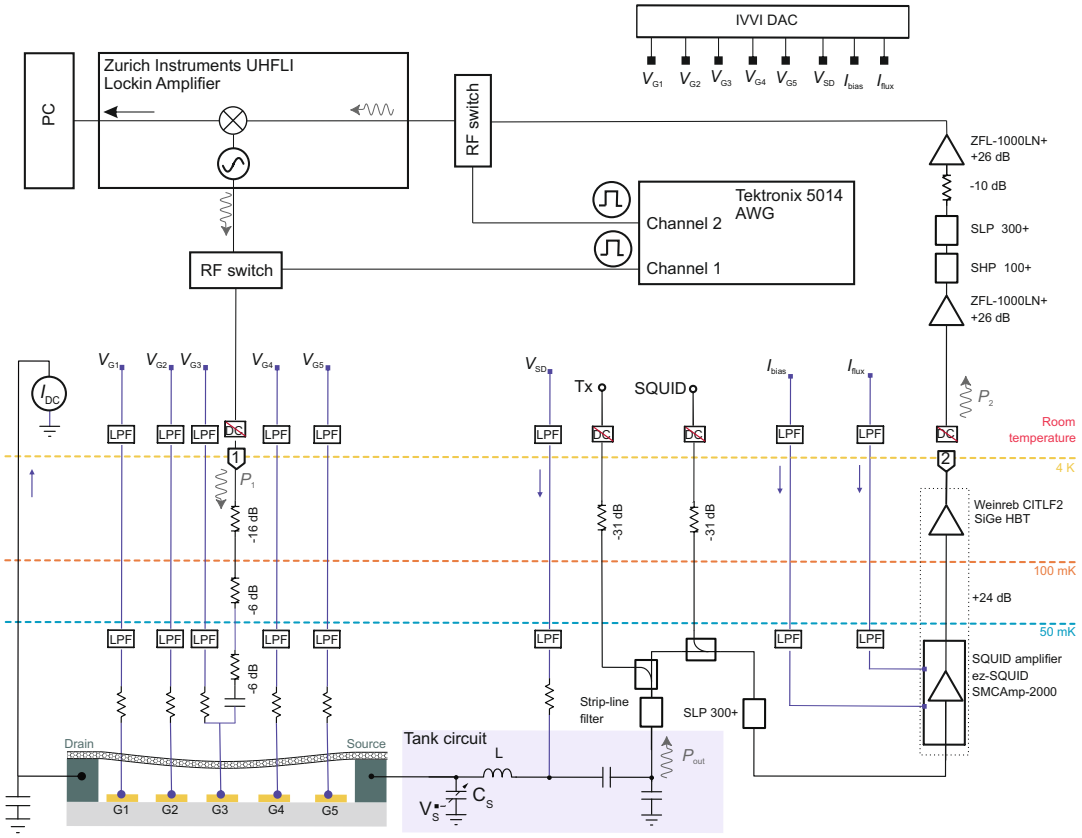


Figure 7.1: The experimental setup features a CNT device anchored at 50 mK. A cavity, composed of a surface-mount inductor and parasitic capacitance, is connected to the device's source to enable probing of the mechanical motion. A SQUID amplifier, maintained at 50 mK, is followed by a HEMT amplifier at the 4 K stage. Various DC and fast lines are connected to the device, as illustrated in the figure.

only electron transport measurements were accessible, here an electrical cavity is connected to one of the electrodes of the CNT. This connection allows probing the motion, wherein the electrical signal generated due to the mechanical motion is amplified by a series of amplifiers: a SQUID amplifier (see Chapter 3), a HEMT amplifier, and a room temperature amplifier. Finally, the amplified signal at room temperature is connected to a lock-in amplifier and measured using homodyne detection. The data is then collected by a PC as a digital record.

The energy space representation of the device is shown in Figure 7.2(b). The source and drain electrodes act as Fermi reservoirs with chemical potentials μ_S and μ_D, with their difference controlled experimentally using V_{SD}. The single electron energy level μ is strongly coupled to the two electrodes with tunneling

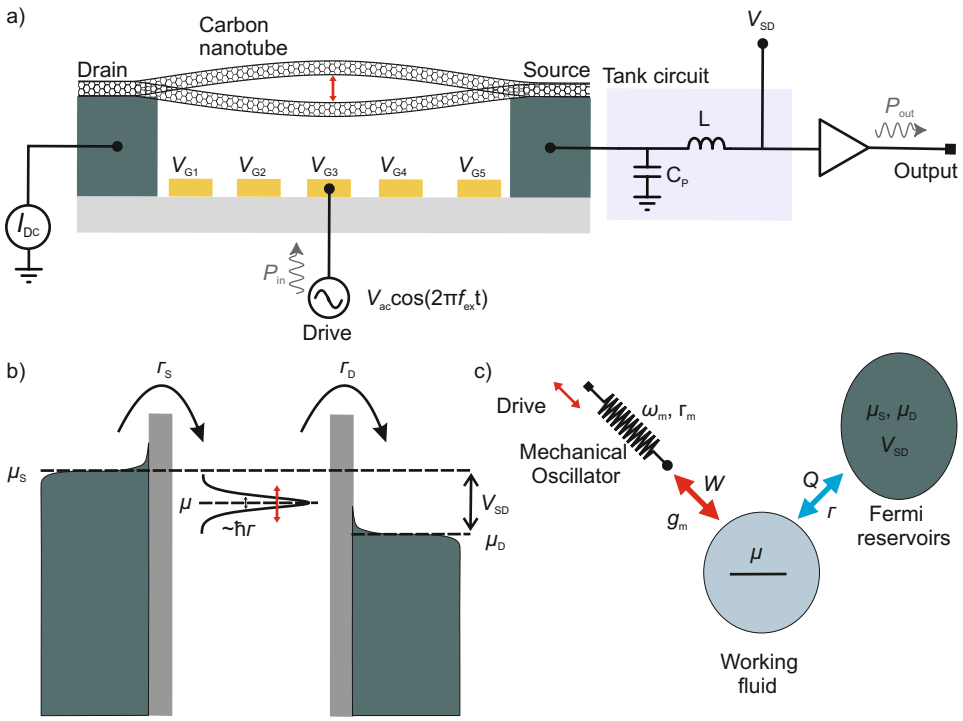


Figure 7.2: a) A CNT device suspended over two metal electrodes. An electrical cavity is connected to one of the contacts, and the electrical signal P_{out} is measured, as illustrated in Figure 7.1. **b)** Energy-space representation of the device. Due to strong coupling to the reservoirs, the energy level experiences lifetime broadening. **c)** The thermodynamic quantities involved in this system. The quantum dot energy level is the working fluid, where the mechanical oscillator can either perform or extract work W, and heat Q is exchanged with the Fermi reservoirs.

rates Γ_{S} and Γ_{D}. In this regime ($\hbar\Gamma \gg k_{\text{B}}T$), the energy level experiences lifetime broadening, where T is the temperature of the system, and quantum tunneling noise dominates over thermal noise.

This system can be viewed as an equivalent of a nanomechanical piston and working fluid (see Figure 7.2(c)). The single energy level acts as a working fluid such that the mechanical motion of the CNT performs work W on the system while the Fermi reservoirs can exchange heat Q. Due to a finite V_{SD} and lifetime broadening in this system, this device operates away from equilibrium with no thermal reservoirs. This setup could allow the study of nanoscale devices subject to non-equilibrium conditions.

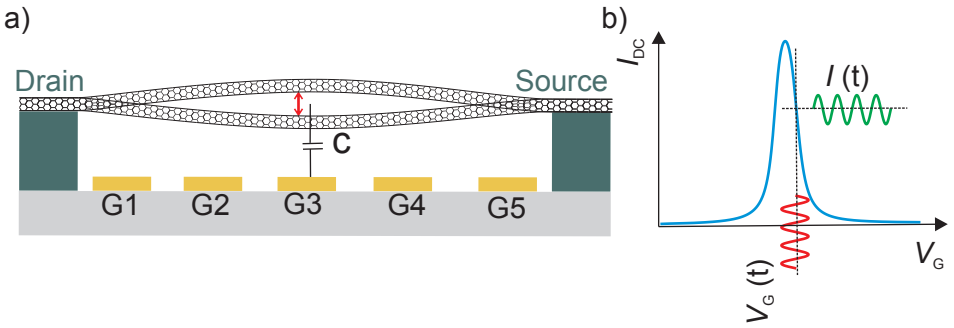


Figure 7.3: **a)** When the CNT moves due to mechanical motion, the capacitance between the CNT and the gate electrode changes. This alteration causes the electrostatic potential experienced by the quantum dot to vary. **b)** For small enough oscillations, i.e., when the displacement is much smaller than the distance between the gate electrodes and the CNT, the effect of this change in capacitance can has the same effect as an oscillating gate voltage $V_{\mathrm{G}}(t)$. This oscillation generates a current $I(t)$ through the CNT with the same frequency as that of the mechanical oscillator.

7.2.1 Transduction of displacement

The mechanical motion results in a change of capacitance between the gate electrodes and the CNT. For small enough oscillations, this change in capacitance can be considered as an effective oscillating voltage, with the same frequency as that of the mechanical motion. The oscillating gate voltage modulates the quantum dot energy level, causing an oscillating current through the CNT.

We make the following assumptions for the transduction of mechanical motion into an electrical signal:

- The conductance is just a function of charge q on the CNT. Therefore, any instantaneous value of gate voltage V_{G} yields a specific instantaneous value of current, i.e., $q(t) \rightarrow V_{\mathrm{G}}(t) \rightarrow I(t)$.
- The electron transport is much faster than the mechanical motion. This is generally true for our device as $\Gamma_{\mathrm{S,D}} \gg \omega_{\mathrm{m}}$.

We can now find the conductance for any particular instance of time

$$G(q(t)) \approx G(q_0) + \frac{\partial G}{\partial q}\delta q(t). \tag{7.1}$$

We can approximate the instantaneous charge as

$$\delta q(t) \approx \left(\frac{dq}{dV_G}\right)_z \delta V_{\mathrm{G}}(t) + \left(\frac{\partial q}{\partial z}\right)_{V_{\mathrm{G}}} \delta z(t). \tag{7.2}$$

The first term corresponds to the change in charge due to electrostatic effects, while the second term corresponds to the mechanical oscillations. For small enough changes, the first term is neglected. Also,

$$q = c_{\mathrm{G}} V_{\mathrm{G}}^{\mathrm{DC}}, \tag{7.3}$$

and,

$$\delta q = c_{\mathrm{G}} \delta V_{\mathrm{G}}(t) + c'_{\mathrm{G}} V_{\mathrm{G}}^{\mathrm{DC}} \delta z(t), \tag{7.4}$$

where c_{G} is the associated gate capacitance.

Ignoring the first term, as it is the electrostatic contribution, and substituting this in equation (7.1)

$$\delta G(t) = \frac{\partial G}{\partial q} c'_{\mathrm{G}} V_{\mathrm{G}}^{\mathrm{DC}} \delta z(t), \tag{7.5}$$

$$\delta G(t) = \frac{\partial G}{\partial V_{\mathrm{G}}} V_{\mathrm{G}}^{\mathrm{DC}} \frac{c'_{\mathrm{G}}}{c_{\mathrm{G}}} \delta z(t), \tag{7.6}$$

$$\delta I(t) = V_{\mathrm{SD}} \delta G(t), \tag{7.7}$$

$$\delta I(t) = \frac{\partial G}{\partial V_{\mathrm{G}}} V_{\mathrm{G}}^{\mathrm{DC}} V_{\mathrm{SD}} \frac{c'_{\mathrm{G}}}{c_{\mathrm{G}}} \delta z(t). \tag{7.8}$$

We can estimate c'_{G} by assuming the CNT as a cylinder and the gates as an infinite plane, which yields

$$c'_{\mathrm{G}} = \frac{c_{\mathrm{G}}}{d \ln\left(\frac{2d}{r}\right)}, \tag{7.9}$$

where d is the separation between the gates and the CNT, and r is the radius of the CNT.

Finally,

$$V(t) = Z_{\mathrm{trans}} I(t). \tag{7.10}$$

This $V(t)$ is amplified through the amplifier chain having an impedance Z_{trans}, and it is demodulated, giving us the final measured voltage.

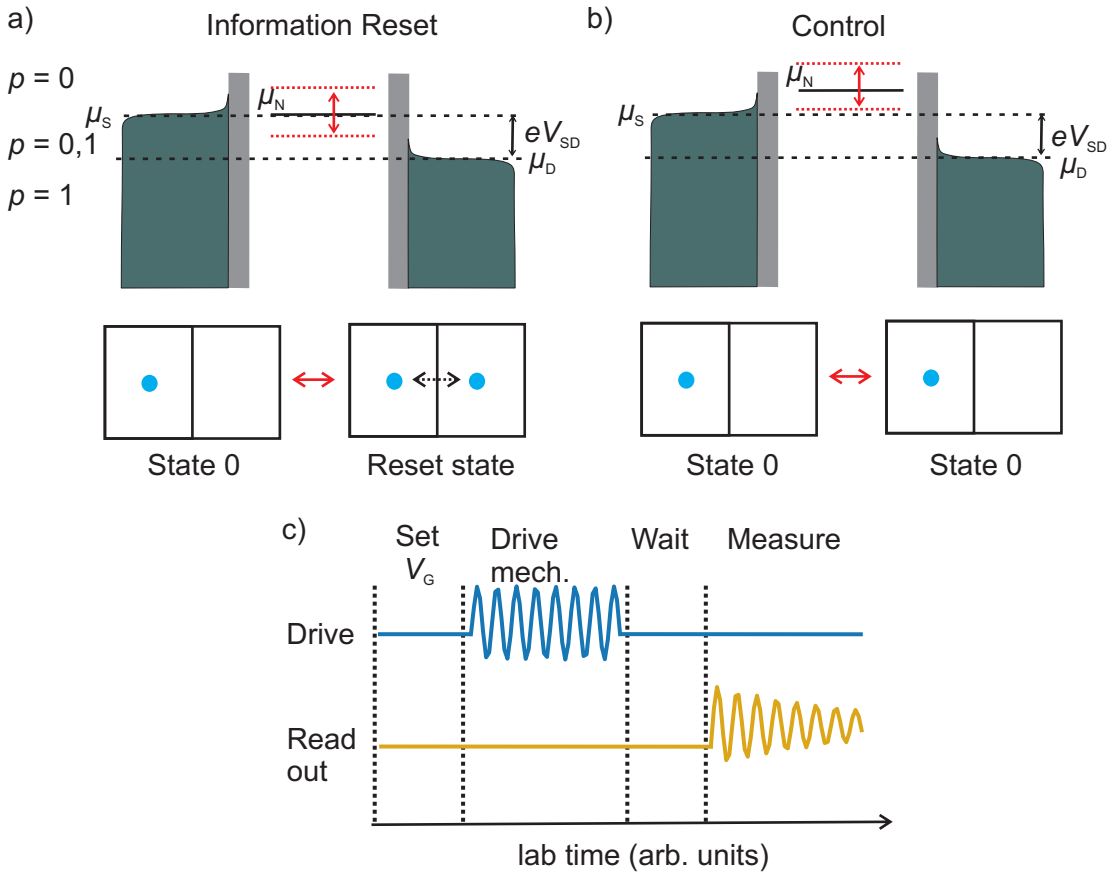


Figure 7.4: a) The occupation of the quantum dot can be controlled by changing the position of the energy level μ_N relative to the source and drain electrochemical potentials. In the case of the information reset of the protocol, the μ_N is placed such that the mechanical oscillations move the μ_N inside the bias window, effectively changing the quantum dot from State 0 to a reset state. **b)** A control protocol, during which no information is reset, can be implemented when the μ_N is significantly above the source and drain electrochemical potentials.**c)** The experimental protocol is implemented in four steps: setting the gate voltage, driving the mechanical oscillator, waiting for a predetermined period, and then measuring the electrical signal from the cavity.

7.2.2 Protocol

Using the gate voltages, the electrochemical potential can be controlled such that μ_N can be either empty (state 0) or full (state 1). Therefore, state 0 is achieved when $\mu_N > \mu_S, \mu_D$ and state 1 is achieved when $\mu_N < \mu_S, \mu_D$. However, within the bias window, where $\mu_D < \mu_N < \mu_S$, the quantum dot constantly transitions between State 0 and State 1 as electrons tunnel through. This can be regarded as a reset state in the context of information thermodynamics. As shown in Figure 7.4(a), μ_N can be positioned right at the edge of the bias window, and then the mechanical motion

can be used to shift μ_{N} within this bias window, effectively erasing information as an indeterminate state (0 or 1) is reset to state 0. In this scenario, the mechanical oscillator is required to dissipate heat.

Figure 7.4(b) illustrates a control experiment. Here, μ_{N} is set above the source and drain electrochemical potentials, ensuring that the mechanical motion does not alter the state of the system. In this case, the mechanical oscillator is not expected to dissipate any heat.

The experimental protocol, as depicted in Figure 7.4(c), is performed as follows: First, the gate voltage is so that the quantum dot is set to the desired initial state, followed by an rf burst driving the mechanical oscillator. A brief wait period is introduced to eliminate any transients, after which the decaying signal resulting from the damping of the mechanical motion is measured. This process allows for the probing of the displacement, frequency, and dissipation of the mechanical oscillator, which will be utilized in subsequent sections to estimate the relevant thermodynamic quantities.

7.3 Electromechanical Model

In this section we formulate a model to capture the dynamics of the device and estimate how the relevant thermdynamic quantities can be estimated from experimental data.

7.3.1 Equation of motion

We use the same approach as in Chapter 4, but for the gate and bias voltages considered in this experiment, we need to take into account both the energy dependence of the tunnel barriers and the change in the stiffness of the nanotube with gate voltage. First, due to the energy-dependent tunnel barriers, the quantum dot exchanges electrons with the lead $\nu = \mathrm{S}, \mathrm{D}$ at rates (in the lifetime broadened regime $\hbar\Gamma_{\mathrm{b}} \gg k_{\mathrm{B}}T$)

$$\gamma_{\nu}^{\mathrm{in}}(\mu) = \gamma_{\nu}(\mu)\rho_{\nu}(\mu), \quad \gamma_{\nu}^{\mathrm{out}}(\mu) = \gamma_{\nu}(\mu)\left(1 - \rho_{\nu}(\mu)\right). \tag{7.11}$$

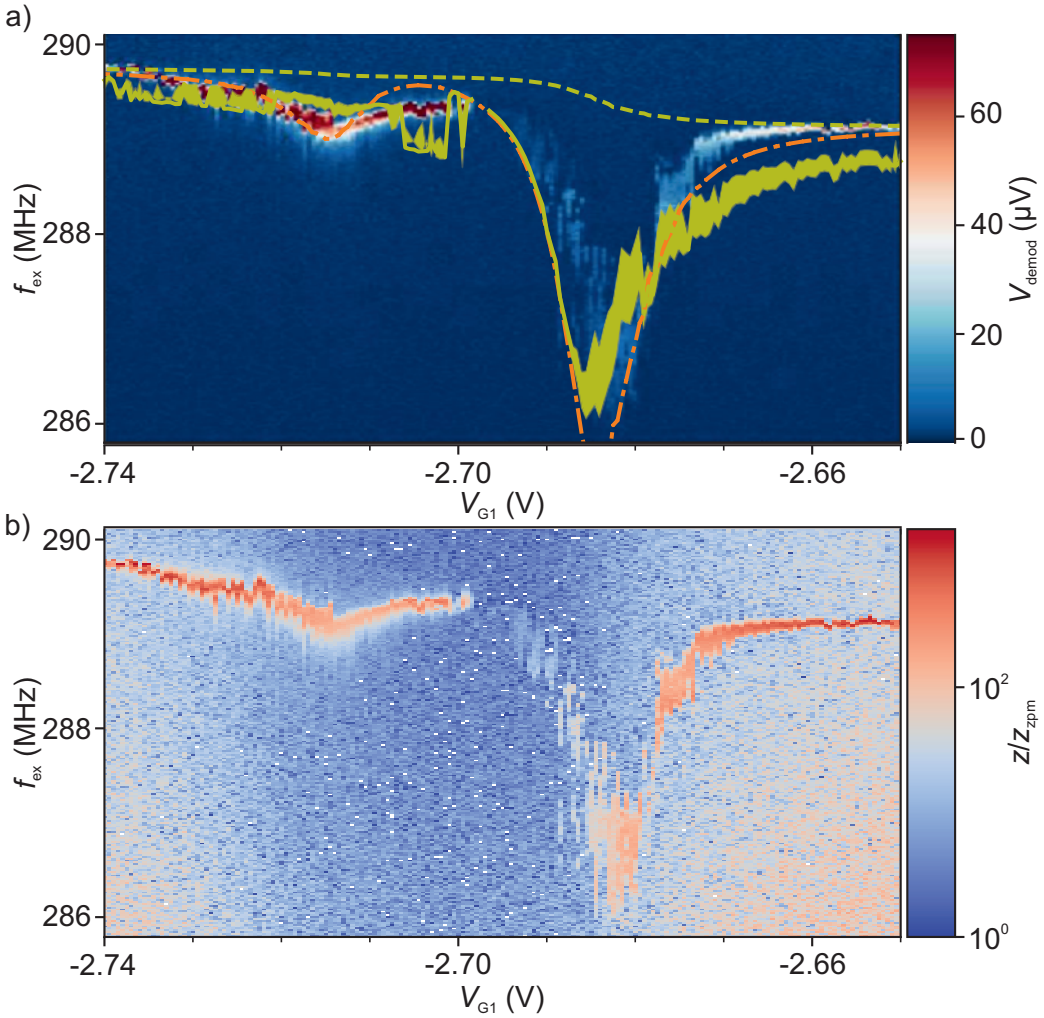


Figure 7.5: **a)** Measured demodulated voltage V_{demod} as a function of gate voltage and driving frequency. For each gate voltage, the maximum indicates the effective mechanical resonance frequency. **b)** Amplitude of the mechanical oscillations Δz calculated from V_{meas} as described in Section 7.2.1. The dashed yellow line in (a) corresponds to $\omega_{\mathrm{m}}(V_{\mathrm{G}})$ and the orange dash-dotted line to $\omega_{\mathrm{eff}}(V_{\mathrm{G}})$ in the small amplitude limit (Equation (7.19)). Finally, the solid yellow curve is the effective mechanical frequency computed by integrating the equation of motion for an amplitude Δz corresponding to the maximum amplitude in (b) for each gate voltage.

with [79]

$$\gamma_\nu(\mu) = \Gamma_\nu e^{b_\nu(\mu-\mu_\nu)}, \quad \rho_\nu(\mu) = \frac{1}{2} + \frac{1}{\pi}\arctan\left(\frac{2(\mu_\nu-\mu)}{\hbar\Gamma_{\mathrm{b}}}\right), \tag{7.12}$$

and $\Gamma_{\mathrm{b}} = \gamma_{\mathrm{S}} + \gamma_{\mathrm{D}}$. The values of the coefficients Γ_ν and b_ν are extracted from the experimental data by fitting the Coulomb peaks. The electrochemical potential of

the quantum dot depends on the mechanical displacement z as [93]

$$\mu(z) = \mu_0(V_\mathrm{G}) + \hbar\gamma_\mathrm{m}\frac{z}{z_\mathrm{pm}}, \tag{7.13}$$

where $\mu_0(V_\mathrm{G}) = \alpha(V_0 - V_\mathrm{G})$ is the electrochemical potential of the dot at $z = 0$, with α the lever arm and V_0 an offset on the gate voltage.

We consider the regime

$$\gamma_\mathrm{LR}(\mu) \gg \omega_\mathrm{m}, \gamma_\mathrm{m} \gg \Gamma_\mathrm{m}, \tag{7.14}$$

Therefore, we can use the adiabatic approximation and consider that, on the timescale of the mechanical evolution, the dot's population is always the equilibrium population,

$$p(z) = \frac{\gamma_\mathrm{S}^\mathrm{in}(\mu(z)) + \gamma_\mathrm{D}^\mathrm{in}(\mu(z))}{\gamma_\mathrm{t}(\mu(z))}, \tag{7.15}$$

with $\gamma_\mathrm{t} = \gamma_\mathrm{S} + \gamma_\mathrm{D}$. The evolution of the mechanics is thus given by

$$\ddot{z} + \Gamma_\mathrm{m}\dot{z} + \omega_\mathrm{m}(V_\mathrm{G})^2 z = -p(z)\gamma_\mathrm{m}\omega_\mathrm{m}(V_\mathrm{G})z_\mathrm{pm}. \tag{7.16}$$

$\omega_\mathrm{m}(V_\mathrm{G})$ is the mechanical resonance frequency when p is constant, accounting for the effects of the gate voltage on the overall stiffness of the nanotube. Furthermore, the change in ω_m with V_G is relatively small compared to the frequency softening due to the electromechanical coupling described in Chapter 4, therefore we can carry on with the same procedure, assuming that γ_m can be considered as constant within the range of the gate voltage sweep. Neglecting the mechanical damping when looking at only a few oscillations, the mechanical equation of motion reads

$$\ddot{z} + \omega_\mathrm{m}^2\left[z + 2p(\mu(z))\frac{\gamma_\mathrm{m}}{\omega_\mathrm{m}}z_\mathrm{ZPM}\right] = 0. \tag{7.17}$$

The change in ω_m with V_G is due to electrostatic effects and therefore $\omega_\mathrm{m}(V_\mathrm{G})$ depends on the average number of charges in the dot. Applying the linear model from Ref. [56] does not work so well here. This is because we are operating at large bias and thus cannot approximate the dot population with a single step in the middle of the bias window. We instead approximated $\omega_\mathrm{m}(V_\mathrm{G})$ as a linear

function of population, $\omega_{\mathrm{m}}(V_{\mathrm{G}}) = ap(\mu_0(V_{\mathrm{G}})) + b$, where p is the dot population, see Equation (7.15), at the electrochemical potential $\mu_0(V_{\mathrm{G}})$ (i.e., for $z = 0$). We obtain the coefficients a and b by fitting V_{demod} as a function of driving frequency f_{ex} and gate voltage V_{G1}, see yellow dashed line in Figure 7.5.

7.3.2 Effective mechanical frequency

Under the approximation of small displacements, the effective resonance frequency ω_{eff} can be estimated from Equation (7.17) by linearizing $p(\mu)$ around μ_0,

$$p(\mu) = p(\mu_0) + (\mu - \mu_0)\left.\frac{\partial p}{\partial \mu}\right|_{\mu_0}. \tag{7.18}$$

From Chapter 4, we obtain

$$\omega_{\mathrm{eff}}(V_{\mathrm{G}}) = \sqrt{\omega_{\mathrm{m}}(V_{\mathrm{G}})^2 + 2\gamma_{\mathrm{m}}^2 \hbar \omega_{\mathrm{m}}(V_{\mathrm{G}})\left.\frac{\partial p}{\partial \mu}\right|_{\mu_0(V_{\mathrm{G}})}}, \tag{7.19}$$

but the expression of $\left.\frac{\partial p}{\partial \mu}\right|_{\mu_0}$ is more complicated than in Chapter 4 due to energy dependence of the tunnel barriers,

$$\left.\frac{\partial p}{\partial \mu}\right|_{\mu} = \frac{1}{\gamma_{\mathrm{t}}}\left(\gamma_{\mathrm{D}}\left.\frac{\partial \rho_{\mathrm{D}}}{\partial \mu}\right|_{\mu} + \gamma_{\mathrm{S}}\left.\frac{\partial \rho_{\mathrm{S}}}{\partial \mu}\right|_{\mu}\right) + \frac{1}{\gamma_{\mathrm{t}}^2}(\rho_{\mathrm{D}} - \rho_{\mathrm{S}})\left(\gamma_{\mathrm{S}}\left.\frac{\partial \gamma_{\mathrm{D}}}{\partial \mu}\right|_{\mu} - \gamma_{\mathrm{D}}\left.\frac{\partial \gamma_{\mathrm{S}}}{\partial \mu}\right|_{\mu}\right), \tag{7.20}$$

with

$$\left.\frac{\partial \gamma_\nu}{\partial \mu}\right|_{\mu} = b_\nu \gamma_\nu, \quad \left.\frac{\partial \rho_\nu}{\partial \mu}\right|_{\mu} = \frac{-2}{\pi \hbar \Gamma_{\mathrm{b}}}\frac{1}{1 + \left(\frac{2(\mu_\nu - \mu)}{\hbar \Gamma_{\mathrm{b}}}\right)^2}. \tag{7.21}$$

$\omega_{\mathrm{eff}}(V_{\mathrm{G}})$ in the small amplitude limit is plotted in Figure 7.5(b) (dash-dotted pink line) using the tunnel rates obtained from fitting the Coulomb peak from Figure 7.5(a). We observe that the dip around μ_{D} is almost nonexistent, unlike in the data, suggesting that we have overestimated the asymmetry between γ_{D} and γ_{S}, while the dip around μ_{S} is deeper than the data, suggesting that the small amplitude limit does not fully apply in the experiment. This leads to a shallower and broader dip due to the large amplitude of the mechanical motion. We finally confirm that the experiment is beyond the small amplitude limit by numerically integrating the equation of motion Equation (7.17) for the amplitudes Δz corresponding to the maximum amplitude in Figure 7.5(b) for each gate voltage (solid yellow curve in Figure 7.5(a)).

7.3.3 Numerical simulations of the driven mechanical motion

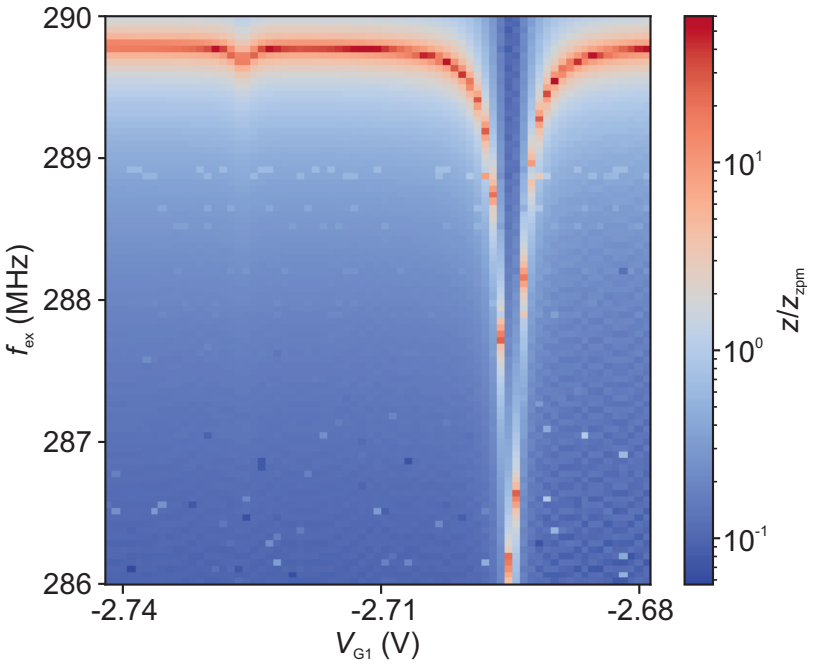


Figure 7.6: Steady-state amplitude, (z/z_{zpm}), of the driven CNT motion for different driving frequencies $f_{\mathrm{ex}} = \frac{\omega_{\mathrm{ex}}}{2\pi}$ and different chemical potentials μ_0 of the quantum dot (i.e., different gate voltages with $\Delta\mu_0 = -\alpha\Delta V_{\mathrm{G}}$).Parameters: $T = 20$ mK, $\frac{\omega_{\mathrm{m}}}{2\pi} = 289.5$ MHz, $m = 61$ ag, $Q_{\mathrm{m}} = 10^4$, $V_{\mathrm{SD}} = 2$ mV, $\frac{\gamma_{\mathrm{S}}}{2\pi} = 1$ GHz, $\frac{\gamma_{\mathrm{D}}}{2\pi} = 40$ GHz, $\frac{\gamma_{\mathrm{m}}}{2\pi} = 800$ MHz, and drive amplitude $A_{\mathrm{d}} = 30\omega_{\mathrm{m}}\Gamma_{\mathrm{m}}z_{\mathrm{zpm}}$ (i.e., we expect an amplitude $\Delta z = 60z_{\mathrm{zpm}}$ when driving at ω_{m} for a constant population).

We cannot solve the equation of motion Equation (7.16) analytically, so we integrate it numerically for different drive frequencies f_{ex}. The amplitude of the mechanical motion in the driven steady state is plotted in Figure 7.6. We clearly observe a softening of the mechanical frequency around the electrochemical potentials of both reservoirs. This softening corresponds to regions where the dot population p varies significantly with z. Additionally, we note that the amplitude reached for a similar driving strength is smaller in these regions, which corresponds to a decrease in the mechanical quality factor due to extra mechanical damping caused by electronic transport.

7.4 Thermodynamics of the system

7.4.1 Thermodynamic quantities

We define the basic thermodynamic quantities from our model of the dot and derive an expression of the Landauer principle. In this section, we approximate the dot evolution using the master equation

$$\dot{p} = \gamma^{\text{in}}(\mu(z))(1-p) - \gamma^{\text{out}}(\mu(z))p. \tag{7.22}$$

The population exchange with each of the source and drain electrodes is given by the probability currents

$$j_{\text{S,D}} = \gamma^{\text{in}}_{\text{S,D}}(\mu(z))(1-p) - \gamma^{\text{out}}_{\text{S,D}}(\mu(z))p, \tag{7.23}$$

such that $\dot{p} = j_{\text{S}} + j_{\text{D}}$.

The instantaneous average internal energy of the dot is given by

$$U(t) = \mu(z)p, \tag{7.24}$$

where

$$\mu(t) = \mu_0 + \hbar\gamma_{\text{m}}\frac{z(t)}{z_{\text{pm}}}. \tag{7.25}$$

Taking the time derivative, we obtain $\dot{U} = \dot{\mu}p + \mu\dot{p}$. The first part corresponds to the mechanical work,

$$\dot{W} = \dot{\mu}(t)p(t), \tag{7.26}$$

meanwhile, the second term must be rewritten as $\mu\dot{p} = (\mu - \mu_{\text{S}})j_{\text{S}} + (\mu - \mu_{\text{D}})j_{\text{D}} + \mu_{\text{S}}j_{\text{S}} + \mu_{\text{D}}j_{\text{D}}$. The chemical work done by the electrons is $\dot{W}_{\text{ch}} = \mu_{\text{S}}j_{\text{S}} + \mu_{\text{D}}j_{\text{D}}$. The heat exchange with each lead is

$$\beta\dot{Q}_\nu = \beta(\mu - \mu_\nu)j_\nu = -j_\nu \log\left(\frac{\gamma^{\text{in}}_\nu}{\gamma^{\text{out}}_\nu}\right), \tag{7.27}$$

with $\nu = \text{S, D}$. In this definition, we call $\gamma^{\text{in/out}} = \gamma^{\text{in/out}}_{\text{S}} + \gamma^{\text{in/out}}_{\text{D}}$ and the detailed balance property of the electron leads $\log(\gamma^{\text{in}}_\nu/\gamma^{\text{out}}_\nu) = -\beta(\mu - \mu_\nu)$. To recover the

second principle of thermodynamics, we consider the Shannon entropy of the dot $S = -p\log p - (1-p)\log(1-p)$ whose time derivative is

$$\dot{S} = -(j_{\rm S} + j_{\rm D}) \log\left(\frac{p}{1-p}\right). \tag{7.28}$$

Then, the total entropy production is

$$\dot{\Sigma} = \dot{S} - \beta\dot{Q} = -j_{\rm S}\log\left(\frac{p\gamma_{\rm S}^{\rm out}}{(1-p)\gamma_{\rm S}^{\rm in}}\right) - j_{\rm D}\log\left(\frac{p\gamma_{\rm D}^{\rm out}}{(1-p)\gamma_{\rm D}^{\rm in}}\right) \geq 0. \tag{7.29}$$

Their positivity comes from the definition of j_ν. $\dot{Q} = \dot{Q}_{\rm S} + \dot{Q}_{\rm D}$ is the total heat flow from the source to drain reservoir.

7.4.2 Landauer interpretation

We compute the work during the information reset in Figure 7.4, that is the first half of the mechanical period, starting at $t = 0$ at the minimum position (with $z(0) < 0$) and ending at the maximum position at $t = \frac{\pi}{\omega_{\rm eff}}$. In the adiabatic approximation:

$$W = \int_0^{\frac{\pi}{\omega_{\rm eff}}} {\rm d}t\, \dot{\mu}(t) p(\mu(z(t))) = \int_{\mu_i}^{\mu_f} {\rm d}\mu\, p(\mu) \tag{7.30}$$

with

$$\mu_i = \mu_0 + \hbar\gamma_{\rm m}\frac{z(0)}{z_{\rm pm}}, \quad \mu_f = \mu_0 + \hbar\gamma_{\rm m}\frac{z(\frac{\pi}{\omega_{\rm eff}})}{z_{\rm pm}} \tag{7.31}$$

where $z(0)$ is taken to be a minimum and $z(\frac{\pi}{\omega_{\rm eff}})$ a maximum of the displacement.

If we assume the initial and final values of the occupation $p(0) \sim \frac{1}{2}$ and $p(\frac{\pi}{\omega_{\rm eff}}) \sim 0$, the total Shannon entropy change is just $\Delta S = -\log 2$. The heat exchange is

$$\Delta Q = \Delta U - W - W_{\rm ch}. \tag{7.32}$$

As $U(t) = \mu(t)p$, we obtain $\Delta U = \frac{\mu_i}{2}$. In terms of the work, the second principle is

$$W + W_{\rm ch} \geq k_{\rm B}T\log 2 + \frac{\mu_i}{2}. \tag{7.33}$$

Now, we can introduce the adiabatic approximation to evaluate W.

Energy independent tunnel barriers and no broadening of the dot level

Here we neglect the tunnel barrier energy dependence and the width of the dot level. As above, we consider that the electrodes are at zero temperature:

$$\gamma_\nu^{\text{in}}(\mu) = \Gamma_\nu \Theta(\mu_\nu - \mu), \quad \gamma_\nu^{\text{out}}(\mu) = \Gamma_\nu \left(1 - \Theta(\mu_\nu - \mu)\right). \tag{7.34}$$

We compute the work during the information reset in Figure 7.4, that is the first half of the mechanical period, starting at $t = 0$ at the minimum position (with $z(0) < 0$) and ending at the maximum position at $t = \frac{\pi}{\omega_{\text{eff}}}$, in the adiabatic approximation, $W = \int_{\mu_i}^{\mu_f} \mathrm{d}\mu\, p(\mu)$.

In the case where $\mu_0 = \mu_{\text{S}}$ and a large enough bias is considered such that $\mu_i > \mu_{\text{D}}$, we have

$$p(\mu_i) = \frac{\gamma_{\text{S}}}{\Gamma_{\text{b}}}, \qquad p(\mu_f) = 0, \tag{7.35}$$

$$\gamma_{\text{S}}^{\text{in}}(\mu_i) = \gamma_{\text{S}}, \qquad \gamma_{\text{S}}^{\text{in}}(\mu_f) = 0. \tag{7.36}$$

Therefore,

$$W = \frac{\gamma_{\text{S}}}{\Gamma_{\text{b}}}(\mu_{\text{S}} - \mu_i) = \frac{\gamma_{\text{S}}}{\Gamma_{\text{b}}} \hbar\gamma_{\text{m}} \frac{|z(0)|}{z_{\text{pm}}}. \tag{7.37}$$

Since the dot level is not broadened, we can make the work cost W arbitrarily small since any $\mu_f > \mu_{\text{S}}$ is enough to get $p = 0$. This is consistent with Landauer's principle since $k_{\text{B}}T \log 2 \xrightarrow[T\to 0]{} 0$.

If instead we take $\mu_0 = \mu_{\text{D}}$, then the Landauer erasure would correspond to the downward motion of the mechanics (with $z(0)$ maximum and $z(\frac{\pi}{\omega_{\text{eff}}})$ minimum) since we would go from $0 < p = \frac{\gamma_{\text{S}}}{\Gamma_{\text{b}}} < 1$ to $p = 1$. In that case,

$$W = \frac{\gamma_{\text{S}}}{\Gamma_{\text{b}}}(\mu_{\text{D}} - \mu_i) + \mu_f - \mu_{\text{D}} = \hbar\gamma_{\text{m}} \left(-\frac{\gamma_{\text{S}}}{\Gamma_{\text{b}}} \frac{z(0)}{z_{\text{pm}}} + \frac{z(\frac{\pi}{\omega_{\text{eff}}})}{z_{\text{pm}}} \right) < 0. \tag{7.38}$$

Level broadening of the dot

Here we neglect the tunnel barrier energy dependence to simplify the calculation and interpretation but take into account the broadening of the dot level. We compute the work for the information reset in Figure 7.4, that is the first half of

the mechanical period, starting at $t = 0$ at the minimum position (with $z(0) < 0$) and ending at the maximum position at $t = \frac{\pi}{\omega_{\text{eff}}}$. In the adiabatic approximation:

$$\begin{aligned} W &= \int_{\mu_i}^{\mu_f} \mathrm{d}\mu\, p(\mu) \\ &= \mu_f p(\mu_f) - \mu_i p(\mu_i) + \sum_{\nu=\mathrm{S,D}} \mu_\nu \frac{\gamma_\nu^{\text{in}}(\mu_i) - \gamma_\nu^{\text{in}}(\mu_f)}{\Gamma_\mathrm{b}} \\ &+ \sum_{\nu=\mathrm{S,D}} \frac{\hbar\Gamma_\nu}{4\pi} \log\left(\frac{(\hbar\Gamma_\mathrm{b})^2 + 4(\mu_\nu - \mu_f)^2}{(\hbar\Gamma_\mathrm{b})^2 + 4(\mu_\nu - \mu_i)^2}\right) \end{aligned} \tag{7.39}$$

where $z(0)$ is taken to be a minimum and $z(\frac{\pi}{\omega_{\text{eff}}})$ a maximum of the displacement. This expression (7.39) should in principle be computable from the amplitude of the motion we extract from Figure 7.5 (see Section 7.2.1) since it can be expressed in terms of the mechanical amplitude by using Equation (7.31).

In the case when $\mu_0 \gg \mu_\mathrm{S}, \hbar\Gamma_\mathrm{b}$, the work is

$$W \simeq \frac{\hbar\Gamma_\mathrm{b}}{2\pi}\frac{\Delta\mu}{\mu_0} \xrightarrow[\mu_0\to\infty]{} 0. \tag{7.40}$$

In the case when $\mu_0 = \mu_\mathrm{S}$ and we have taken a large enough bias to neglect the contribution from the drain,

$$p(\mu_i) \simeq \frac{\gamma_\mathrm{S}}{\Gamma_\mathrm{b}}, \qquad p(\mu_f) \simeq 0, \tag{7.41}$$

$$\gamma_\mathrm{S}^{\text{in}}(\mu_i) \simeq \gamma_\mathrm{S}, \qquad \gamma_\mathrm{S}^{\text{in}}(\mu_f) \simeq 0. \tag{7.42}$$

Therefore,

$$W \simeq \hbar\gamma_\mathrm{m}\frac{|z(0)|}{z_{\text{pm}}}\frac{\gamma_\mathrm{S}}{\Gamma_\mathrm{b}} + \frac{\hbar\Gamma_\mathrm{S}}{2\pi}\log\left(\left|\frac{z(\frac{\pi}{\omega_{\text{eff}}})}{z(0)}\right|\right). \tag{7.43}$$

Note that unlike in the previous case, we cannot make this work cost arbitrarily small since to get $p(\mu_f) \simeq 0$, we need to have $\mu - \mu_\mathrm{S} \gg \hbar\Gamma_\mathrm{b}$. This constraint gives us a minimal mechanical amplitude which in turn gives a minimum work cost.

7.5 Erasure with two fermion baths

In the previous section, we explored how to extract thermodynamic quantities from experimental data. However, a pertinent question arises: what is the fundamental

bound on the cost of information erasure in this scenario? Given the presence of Fermi reservoirs and the strong coupling of the quantum dot, quantum tunneling noise dominates over thermal noise. This indicates that we are operating under non-equilibrium conditions with athermal baths. In this section, we develop the theory for a generalized version of Landauer's principle, particularly tailored for fermion baths.

7.5.1 Average cyclic work cost of bit reset

We consider a quantum dot with an energy level μ, and suppose that the steady-state occupation probability varies as some function $n(\mu)$. Suppose that we can vary μ as a control parameter: the work cost of quasistatically transforming the configuration $(\mu_i, n(\mu_i)) \mapsto (\mu_f, n(\mu_f))$ is given by:

$$W = \int_{\mu_i}^{\mu_f} n(\mu)\,\mathrm{d}\mu. \tag{7.44}$$

However, this leaves the value of μ changed. A *cycle* for transforming the occupation state takes the configuration $(\mu_i, n(\mu_i)) \mapsto (\mu_i, n(\mu_f))$, with the energy level restored to its initial value. This can be achieved reversibly by *very quickly* resetting $\mu_f \mapsto \mu_i$ after the quasistatic step, fast enough that the state evolution is negligible and occupation remains at $n(\mu_f)$. This reset step incurs an extra work cost $\int_{\mu_f}^{\mu_i} n(\mu_f)\,\mathrm{d}\mu$, so that the work for the cycle is given by:

$$W = \int_{\mu_i}^{\mu_f} n(\mu) - n(\mu_f)\,\mathrm{d}\mu. \tag{7.45}$$

A case of particular interest is a cycle where the initial configuration is $(\mu_{\frac{1}{2}}, n = \frac{1}{2})$, and where the final configuration is either $(\mu_{\frac{1}{2}}, n = 0)$ or $(\mu_{\frac{1}{2}}, n = 1)$, with $\mu_{\frac{1}{2}}$ being the value of the dot's energy level for which the steady state occupation $n(\mu_{\frac{1}{2}}) = \frac{1}{2}$. If the occupation is taken to represent a bit of information, these processes represent a Landauer-like reset to a definite state, respectively 0 or 1 for the two cycles. Assume that $n(\mu)$ is monotone-decreasing, with $\lim_{\mu\to\infty} n(\mu) = 0$ and $\lim_{\mu\to-\infty} n(\mu) = 1$. The work cost W^0 of our reset-to-zero cycle is then given by (7.45) in the limit where $\mu_f \to \infty$:

$$W^0 = \int_{\mu_{\frac{1}{2}}}^{\infty} n(\mu)\,\mathrm{d}\mu, \tag{7.46}$$

noting that $n(\mu_f)$ vanishes. Likewise, the work cost W^1 of the reset-to-one cycle is given by taking $\mu_f \to -\infty$ and $n(\mu_f) \to 1$:

$$W^1 = \int_{-\infty}^{\mu_{\frac{1}{2}}} 1 - n(\mu)\,\mathrm{d}\mu, \tag{7.47}$$

In general, W^0 and W^1 may differ from each other, depending on the form of $n(\mu)$. In the context of information processing, 1s are required just as frequently as 0s for efficient coding. A fair measure of the cost of state reset is the *average* cyclic work cost of preparing either the empty state or the full occupancy state. Averaging eliminates any change in the system's internal energy[1], meaning that the work cost is solely associated with the entropic change. The quantity of interest is,

$$\overline{W} = \frac{1}{2}\left(W^0 + W^1\right). \tag{7.48}$$

7.5.2 Work is related to the spread of the occupation distribution

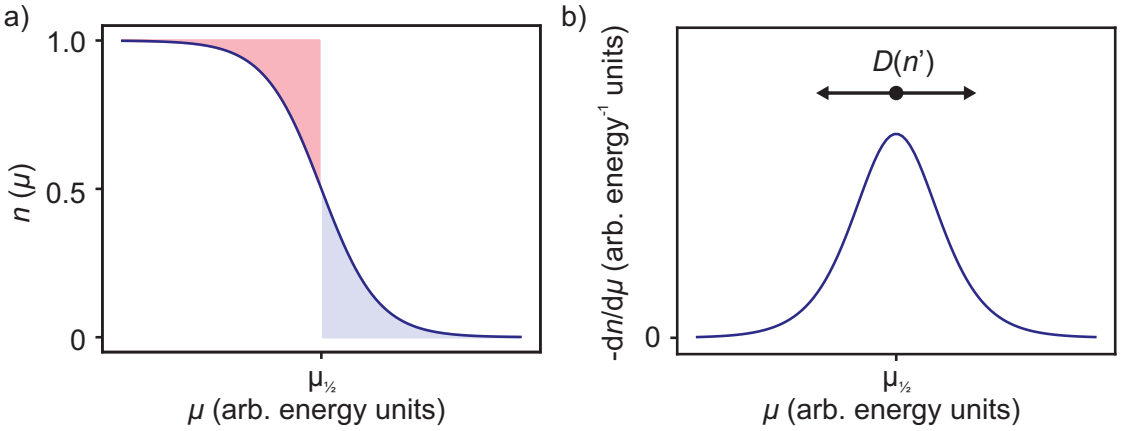


Figure 7.7: a) Occupation is described by a function n of the dot's energy level μ, which is monotone-decreasing from 1 to 0. We're interested in the work cost of producing a definite state. In general, the cost of producing a state with $n = 0$ or $n = 1$ (denoted as W^0 and W^1 respectively) may differ, so we consider the average, $\overline{W} = \frac{1}{2}(W^0 + W^1)$. **b)** The work cost of erasure is determined by the *spread* of the occupation distribution. The derivative $n'(\mu) = -\frac{dn}{d\mu}$ defines a probability density function, and the work cost is related to its mean absolute deviation D by $\overline{W} = \frac{1}{2}D(n')$. For the Fermi-Dirac distribution (pictured), $\overline{W} = k_{\mathrm{B}}T \ln 2$.

[1]The final configuration is either $(\mu = \mu_{\frac{1}{2}}, p = 0)$ or $(\mu = \mu_{\frac{1}{2}}, p = 1)$, so on average the internal energy is $\frac{1}{2}\mu_{\frac{1}{2}}$.

Our assumptions about $n(\mu)$ mean that $n'(\mu) = -\frac{dn}{d\mu}$ meets the definition of a probability density function, and $\mu_{\frac{1}{2}}$ represents the median of that distribution. Using integration by parts, the average work cost can be rewritten as [124]:

$$\begin{aligned}\overline{W} &= \frac{1}{2}\left(\int_{\mu_{\frac{1}{2}}}^{\infty} n(\mu)\,\mathrm{d}\mu + \int_{-\infty}^{\mu_{\frac{1}{2}}} 1 - n(\mu)\,\mathrm{d}\mu\right) \\ &= \frac{1}{2}\int_{-\infty}^{\infty} \left|\mu - \mu_{\frac{1}{2}}\right| \left(-\frac{dn}{d\mu}\right) \mathrm{d}\mu.\end{aligned} \tag{7.49}$$

The final integral in the above can be recognised as the *mean absolute deviation* of $n'(\mu)$, a measure of spread defined by $D(n') = \int_{-\infty}^{\infty} \left|\mu - \mu_{\frac{1}{2}}\right| n'(\mu)\mathrm{d}\mu$. The average work cost is directly related to the spread:

$$\overline{W} = \frac{1}{2}D(n'). \tag{7.50}$$

$n(\mu)$ need not be a canonical equilibrium distribution: it might instead represent a dynamical steady state for a dot in contact with multiple baths with different temperatures and chemical potentials. In that case, Equation (7.50) still applies, but may not reduce to the standard Landauer bound.

Incidentally, Equation (7.50) implies that the average cost of erasure from $n = \frac{1}{2}$ is always lower than for any other initial occupation, since the median is the point about which the mean absolute deviation is minimised.

7.5.3 Erasure with two Fermion baths

We consider a charge qubit encoded in a quantum dot which simultaneously interacts with two reservoirs with energy distributions $f_{\mathrm{S}}(\epsilon)$ and $f_{\mathrm{D}}(\epsilon)$ to calculate the cost of erasure with two Fermion baths. Take the reservoirs to be described by Fermi-Dirac distributions, $f_{\mathrm{S}}(\epsilon) = \frac{1}{1+\exp(\beta_{\mathrm{S}}(\epsilon-\mu_{\mathrm{S}}))}$ and $f_{\mathrm{D}}(\epsilon) = \frac{1}{1+\exp(\beta_{\mathrm{D}}(\epsilon-\mu_{\mathrm{D}}))}$, where $\mu_{\mathrm{S}} \geq \mu_{\mathrm{D}}$. Suppose, that the dot exchanges electrons with the source reservoir at rate Γ_{S} and with the drain reservoir at rate Γ_{D}. The tunneling rates are taken to be energy-independent. Let the dot have an unoccupied state with energy 0 and an occupied state with energy ϵ, with an occupation probability $p(\epsilon)$ (we will later

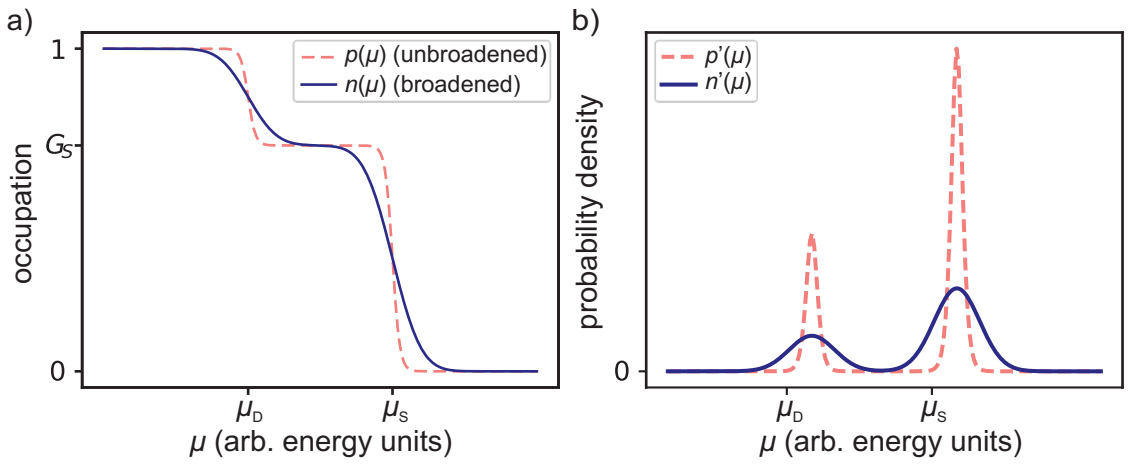


Figure 7.8: a) The steady-state occupation for a quantum dot in contact with two fermion reservoirs is described by a sum of Fermi-Dirac distributions weighted by the relative tunneling rates (pink dotted curve). Lifetime broadening has the effect of smoothing the occupation distribution (dark blue curve) by a function $g(\epsilon-\mu)$ which describes the spread of the dot's energy levels. Here, g is taken to be a Gaussian with standard deviation $\hbar\Gamma_{\text{broad}}$. **b)** The probability density function defined by the derivative of occupation has peaks at the source and drain chemical potentials. The width of each peak depends on the reservoir temperature and the lifetime broadening. The work cost of erasure $\overline{W}$ is determined by the mean absolute deviation of the entire bimodal distribution, which depends on source-drain bias as well as the temperature and lifetime broadening.

account for broadening of the energy level). Let us take the particle currents in and out of the dot to be the following:

$$\begin{aligned} \gamma_{\text{S}}^{\text{in}} &= \Gamma_{\text{S}} f_{\text{S}}(\epsilon)\,(1-p(\epsilon)), & \gamma_{\text{S}}^{\text{out}} &= \Gamma_{\text{S}}(1-f_{\text{S}}(\epsilon))\,p(\epsilon), \\ \gamma_{\text{D}}^{\text{in}} &= \Gamma_{\text{D}} f_{\text{D}}(\epsilon)\,(1-p(\epsilon)), & \gamma_{\text{D}}^{\text{out}} &= \Gamma_{\text{D}}(1-f_{\text{D}}(\epsilon))\,p(\epsilon). \end{aligned} \tag{7.51}$$

The steady-state occupation is achieved when the total currents in and out are balanced:

$$\begin{aligned} &\gamma_{\text{S}}^{\text{in}} + \gamma_{\text{D}}^{\text{in}} = \gamma_{\text{S}}^{\text{out}} + \gamma_{\text{D}}^{\text{out}} \\ &\implies p(\epsilon) = \frac{\Gamma_{\text{S}}}{\Gamma_{\text{S}}+\Gamma_{\text{D}}} f_{\text{S}}(\epsilon) + \frac{\Gamma_{\text{D}}}{\Gamma_{\text{S}}+\Gamma_{\text{D}}} f_{\text{D}}(\epsilon). \end{aligned} \tag{7.52}$$

Let us denote the *relative* tunneling rates $G_{\text{S}} = \frac{\Gamma_{\text{S}}}{\Gamma_{\text{S}}+\Gamma_{\text{D}}}$ and $G_{\text{D}} = \frac{\Gamma_{\text{D}}}{\Gamma_{\text{S}}+\Gamma_{\text{D}}}$, noting $G_{\text{S}} + G_{\text{D}} = 1$.

Lifetime broadening

The energy level of the quantum dot is subject to lifetime broadening. In this case the control parameter μ does not represent the exact energy level, but instead the

mean value of a probabilistic distribution of energies $g(\epsilon, \mu)$. Let us assume that the distribution does not change shape depending on μ but is only shifted; then we can write it as $g(\epsilon - \mu)$. If the occupation of an exact energy level ϵ is described by $p(\epsilon)$, then the occupation as a function of μ is given by the cross-correlation,

$$n(\mu) = g \star p(\mu) = \int_{-\infty}^{\infty} g(\epsilon - \mu) p(\epsilon) d\epsilon. \tag{7.53}$$

Using standard properties of cross-correlation, the probability density function is $n'(\mu) = g \star p'(\mu)$, where $p'(\epsilon) = -\frac{dp}{d\epsilon}$. Therefore we can relate the average work cost of to the mean absolute deviation of the cross-correlation:

$$\overline{W} = \frac{1}{2} D(g \star p'). \tag{7.54}$$

7.5.4 Bounding the work cost of erasure

Given values of the electrochemical potential, temperature and tunnelling rate for each reservoir, it is straightforward to numerically evaluate $\overline{W}$ using the above model; but there is no closed analytical expression. In fact it is difficult even to invert $n(\mu)$ to obtain a formula for $\mu_{\frac{1}{2}}$. However, it is possible to place analytic *bounds* on $\overline{W}$, and thereby analyse the relevant energy scales and their interplay. We will refer to general properties of the mean absolute deviation established in lemmas 1 and 2 (see the following section). Combining equations (7.53) and (7.54), it can be seen that:

$$\overline{W} = \frac{1}{2} D(g \star (G_{\mathrm{S}} f'_{\mathrm{S}} + G_{\mathrm{D}} f'_{\mathrm{D}})), \tag{7.55}$$

where $f'_\nu(\epsilon) = -\frac{d}{d\mu} f_\nu(\epsilon)$, for $\nu = \mathrm{S,D}$; which can be explicitly written as:

$$f'_\nu(\epsilon) = \frac{\beta_\nu e^{\beta_\nu(\epsilon - \mu_\nu)}}{(1 + e^{\beta_\nu(\epsilon - \mu_\nu)})^2}. \tag{7.56}$$

f'_ν defines a probability density function with median equal to the electrochemical potential μ_ν. The mean absolute deviation is given by:

$$D(f'_\nu) = \frac{2 \ln 2}{\beta_\nu}. \tag{7.57}$$

Returning to (7.55), we can apply lemmas 1(i) followed by 2(i), using the fact that that $f'_\nu(\mu_\nu + \epsilon) = f'_\nu(\mu_\nu - \epsilon)$ for all ϵ:

$$\begin{aligned}\overline{W} &\geq \frac{1}{2}\max\Big\{D(g),\ \ D(G_{\rm S}f'_{\rm S} + G_{\rm D}f'_{\rm D})\Big\} \\ &\geq \frac{1}{2}\max\Big\{D(g),\ \ G_{\rm S}D(f'_{\rm S}) + G_{\rm D}D(f'_{\rm D}),\ \ \min\{G_{\rm S},G_{\rm D}\}(\mu_{\rm S}-\mu_{\rm D})\Big\} \\ &= \max\left\{\frac{1}{2}D(g),\ \ \left(\tfrac{G_{\rm S}}{\beta_{\rm S}} + \tfrac{G_{\rm D}}{\beta_{\rm D}}\right)\ln 2,\ \ \frac{1}{2}\min\{G_{\rm S},G_{\rm D}\}(\mu_{\rm S}-\mu_{\rm D})\right\}.\end{aligned} \tag{7.58}$$

In the above, we have effectively identified three independent energy scales which contribute to the work cost of erasure. Let us denote them as follows:

$$\begin{aligned}E_{\rm therm} &= \left(\tfrac{G_{\rm S}}{\beta_{\rm S}} + \tfrac{G_{\rm D}}{\beta_{\rm D}}\right)\ln 2 \\ E_{\rm bias} &= \frac{1}{2}\min\{G_{\rm S},G_{\rm D}\}(\mu_{\rm S}-\mu_{\rm D}) \\ E_{\rm broad} &= \frac{1}{2}D(g).\end{aligned} \tag{7.59}$$

$E_{\rm therm}$ relates to thermal broadening, and has the familiar form of the Landauer energy cost $k_{\rm B}T\ln 2$, albeit with the temperature replaced by an average of the two reservoir temperatures weighted by the relative tunnelling rates. $E_{\rm bias}$ relates to the potential bias between source and drain reservoirs: the larger the bias, the larger the cost of erasure - although the effect is mitigated when the tunneling rate from one reservoir dominates the other (in that limit we effectively recover the single bath case). Finally, $E_{\rm broad}$ relates to the broadening of the dot's energy level, and will typically be of the order $\hbar\Gamma_{\rm tot}$, where the total tunneling rate $\Gamma_{\rm tot} = \Gamma_{\rm S} + \Gamma_{\rm D}$ quantifies the reciprocal of the typical time spent before tunneling out of the dot.

Note that Equation (7.58) is not a tight bound: aside from a few limiting cases it cannot be saturated, and so far we cannot rule out that in fact an optimal erasure protocol would require much *more* work that the right hand side of Equation (7.58) suggests. However, applying lemmas 1(ii) and 2(ii) to Equation (7.55), we can upper-bound the minimum work cost:

$$\begin{aligned}\overline{W} &\leq \frac{1}{2}\Big(D(g) \ \ + \ \ D(G_{\rm S}f'_{\rm S} + G_{\rm D}f'_{\rm D})\Big) \\ &\leq \frac{1}{2}\Big(D(g) \ \ + \ \ G_{\rm S}D(f'_{\rm S}) + G_{\rm D}D(f'_{\rm D}) \ \ + \ \ \min\{G_{\rm S},G_{\rm D}\}(\mu_{\rm S}-\mu_{\rm D})\Big) \\ &= \frac{1}{2}D(g) \ \ + \ \ \left(\tfrac{G_{\rm S}}{\beta_{\rm S}} + \tfrac{G_{\rm D}}{\beta_{\rm D}}\right)\ln 2 \ \ + \ \ \frac{1}{2}\min\{G_{\rm S},G_{\rm D}\}(\mu_{\rm S}-\mu_{\rm D}).\end{aligned} \tag{7.60}$$

Putting this together with (7.58), we have:

$$\max\left\{E_{\text{therm}}, E_{\text{bias}}, E_{\text{broad}}\right\} \leq \overline{W} \leq E_{\text{therm}} + E_{\text{bias}} + E_{\text{broad}}. \tag{7.61}$$

Recall that $\overline{W}$ is the average cost of preparing a 0 or 1 state using an ideal, thermodynamically reversible process. If the erasure were carried out in an inefficient manner, there is certainly nothing preventing the cost from exceeding $E_{\text{therm}} + E_{\text{bias}} + E_{\text{broad}}$: but in principle it is possible to do better.

Equation (7.61) tells that if any one of the three energy scales dominates the other two, it essentially solely determines the cost of erasure. For example if the source-drain bias were very much larger than the thermal energy and lifetime broadening, then we would have $E_{\text{bias}} \gg E_{\text{therm}}, E_{\text{broad}}$, and therefore $\overline{W} \approx E_{\text{bias}}$. Conversely, if any one of the energy scales is much smaller than the other two, then it is functionally irrelevant to the cost of erasure.

7.5.5 Bounds on the mean absolute deviation

Lemma 1. Let f and g be probability density functions. Then the mean absolute deviation D of the cross-correlation function $f \star g$ is bounded by:

$$\begin{aligned} &\text{(i)} && D(f \star g) \geq \max\{D(f), D(g)\} \\ &\text{(ii)} && D(f \star g) \leq D(f) + D(g). \end{aligned} \tag{7.62}$$

Proof. Recall $f \star g = \int_{-\infty}^{\infty} f(y)g(y-x)dy = \int_{-\infty}^{\infty} f(y+x)g(y)dy$. For the lower bound, (i), we have:

$$\begin{aligned} D(f \star g) &= \int_{-\infty}^{\infty} |x - m_{fg}| \left(\int f(y+x)g(y)dy \right) dx \\ &= \int \left(\int |x - m_{fg}| f(y+x)dx \right) g(y)dy \\ &\geq \int D(f)g(y)dy \\ &= D(f). \end{aligned} \tag{7.63}$$

Since $f \star g(x) = g \star f(-x)$, and since the mean absolute deviation of a function $h(x)$ is equal to that of $h(-x)$, then by the above reasoning we also have $D(f \star g) \geq D(g)$,

which completes the proof of (i). On the other hand to show the upper bound,

$$\begin{aligned} D(f\star g) &= \int_{-\infty}^{\infty} |u-m_{fg}| f\star g(u)du \\ &\leq \int |u-(m_f-m_g)| f\star g(u)du \\ &= \int |u-(m_f-m_g)| \left(\int f(u+y)g(y)dy\right) du \\ &= \int \left(\int |u-(m_f-m_g)| f(u+y)du\right) g(y)dy \\ &= \int \left(\int |x-y-(m_f-m_g)| f(x)dx\right) g(y)dy \\ &\leq \iint \left(|x-m_f|+|y-m_g|\right) f(x)g(y)dxdy \\ &= \int \left(\int |x-m_f| f(x)dx\right) g(y)dy + \int \left(\int |y-m_g| g(y)dy\right) f(x)dx \\ &= \int D(f)g(y)dy + \int D(g)f(x)dx \\ &= D(f)+D(g) \end{aligned} \tag{7.64}$$

In the fifth line we used the substitution $x = u + y$. This completes the proof of (ii).

Lemma 2. Let f be a probability density function which is even about its median m_f, such that for all x, $f(m_f + x) = f(m_f - x)$. Similarly, let g be a probability density function which is even about its median m_g, where $m_g \leq m_f$. Let p_f and p_g be probabilities such that $p_f + p_g = 1$. Then the mean absolute deviation of the convex sum $p_f f + p_g g$ is bounded by:

$$\begin{aligned} &\text{(i)} \qquad D(p_f f + p_g g) \geq \max\left\{p_f D(\mu_f) + p_g D(\mu_g),\ \min\{p_f, p_g\}(m_f - m_g)\right\} \\ &\text{(ii)} \qquad D(p_f f + p_g g) \leq p_f D(\mu_f) + p_g D(\mu_g) + \min\{p_f, p_g\}(m_f - m_g). \end{aligned} \tag{7.65}$$

Proof. Let us denote $h(x) = p_f f(x) + p_g g(x)$; note that h is also a probability density function and its median $m_h \in [m_g, m_f]$. We will use the fact that the median minimises the mean absolute deviation, in that for all a, $\int_{-\infty}^{\infty} |x-a| f(x)dx \geq \int_{-\infty}^{\infty} |x - m_f| f(x)dx$. Then the mean absolute deviation of h is bounded as follows:

$$\begin{aligned} D(h) &= \int_{-\infty}^{\infty} |x-m_h|(p_f f(x) + p_g g(x))dx \\ &= p_f \int |x-m_h| f(x)dx + p_g \int |x-m_h| g(x)dx \\ &\geq p_f \int |x-m_f| f(x)dx + p_g \int |x-m_g| g(x)dx \\ &= p_f D(f) + p_g D(g). \end{aligned} \tag{7.66}$$

On the other hand, we also have:

$$\begin{aligned}\int_{-\infty}^{\infty}|x-m_h|f(x)dx &= \int_{-\infty}^{m_f}(x-m_h)f(x)dx+\int_{m_f}^{\infty}(x-m_h)f(x)dx\\ &\quad+2\int_{-\infty}^{m_h}|x-m_h|f(x)dx\\ &=\int_0^{\infty}(m_f-u-m_h)f(m_f-u)du\\ &\quad+\int_0^{\infty}(m_f+u-m_h)f(m_f+u)du\\ &\quad+2\int_{-\infty}^{m_h}|x-m_h|f(x)dx\\ &=2(m_f-m_h)\int_0^{\infty}f(m_f+u)du\\ &\quad+2\int_{-\infty}^{m_h}|x-m_h|f(x)dx\\ &=m_f-m_h+2\int_{-\infty}^{m_h}|x-m_h|f(x)dx.\end{aligned} \tag{7.67}$$

We have used that $f(m_f+x)=f(m_f-x)$. In the final line we used that $\int_{m_f}^{\infty}f(x)dx=\frac{1}{2}$, by definition of the median. By a similar argument for g,

$$\int_{-\infty}^{\infty}|x-m_h|g(x)dx=m_h-m_g+2\int_{m_h}^{\infty}|x-m_h|g(x)dx. \tag{7.68}$$

Combining (7.67) and (7.68):

$$\begin{aligned}D(h)&=p_f(m_f-m_h)+p_g(m_h-m_g)\\ &\quad+2\left(p_f\int_{-\infty}^{m_h}|x-m_h|f(x)dx\right.\\ &\quad\left.+p_g\int_{m_h}^{\infty}|x-m_h|g(x)dx\right)\end{aligned} \tag{7.69}$$

Since the integral terms are always positive, it follows that:

$$\begin{aligned}D(h)&\geq p_f(m_f-m_h)+p_g(m_h-m_g)\\ &\geq\min\{p_f,p_g\}(m_f-m_g).\end{aligned} \tag{7.70}$$

Taking inequalities (7.66) and (7.70) together, the claim (i) follows.

Moreover, since $D(h) = \min_m \int_{-\infty}^{\infty} |x-m|h(x)\,dx$, then from (7.69) we have:

$$\begin{aligned}
D(h) &= \min_m \{p_f(m_f - m) + p_g(m - m_g) \\
&\quad + 2\left(p_f \int_{-\infty}^{m} |x-m|f(x)dx \right. \\
&\quad \left. + p_g \int_{m}^{\infty} |x-m|g(x)dx\right)\Big\} \\
&\leq p_f(m_f - m_g) + p_g(m_g - m_g) \\
&\quad + 2p_f \int_{-\infty}^{m_g} |x-m_g|f(x)dx \\
&\quad + 2p_g \int_{m_g}^{\infty} |x-m_g|g(x)dx \\
&= p_f(m_f - m_g) + p_g D(g) \\
&\quad + 2p_f \int_{-\infty}^{m_g} |x-m_g|f(x)dx \\
&= p_f(m_f - m_g) + p_g D(g) \\
&\quad + 2p_f \int_{-\infty}^{m_f} |x-m_f|f(x)dx \\
&= p_f(m_f - m_g) + p_g D(g) + p_f D(f).
\end{aligned} \tag{7.71}$$

We have used the fact that $m_f \geq m_g$, and in the final line we used the assumption that f is even about m_f. If we instead take $m = m_f$, then by the same arguments,

$$D(h) \leq p_g(m_f - m_g) + p_g D(g) + p_f D(f). \tag{7.72}$$

Combining (7.71) and (7.72), we certainly have $D(h) \leq \min\{p_f, p_g\}(m_f - m_g) + p_f D(f) + p_g D(g)$, which was the claimed bound (ii).

7.6 Quantifying energy dissipation

We have methods to estimate the work done in changing the occupation state of the quantum dot, and we believe that this work is done *almost* reversibly, since the tunneling rates are much faster than the mechanical frequency, meaning that the process is effectively quasistatic. However, it strengthens our argument if we have an empirical way to quantify the energy dissipated in changing the occupation of the dot – which we expect to be a small fraction of the work done.

In the oscillator-dot system, there is periodic conversion of kinetic energy into a combination of elastic potential of the nanotube, and electrostatic potential of

the quantum dot. In reality, neither conversion process is completely reversible, and in each oscillation cycle some energy will be lost to both mechanical damping, and to resistance in the charging and discharging of the dot. Both dissipation mechanisms contribute to the overall quality factor of the system, defined as $Q = 2\pi \times \frac{\text{total energy}}{\text{energy dissipated per cycle}}$.

For oscillations outside the bias window, the change in the dot occupation is negligible. Therefore, we expect dissipation to result only from mechanical damping, and we should be able to measure a quality factor Q_{mech} associated solely with this mechanism. By comparing quality factor measurements inside and outside the bias window, we may therefore be able to infer the amount of energy dissipated in changing the dot occupation state – provided we also know how much energy is going into elastic and electrostatic potential respectively.

Consider the nanotube-dot system at maximum displacement, such that it is stationary with zero kinetic energy, and its total energy U_{tot} is given by the sum of elastic and electrostatic potential energy (which are both at their maximal values):

$$U_{\text{tot}} = V_{\text{mech}}^{\text{max}} + V_{\text{dot}}^{\text{max}}. \tag{7.73}$$

Over the course of one full mechanical oscillation cycle, the total energy dissipated by the system is given by a sum of contributions from the mechanical damping and dot resistance:

$$\Delta U_{\text{tot}} = \Delta U_{\text{mech}} + \Delta U_{\text{dot}}. \tag{7.74}$$

This allows us to express ΔU_{dot} in terms of the total and mechanical quality factors:

$$\begin{aligned} \frac{Q_{\text{tot}}}{2\pi} &= \frac{U_{\text{tot}}}{\Delta U_{\text{mech}} + \Delta U_{\text{dot}}} \\ \implies \Delta U_{\text{dot}} &= 2\pi \frac{U_{\text{tot}}}{Q_{\text{tot}}} - \Delta U_{\text{mech}} \\ &= 2\pi \left[\frac{U_{\text{tot}}}{Q_{\text{tot}}} - \frac{V_{\text{mech}}^{\text{max}}}{Q_{\text{mech}}} \right], \end{aligned} \tag{7.75}$$

where $Q_{\text{mech}} = 2\pi \frac{V_{\text{mech}}^{\text{max}}}{\Delta U_{\text{mech}}}$. Assuming that the mechanical quality factor is independent of gate voltage, it should be possible to find Q_{mech} using the control protocol

in Figure 7.4. It should also be possible to determine $V_{\mathrm{mech}}^{\mathrm{max}}$ from the measured amplitude z using the formula $V_{\mathrm{mech}}^{\mathrm{max}} = \frac{1}{2}m\omega_m^2 z^2$, where m is the estimated effective oscillating mass, and ω_m is the bare mechanical frequency.

On the other hand, $V_{\mathrm{dot}}^{\mathrm{max}}$ can be estimated using the method in Section 7.4, integrating $p(\mu(z))$ for the half cycle from minimum to maximum displacement. If $V_{\mathrm{dot}}^{\mathrm{max}} \ll V_{\mathrm{mech}}^{\mathrm{max}}$, then to a good approximation we can take $U_{\mathrm{tot}} = V_{\mathrm{mech}}^{\mathrm{max}}$, simplifying Equation(7.75) to the following:

$$\Delta U_{\mathrm{dot}} = \pi m\omega_m^2 z^2 \left[\frac{1}{Q_{\mathrm{tot}}} - \frac{1}{Q_{\mathrm{mech}}}\right]. \tag{7.76}$$

Note that the above expresses the energy dissipated while changing the dot occupation over a *whole* mechanical period (i.e., a charge and discharge cycle). We might assume that during the 'erasure' stroke, the dissipated energy is $\frac{1}{2}\Delta U_{\mathrm{dot}}$.

7.7 Conclusion & Outlook

This chapter represents the culmination of the work presented in this thesis. The earlier chapters were devoted to developing the experimental setup and theoretical model, as well as understanding the back-action of single-electron tunneling on mechanics, and vice versa. A significant change was introduced in the experimental setup by incorporating an electrical cavity, providing a direct probe of the mechanical amplitude.

We extended the theoretical model from Chapter 4 to include energy-dependent tunnel barriers and the influence of electrostatic tensioning on the mechanical frequency. This allowed us to calculate how thermodynamic work can be estimated from the amplitude of mechanical oscillations, an experimentally accessible quantity.

With the objective of exploring thermodynamics at the nanoscale, taking inspiration from a piston coupled to a working fluid, this system presented exciting opportunities: the presence of Fermi reservoirs and the strong coupling of the quantum dot to these reservoirs lead to non-equilibrium conditions and quantum tunneling noise.

In examining the theory of erasure cost under these conditions, where thermal equilibrium cannot be assumed, we discovered that the work is related to the spread of the occupation distribution. This implies that the work cost depends on the probability of the electron being occupied or not. We determined that, depending on various conditions, the bound might be defined by the effective temperature (reducing to the original Landauer's erasure), an energy scale defined by tunneling, or by the difference in electrochemical potentials. We conclude with the observation that connecting experimentally accessible and extractable quantities to fundamental bounds, as elucidated in this chapter, remains an ongoing area of work.

8 Conclusion

This thesis has provided a comprehensive exploration of nanoelectromechanical systems, with a focus on the intricate dynamics of carbon nanotubes and their applications in understanding non-equilibrium thermodynamics. The research journey, detailed across several chapters, highlights the interplay between mechanical and electronic degrees of freedom in these systems and their implications in the broader context of thermodynamic principles.

The thesis began with a foundational overview of thermodynamic principles, particularly emphasizing the shift from traditional macroscopic systems to the exploration of isolated single degrees of freedom. This transition underpins the study of stochastic and quantum thermodynamics, setting the stage for the subsequent chapters.

In Chapter 3, the experimental techniques utilized for the study were elucidated, including the methods for defining single and double quantum dots in carbon nanotubes. This chapter was critical in detailing the nanofabrication techniques and operational principles of key components, such as the radiofrequency amplifier based on a superconducting quantum interference device, which is essential for sensitive probing mechanical motion in carbon nanotubes.

Chapter 4 delved into the interplay between electron tunneling and mechanical motion in carbon nanotubes. A theoretical model characterizing this relationship

was introduced, which laid the groundwork for the experimental observations detailed in the chapter.

The findings in Chapter 5 revealed that variations in the rate of electron tunneling through carbon nanotubes, combined with electromechanical interactions, can lead to self-sustained oscillations in the mechanical resonator. This chapter highlighted the complex behaviors of these oscillations, including spontaneous starts, stops, and bistability, enriching our understanding of the dynamics in nanomechanical systems.

Chapter 6 presented insights into the non-linear restoring forces experienced by carbon nanotubes, arising from their geometric structure and electrostatic forces. The chapter emphasized the significance of Duffing-like forces in influencing both mechanical and electronic properties, thereby facilitating a deeper investigation into limit cycles and chaos in nanomechanical systems.

The final chapter integrated insights from the previous chapters to examine the thermodynamics of information under non-equilibrium conditions. The chapter uniquely utilized the mechanical motion of carbon nanotubes as a piston and the quantum dot as a working fluid, providing a novel perspective on the thermodynamic cost of information processing in quantum systems.

In summary, this thesis has advanced our understanding of the dynamics and properties of nanoelectromechanical systems, with a particular focus on carbon nanotubes. The findings contribute significantly to the field of non-equilibrium thermodynamics, offering new perspectives and methodologies for future research. The exploration of quantum effects in these systems opens up new possibilities for technological applications and theoretical advancements in the realm of quantum thermodynamics.

Bibliography

[1] Robert G. Knobel and Andrew N. Cleland. "Nanometre-scale displacement sensing using a single electron transistor". In: *Nature* 424.6946 (2003), pp. 291–293. ISSN: 1476-4687. DOI: 10.1038/nature01773.

[2] M. D. LaHaye et al. "Approaching the Quantum Limit of a Nanomechanical Resonator". In: *Science* 304.5667 (2004), pp. 74–77. ISSN: 1095-9203. DOI: 10.1126/science.1094419.

[3] A Naik et al. "Cooling a nanomechanical resonator with quantum back-action". en. In: *Nature* 443.7108 (2006), pp. 193–196.

[4] Yuma Okazaki et al. "Quantum point contact displacement transducer for a mechanical resonator at sub-Kelvin temperatures". In: *Applied Physics Letters* 103.19 (2013). ISSN: 1077-3118. DOI: 10.1063/1.4828890.

[5] N. E. Flowers-Jacobs, D. R. Schmidt, and K. W. Lehnert. "Intrinsic Noise Properties of Atomic Point Contact Displacement Detectors". In: *Physical Review Letters* 98.9 (2007). ISSN: 1079-7114. DOI: 10.1103/physrevlett.98.096804.

[6] J. D. Teufel et al. "Nanomechanical motion measured with an imprecision below that at the standard quantum limit". In: *Nature Nanotechnology* 4.12 (2009), pp. 820–823. ISSN: 1748-3395. DOI: 10.1038/nnano.2009.343.

[7] C. A. Regal, J. D. Teufel, and K. W. Lehnert. "Measuring nanomechanical motion with a microwave cavity interferometer". In: *Nature Physics* 4.7 (2008), pp. 555–560. ISSN: 1745-2481. DOI: 10.1038/nphys974.

[8] Srujan Meesala et al. "Enhanced Strain Coupling of Nitrogen-Vacancy Spins to Nanoscale Diamond Cantilevers". In: *Physical Review Applied* 5.3 (2016). ISSN: 2331-7019. DOI: 10.1103/physrevapplied.5.034010.

[9] Z. Y. Xu et al. "Deterministically entangling distant nitrogen-vacancy centers by a nanomechanical cantilever". In: *Physical Review A* 80.2 (2009). ISSN: 1094-1622. DOI: 10.1103/physreva.80.022335.

[10] *Nanoelectronics: Materials, Devices, Applications*. Wiley, 2017. ISBN: 9783527800728. DOI: 10.1002/9783527800728.

[11] Benoit Witkamp, Menno Poot, and Herre S. J. van der Zant. "Bending-Mode Vibration of a Suspended Nanotube Resonator". In: *Nano Letters* 6.12 (2006), pp. 2904–2908. ISSN: 1530-6992. DOI: 10.1021/nl062206p.

[12] Shoichi Toyabe et al. "Experimental demonstration of information-to-energy conversion and validation of the generalized Jarzynski equality". In: *Nature Physics* 6.12 (2010), pp. 988–992. ISSN: 1745-2481. DOI: 10.1038/nphys1821.

[13] D. Collin et al. “Verification of the Crooks fluctuation theorem and recovery of RNA folding free energies”. In: *Nature* 437.7056 (2005), pp. 231–234. ISSN: 1476-4687. DOI: 10.1038/nature04061.

[14] A. Hofmann et al. “Equilibrium free energy measurement of a confined electron driven out of equilibrium”. In: *Phys. Rev. B* 93 (3 2016), p. 035425. DOI: 10.1103/PhysRevB.93.035425.

[15] T. P. Xiong et al. “Experimental Verification of a Jarzynski-Related Information-Theoretic Equality by a Single Trapped Ion”. In: *Phys. Rev. Lett.* 120 (1 2018), p. 010601. DOI: 10.1103/PhysRevLett.120.010601.

[16] MD LaHaye et al. “Nanomechanical measurements of a superconducting qubit”. In: *Nature* 459.7249 (2009), pp. 960–964. DOI: 10.1038/nature08093.

[17] Joel Moser et al. “Ultrasensitive force detection with a nanotube mechanical resonator”. In: *Nat. Nanotechnol.* 8.7 (2013), pp. 493–496. DOI: 10.1038/nnano.2013.97.

[18] Yue Wang, G. Micchi, and F. Pistolesi. “Sensitivity of the Mixing-Current Technique for the Detection of Mechanical Motion in the Coherent Tunnelling Regime”. In: *Journal of Physics: Condensed Matter* 29.46 (2017), p. 465304. ISSN: 0953-8984. DOI: 10.1088/1361-648X/aa903e.

[19] SL De Bonis et al. “Ultrasensitive displacement noise measurement of carbon nanotube mechanical resonators”. In: *Nano Lett.* 18.8 (2018), pp. 5324–5328. DOI: 10.1021/acs.nanolett.8b02437.

[20] A. D. O’Connell et al. “Quantum Ground State and Single-Phonon Control of a Mechanical Resonator”. In: *Nature* 464.7289 (2010), pp. 697–703. ISSN: 1476-4687. DOI: 10.1038/nature08967.

[21] TA Palomaki et al. “Entangling mechanical motion with microwave fields”. In: *Science* 342.6159 (2013), pp. 710–713. DOI: 10.1126/science.1244563.

[22] AP Reed et al. “Faithful conversion of propagating quantum information to mechanical motion”. In: *Nat. Phys.* 13.12 (2017), pp. 1163–1167. DOI: 10.1038/nphys4251.

[23] Markus Aspelmeyer, Tobias J. Kippenberg, and Florian Marquardt. “Cavity Optomechanics”. In: *Rev. Mod. Phys.* 86.4 (2014), pp. 1391–1452. DOI: 10.1103/RevModPhys.86.1391.

[24] Cyril Elouard, Maxime Richard, and Alexia Auffèves. “Reversible Work Extraction in a Hybrid Opto-Mechanical System”. In: *New J. Phys.* 17.5 (2015), p. 055018. DOI: 10.1088/1367-2630/17/5/055018.

[25] Juliette Monsel, Cyril Elouard, and Alexia Auffèves. “An Autonomous Quantum Machine to Measure the Thermodynamic Arrow of Time”. English. In: *Npj Quantum Inf.* 4.1 (2018), p. 59. ISSN: 2056-6387. DOI: 10.1038/s41534-018-0109-8.

[26] CW Wächtler, P Strasberg, and G Schaller. “Proposal of a realistic stochastic rotor engine based on electron shuttling”. In: *Phys. Rev. Applied* 12.2 (2019), p. 024001. DOI: 10.1103/PhysRevApplied.12.024001.

[27] Christopher W. Wächtler et al. "Stochastic Thermodynamics of Self-Oscillations: The Electron Shuttle". In: *New J. Phys.* 21.7 (2019), p. 073009. ISSN: 1367-2630. DOI: 10.1088/1367-2630/ab2727.

[28] Adrian Bachtold, Joel Moser, and MI Dykman. "Mesoscopic physics of nanomechanical systems". In: *arXiv preprint arXiv:2202.01819* (2022).

[29] Gary A Steele et al. "Strong coupling between single-electron tunneling and nanomechanical motion". In: *Science* 325.5944 (2009), pp. 1103–1107. DOI: 10.1126/science.1176076.

[30] Benjamin Lassagne et al. "Coupling Mechanics to Charge Transport in Carbon Nanotube Mechanical Resonators". In: *Science* 325.5944 (2009), pp. 1107–1110. ISSN: 0036-8075. DOI: 10.1126/science.1174290.

[31] Klemens Hammerer et al. "Strong coupling of a mechanical oscillator and a single atom". In: *Phys. Rev. Lett.* 103.6 (2009), p. 063005. DOI: 10.1103/PhysRevLett.103.063005.

[32] Steven D Bennett et al. "Strong electromechanical coupling of an atomic force microscope cantilever to a quantum dot". In: *Phys. Rev. Lett.* 104.1 (2010), p. 017203. DOI: 10.1103/PhysRevLett.104.017203.

[33] David Hunger et al. "Resonant coupling of a Bose-Einstein condensate to a micromechanical oscillator". In: *Phys. Rev. Lett.* 104.14 (2010), p. 143002. DOI: 10.1103/PhysRevLett.104.143002.

[34] Peter Rabl et al. "Strong magnetic coupling between an electronic spin qubit and a mechanical resonator". In: *Phys. Rev. B* 79.4 (2009), p. 041302. DOI: 10.1103/PhysRevB.79.041302.

[35] Shimon Kolkowitz et al. "Coherent sensing of a mechanical resonator with a single-spin qubit". In: *Science* 335.6076 (2012), pp. 1603–1606. DOI: 10.1126/science.1216821.

[36] B. H. Schneider et al. "Coupling carbon nanotube mechanics to a superconducting circuit". In: *Sci. Rep.* 2.599 (2012), pp. 1–5. ISSN: 2045-2322. DOI: 10.1038/srep00599.

[37] Philipp Treutlein et al. "Hybrid mechanical systems". In: *Cavity Optomechanics*. Berlin: Springer, 2014, pp. 327–351.

[38] J-M Pirkkalainen et al. "Cavity Optomechanics Mediated by a Quantum Two-Level System". In: *Nat. Commun.* 6.1 (2015), pp. 1–6. DOI: 10.1038/ncomms7981.

[39] J.-M. Pirkkalainen et al. "Hybrid Circuit Cavity Quantum Electrodynamics with a Micromechanical Resonator". In: *Nature* 494.7436 (2013), pp. 211–215. ISSN: 0028-0836. DOI: 10.1038/nature11821.

[40] O. Arcizet et al. "A Single Nitrogen-Vacancy Defect Coupled to a Nanomechanical Oscillator". In: *Nat. Phys.* 7.11 (2011), p. 879. ISSN: 1745-2481. DOI: 10.1038/nphys2070.

[41] I. Yeo et al. "Strain-Mediated Coupling in a Quantum DotMechanical Oscillator Hybrid System". In: *Nat. Nanotechnol.* 9 (2014), pp. 106–110. DOI: 10.1038/nnano.2013.274.

[42] Jan Kettler et al. “Inducing micromechanical motion by optical excitation of a single quantum dot”. In: *Nat. Nanotechnol.* 16.3 (2021), pp. 283–287. ISSN: 1748-3395. DOI: 10.1038/s41565-020-00814-y.

[43] PD Nation, J Suh, and MP Blencowe. “Ultrastrong Optomechanics Incorporating the Dynamical Casimir Effect”. In: *Phys. Rev. A* 93.2 (2016), p. 022510. DOI: 10.1103/PhysRevA.93.022510.

[44] Olga Shevchuk, Gary A Steele, and Ya M Blanter. “Strong and Tunable Couplings in Flux-Mediated Optomechanics”. In: *Phys. Rev. B* 96.1 (2017), p. 014508. DOI: 10.1103/PhysRevB.96.014508.

[45] Kiran E Khosla et al. “Displacemon Electromechanics: How to Detect Quantum Interference in a Nanomechanical Resonator”. In: *Phys. Rev. X* 8.2 (2018), p. 021052. DOI: 10.1103/PhysRevX.8.021052.

[46] Marios Kounalakis, Yaroslav M Blanter, and Gary A Steele. “Flux-Mediated Optomechanics with a Transmon Qubit in the Single-Photon Ultrastrong-Coupling Regime”. In: *Phys. Rev. Res.* 2.2 (2020), p. 023335. DOI: 10.1103/PhysRevResearch.2.023335.

[47] Lukas Neumeier and Darrick E Chang. “Exploring Unresolved Sideband, Optomechanical Strong Coupling Using a Single Atom Coupled to a Cavity”. In: *New J. Phys.* 20.8 (2018), p. 083004. DOI: 10.1088/1367-2630/aad497.

[48] Lukas Neumeier, Tracy E Northup, and Darrick E Chang. “Reaching the Optomechanical Strong-Coupling Regime with a Single Atom in a Cavity”. In: *Phys. Rev. A* 97.6 (2018), p. 063857. DOI: 10.1103/PhysRevA.97.063857.

[49] T. T. Heikkilä et al. “Enhancing Optomechanical Coupling via the Josephson Effect”. In: *Phys. Rev. Lett.* 112.20 (2014), p. 203603. DOI: 10.1103/PhysRevLett.112.203603.

[50] AJ Rimberg et al. “A Cavity-Cooper Pair Transistor Scheme for Investigating Quantum Optomechanics in the Ultra-Strong Coupling Regime”. In: *New J. Phys.* 16.5 (2014), p. 055008. DOI: 10.1088/1367-2630/16/5/055008.

[51] Juuso Manninen et al. “Enhancement of the optomechanical coupling and Kerr nonlinearity using the Josephson capacitance of a Cooper-pair box”. In: *Phys. Rev. B* 105.14 (2022), p. 144508. ISSN: 2469-9969. DOI: 10.1103/PhysRevB.105.144508.

[52] Avishai Benyamini et al. “Real-space tailoring of the electron–phonon coupling in ultraclean nanotube mechanical resonators”. In: *Nat. Phys.* 10.2 (2014), pp. 151–156. DOI: 10.1038/nphys2842.

[53] Joel Moser et al. “Nanotube mechanical resonators with quality factors of up to 5 million”. In: *Nat. Nanotechnol.* 9.12 (2014), pp. 1007–1011. DOI: 10.1038/nnano.2014.234.

[54] Edward A Laird et al. “A high quality factor carbon nanotube mechanical resonator at 39 GHz”. In: *Nano Lett.* 12.1 (2012), pp. 193–197. DOI: 10.1021/nl203279v.

[55] Michael T Woodside and Paul L McEuen. “Scanned probe imaging of single-electron charge states in nanotube quantum dots”. In: *Science* 296.5570 (2002), pp. 1098–1101. DOI: 10.1126/science.1069923.

[56] A. K. Hüttel et al. "Single Electron Tunnelling through High-Q Single-Wall Carbon Nanotube NEMS Resonators". In: *Phys. Status Solidi B* 247.11-12 (2010), pp. 2974–2979. ISSN: 1521-3951. DOI: 10.1002/pssb.201000175.

[57] H. B. Meerwaldt et al. "Probing the Charge of a Quantum Dot with a Nanomechanical Resonator". In: *Phys. Rev. B* 86.11 (2012), p. 115454. DOI: 10.1103/PhysRevB.86.115454.

[58] G. Micchi, R. Avriller, and F. Pistolesi. "Mechanical Signatures of the Current Blockade Instability in Suspended Carbon Nanotubes". In: *Phys. Rev. Lett.* 115 (20 2015), p. 206802. DOI: 10.1103/PhysRevLett.115.206802.

[59] G. Micchi, R. Avriller, and F. Pistolesi. "Electromechanical transition in quantum dots". In: *Phys. Rev. B* 94 (12 2016), p. 125417. DOI: 10.1103/PhysRevB.94.125417.

[60] Yutian Wen et al. "A coherent nanomechanical oscillator driven by single-electron tunnelling". In: *Nat. Phys.* 16.1 (2020), pp. 75–82. DOI: 10.1038/s41567-019-0683-5.

[61] Carlos Urgell et al. "Cooling and self-oscillation in a nanotube electromechanical resonator". In: *Nat. Phys.* 16.1 (2020), pp. 32–37. DOI: 10.1038/s41567-019-0682-6.

[62] Ilya Khivrich, Aashish A. Clerk, and Shahal Ilani. "Nanomechanical PumpProbe Measurements of Insulating Electronic States in a Carbon Nanotube". In: *Nat. Nanotechnol.* 14.2 (2019), pp. 161–167. ISSN: 1748-3395. DOI: 10.1038/s41565-018-0341-6.

[63] F. Pistolesi, A. N. Cleland, and A. Bachtold. "Proposal for a Nanomechanical Qubit". In: *Phys. Rev. X* 11.3 (2021), p. 031027. ISSN: 2160-3308. DOI: 10.1103/PhysRevX.11.031027.

[64] P. Forn-Daz et al. "Ultrastrong coupling regimes of light-matter interaction". In: *Rev. Mod. Phys.* 91 (2 2019), p. 025005. DOI: 10.1103/RevModPhys.91.025005.

[65] F. Valmorra et al. "Vacuum-field-induced THz transport gap in a carbon nanotube quantum dot". In: *Nat. Commun.* 12.5490 (2021), pp. 1–8. ISSN: 2041-1723. DOI: 10.1038/s41467-021-25733-x.

[66] Natalia Ares et al. "Resonant optomechanics with a vibrating carbon nanotube and a radio-frequency cavity". In: *Phys. Rev. Lett.* 117.17 (2016), p. 170801. DOI: 10.1103/PhysRevLett.117.170801.

[67] Yutian Wen et al. "Measuring carbon nanotube vibrations using a single-electron transistor as a fast linear amplifier". In: *Appl. Phys. Lett.* 113.15 (2018), p. 153101. DOI: 10.1063/1.5052185.

[68] Carlo WJ Beenakker. "Theory of Coulomb-blockade oscillations in the conductance of a quantum dot". In: *Phys. Rev. B* 44.4 (1991), p. 1646. DOI: 10.1103/PhysRevB.44.1646.

[69] Jens Koch, Felix von Oppen, and A. V. Andreev. "Theory of the Franck-Condon blockade regime". In: *Phys. Rev. B* 74.20 (2006), p. 205438. ISSN: 2469-9969. DOI: 10.1103/PhysRevB.74.205438.

[70] Renaud Leturcq et al. “Franck–Condon blockade in suspended carbon nanotube quantum dots”. In: *Nat. Phys.* 5.5 (2009), pp. 327–331. ISSN: 1745-2481. DOI: 10.1038/nphys1234.

[71] Eros Mariani and Felix von Oppen. “Electron-vibron coupling in suspended carbon nanotube quantum dots”. In: *Phys. Rev. B* 80.15 (2009), p. 155411. ISSN: 2469-9969. DOI: 10.1103/PhysRevB.80.155411.

[72] Yuli V. Nazarov and Yaroslav M. Blanter. *Quantum Transport: Introduction to Nanoscience*. Cambridge, England, UK: Cambridge University Press, 2009. ISBN: 978-0-52183246-5. DOI: 10.1017/CBO9780511626906.

[73] Ronald Hanson et al. “Spins in few-electron quantum dots”. In: *Rev. Mod. Phys.* 79.4 (2007), p. 1217. DOI: 10.1103/RevModPhys.79.1217.

[74] Vera Sazonova et al. “A tunable carbon nanotube electromechanical oscillator”. In: *Nature* 431.7006 (2004), pp. 284–287. DOI: 10.1038/nature02905.

[75] M. Poot et al. “Modelling suspended carbon nanotube resonators”. In: *Phys. Status Solidi B* 244.11 (2007), pp. 4252–4256. ISSN: 0370-1972. DOI: 10.1002/pssb.200776130.

[76] Chung Chiang Wu and Zhaohui Zhong. “Capacitive spring softening in single-walled carbon nanotube nanoelectromechanical resonators”. In: *Nano letters* 11.4 (2011), pp. 1448–1451.

[77] S Sapmaz et al. “Carbon nanotubes as nanoelectromechanical systems”. In: *Phys. Rev. B* 67.23 (2003), p. 235414. ISSN: 2469-9969. DOI: 10.1103/PhysRevB.67.235414.

[78] Benot Witkamp. “High-frequency nanotube resonators”. PhD thesis. Technische Universiteit Delft, 2009. ISBN: 9789085930495.

[79] H. B. Meerwaldt, G. A. Steele, and H. S. J. van der Zant. “Fluctuating Nonlinear Oscillators: From Nanomechanics to Quantum Superconducting Circuits”. In: (2012). DOI: 10.1093/acprof:oso/9780199691388.003.0012.

[80] Andres Castellanos-Gomez et al. “Strong and tunable mode coupling in carbon nanotube resonators”. In: *Phys. Rev. B* 86 (4 2012), p. 041402. DOI: 10.1103/PhysRevB.86.041402.

[81] S Heinze et al. “Unexpected scaling of the performance of carbon nanotube Schottky-barrier transistors”. In: *Phys. Rev. B* 68.23 (2003), p. 235418. DOI: 10.1103/PhysRevB.68.235418.

[82] Stefan Heinze et al. “Carbon nanotubes as Schottky barrier transistors”. In: *Phys. Rev. Lett.* 89.10 (2002), p. 106801. DOI: 10.1103/PhysRevLett.89.106801.

[83] Lingjuan Feng et al. “Precision Measurement of Few Charges in Cavity Optoelectromechanical System”. In: *Quantum Inf. Process.* 19.5 (2020), p. 167. DOI: 10.1007/s11128-020-02658-w.

[84] J.-M. Pirkkalainen et al. “Cavity optomechanics mediated by a quantum two-level system”. In: *Nat. Commun.* 6.1 (2015), p. 6981. ISSN: 2041-1723. DOI: 10.1038/ncomms7981.

[85] I. C. Rodrigues, D Bothner, and G. A. Steele. “Coupling microwave photons to a mechanical resonator using quantum interference”. In: *Nat. Commun.* 10.1 (2019), p. 5359. ISSN: 2041-1723. DOI: 10.1038/s41467-019-12964-2.

[86] Aaron D OConnell et al. "Quantum ground state and single-phonon control of a mechanical resonator". In: *Nature* 464.7289 (2010), pp. 697–703. DOI: 10.1038/nature08967.

[87] David P Lake et al. "Processing light with an optically tunable mechanical memory". In: *Nat. Commun.* 12.1 (2021), pp. 1–9. DOI: 10.1038/s41467-021-20899-w.

[88] Ahmad Shafiei Aporvari and David Vitali. "Strong Coupling Optomechanics Mediated by a Qubit in the Dispersive Regime". In: *Entropy* 23.8 (2021), p. 966. DOI: 10.3390/e23080966.

[89] Andreas K Hüttel et al. "Carbon nanotubes as ultrahigh quality factor mechanical resonators". In: *Nano Lett.* 9.7 (2009), pp. 2547–2552. DOI: 10.1021/nl900612h.

[90] Julien Chaste et al. "A nanomechanical mass sensor with yoctogram resolution". In: *Nat. Nanotechnol.* 7.5 (2012), pp. 301–304. ISSN: 1748-3395. DOI: 10.1038/nnano.2012.42.

[91] A. K. Hüttel et al. "Single electron tunnelling through high-Q single-wall carbon nanotube NEMS resonators". In: *Phys. Status Solidi B* 247.11-12 (2010), pp. 2974–2979. DOI: 10.1002/pssb.201000175.

[92] Vera Sazonova et al. "A tunable carbon nanotube electromechanical oscillator". In: *Nature* 431.7006 (2004), pp. 284–287. DOI: 10.1038/nature02905.

[93] Florian Vigneau et al. "Ultrastrong coupling between electron tunneling and mechanical motion". In: *Phys. Rev. Res.* 4.4 (2022), p. 043168. ISSN: 2643-1564. DOI: 10.1103/PhysRevResearch.4.043168.

[94] Xinhe Wang et al. "Visualizing nonlinear resonance in nanomechanical systems via single-electron tunneling". In: *Nano Res.* 14.4 (2021), pp. 1156–1161. ISSN: 1998-0000. DOI: 10.1007/s12274-020-3165-2.

[95] A Tavernarakis et al. "Optomechanics with a hybrid carbon nanotube resonator". In: *Nat. Commun.* 9.1 (2018), pp. 1–8. DOI: 10.1038/s41467-018-03097-z.

[96] Ya M Blanter, O Usmani, and Yu V Nazarov. "Single-electron tunneling with strong mechanical feedback". In: *Phys. Rev. Lett.* 93.13 (2004), p. 136802. DOI: 10.1103/PhysRevLett.93.136802.

[97] O. Usmani, Ya. M. Blanter, and Yu. V. Nazarov. "Strong feedback and current noise in nanoelectromechanical systems". In: *Phys. Rev. B* 75.19 (2007). Publisher: American Physical Society, p. 195312. DOI: 10.1103/PhysRevB.75.195312.

[98] S. D. Bennett and A. A. Clerk. "Laser-like instabilities in quantum nano-electromechanical systems". In: *Phys. Rev. B* 74.20 (2006), p. 201301. ISSN: 2469-9969. DOI: 10.1103/PhysRevB.74.201301.

[99] Alexander Eichler et al. "Parametric amplification and self-oscillation in a nanotube mechanical resonator". In: *Nano Lett.* 11.7 (2011), pp. 2699–2703. DOI: 10.1021/nl200950d.

[100] Daniel R Schmid et al. "Magnetic damping of a carbon nanotube nano-electromechanical resonator". In: *New J. Phys.* 14.8 (2012), p. 083024. DOI: 10.1088/1367-2630/14/8/083024.

[101] D. R. Schmid et al. "Liquid-induced damping of mechanical feedback effects in single electron tunneling through a suspended carbon nanotube". In: *Appl. Phys. Lett.* 107.12 (2015), p. 123110. DOI: 10.1063/1.4931775.

[102] Kyle Willick and Jonathan Baugh. "Self-driven oscillation in Coulomb blockaded suspended carbon nanotubes". In: *Phys. Rev. Res.* 2.3 (2020), p. 033040. DOI: 10.1103/PhysRevResearch.2.033040.

[103] Philipp Strasberg, Christopher W Wächtler, and Gernot Schaller. "Autonomous implementation of thermodynamic cycles at the nanoscale". In: *Phys. Rev. Lett.* 126.18 (2021), p. 180605. DOI: 10.1103/PhysRevLett.126.180605.

[104] Cyril Elouard, Maxime Richard, and Alexia Auffèves. "Reversible work extraction in a hybrid opto-mechanical system". In: *New J. Phys.* 17.5 (2015), p. 055018. DOI: 10.1088/1367-2630/17/5/055018.

[105] Juliette Monsel, Cyril Elouard, and Alexia Auffèves. "An autonomous quantum machine to measure the thermodynamic arrow of time". In: *npj Quantum Inf.* 4.1 (2018), p. 59. DOI: 10.1038/s41534-018-0109-8.

[106] C. W. Wächtler et al. "Dissipative nonequilibrium synchronization of topological edge states via self-oscillation". In: *Phys. Rev. B* 102.1 (2020), p. 014309. DOI: 10.1103/PhysRevB.102.014309.

[107] Jianqiang Lin, Supratik Guha, and Shriram Ramanathan. "Vanadium Dioxide Circuits Emulate Neurological Disorders". In: *Front. Neurosci.* 12 (2018). ISSN: 1662-453X.

[108] P. Stoliar, O. Schneegans, and M. J. Rozenberg. "Implementation of a Minimal Recurrent Spiking Neural Network in a Solid-State Device". In: *Phys. Rev. Applied* 16.3 (2021). Publisher: American Physical Society, p. 034030. DOI: 10.1103/PhysRevApplied.16.034030.

[109] Rodolfo Rocco et al. "Exponential Escape Rate of Filamentary Incubation in Mott Spiking Neurons". In: *Phys. Rev. Applied* 17.2 (2022). Publisher: American Physical Society, p. 024028. DOI: 10.1103/PhysRevApplied.17.024028.

[110] Edward A. Laird et al. "Quantum transport in carbon nanotubes". In: *Rev. Mod. Phys.* 87.3 (2015). Publisher: American Physical Society, pp. 703–764. DOI: 10.1103/RevModPhys.87.703.

[111] Alexander Eichler et al. "Nonlinear damping in mechanical resonators made from carbon nanotubes and graphene". In: *Nat. Nanotechnol.* 6.6 (2011), pp. 339–342. DOI: 10.1038/nnano.2011.71.

[112] A. D. Armour, M. P. Blencowe, and Y. Zhang. "Classical dynamics of a nanomechanical resonator coupled to a single-electron transistor". In: *Phys. Rev. B* 69.12 (2004), p. 125313. ISSN: 2469-9969. DOI: 10.1103/PhysRevB.69.125313.

[113] Crispin W Gardiner. *A Handbook of Stochastic Methods*. Berlin Heidelberg: Springer, 1985.

[114] O Usmani, Ya M Blanter, and Yu V Nazarov. "Strong feedback and current noise in nanoelectromechanical systems". In: *Phys. Rev. B* 75.19 (2007), p. 195312. DOI: 10.1103/PhysRevB.75.195312.

[115] Wilfred G Van der Wiel et al. "Electron transport through double quantum dots". In: *Rev. Mod. Phys.* 75.1 (2002), p. 1. DOI: 10.1103/RevModPhys.75.1.

[116] Harold B. Meerwaldt, Gary A. Steele, and Herre S. J. van der Zant. *Carbon nanotubes: Nonlinear high-Q resonators with strong coupling to single-electron tunneling*. 2012. DOI: 10.48550/ARXIV.1205.4921.

[117] Y. H. Ku and Xiaoguang Sun. "CHAOS and limit cycle in Duffing's equation". In: *Journal of The Franklin Institute* 327.2 (1990), pp. 165–195.

[118] G. J. Milburn. "The thermodynamics of clocks". In: *Contemporary Physics* 61.2 (2020), pp. 69–95.

[119] G. J. Milburn and Sahar Basiri-Esfahani. "The physics of learning machines". In: *Contemporary Physics* 0.0 (2022), pp. 1–27.

[120] D. Wahyu Utami et al. "Quantum noise in the electromechanical shuttle: Quantum master equation treatment". In: *Physical Review B* 74.1 (2006), p. 014303. ISSN: 1098-0121, 1550-235X. DOI: 10.1103/PhysRevB.74.014303.

[121] Itamar Katz et al. "Signatures for a Classical to Quantum Transition of a Driven Nonlinear Nanomechanical Resonator". In: *Physical Review Letters* 99.4 (2007), p. 040404. ISSN: 0031-9007, 1079-7114. DOI: 10.1103/PhysRevLett.99.040404.

[122] Jonne V. Koski et al. "Experimental realization of a Szilard engine with a single electron". In: *Proceedings of the National Academy of Sciences* 111.38 (2014), pp. 13786–13789. ISSN: 1091-6490. DOI: 10.1073/pnas.1406966111.

[123] Matteo Scandi et al. "Minimally Dissipative Information Erasure in a Quantum Dot via Thermodynamic Length". In: *Physical Review Letters* 129.27 (2022). ISSN: 1079-7114. DOI: 10.1103/physrevlett.129.270601.

[124] Jing-Hao Xue and D. Michael Titterington. "The p-folded cumulative distribution function and the mean absolute deviation from the p-quantile". In: *Statistics & Probability Letters* 81.8 (2011), pp. 1179–1182. ISSN: 0167-7152. DOI: https://doi.org/10.1016/j.spl.2011.03.014.